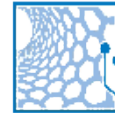


Technische Universität München

Lehrstuhl Für Nanoelektronik



Numerical and analytical modeling of Fourier domain mode-locked lasers

Horatiu-Sebastian Todor



Vollständiger Abdruck der von der Fakultät für Elektrotechnik und Informationstechnik der Technischen Universität München zur Erlangung des akademischen Grades

Doktors der Naturwissenschaften

genehmigten Dissertation.

Vorsitzender:

Univ.-Prof. Dr. Ing., Dr. Ing. habil. Erwin Biebl
Prüfer der Dissertation:

1. Junior-Fellow Dr. Christian Jirauschek
2. Univ.-Prof. Jonathan J. Finley, Ph.D.

Die Dissertation wurde am 27.03.2012 bei der Technischen Universität München eingereicht und durch die Fakultät für Elektrotechnik und Informationstechnik am 18.02.2013 angenommen.

Contents

Zusammenfassung (German)	7
Abstract (English)	9
1 Introduction	11
2 Propagation of electromagnetic waves in linear and nonlinear media	17
2.1 Linear propagation of electromagnetic waves	17
2.1.1 Maxwell equations	17
2.1.2 Wave equation for linear propagation in isotropic media	18
2.1.3 Dispersion	19
2.2 Linear and nonlinear media	20
2.2.1 Kerr effect	20
2.2.2 Self-phase modulation	21
2.2.3 Nonlinear Schrödinger equation	21
3 Fourier domain mode-locking: Applications, experimental setup, governing equation and numerical simulation	23
3.1 Applications of FDML lasers	24
3.1.1 Chemical detection and sensing applications	24
3.1.2 Optical coherence tomography	24
3.2 Experimental setup of the FDML laser used for our simulations	27
3.3 FDML equation	29
3.4 Numerical simulation	31
3.4.1 Split-step Fourier algorithm	31
3.4.2 Implementation of the various elements of the FDML laser	32
3.4.3 C++ code	34

4	Instantaneous lineshape analysis of FDML lasers	37
4.1	Experimental setup and measurement of the instantaneous linewidth	38
4.2	Calculation of the instantaneous linewidth	39
4.3	Results	39
4.3.1	Agreement with the experiment	39
4.3.2	Timing offset, linewidth enhancement factor and spectral shift	40
4.3.3	Conclusions	43
5	Balance of physical effects causing stationary operation of FDML lasers	45
5.1	Temporal and spatial evolution of the optical cavity field	46
5.1.1	Discussion of the spectral shaping effects	47
5.1.2	Analysis of the FDML dynamics in steady state operation	53
5.1.3	Comparison to experiment	53
5.2	Conclusion	55
6	Pulse compression in an FDML laser	59
6.1	Types of ultrashort pulsed lasers	59
6.2	Ideal pulse compression	60
6.3	Analytical treatment of pulse compression for the example of a linear ramp	61
6.4	Experimental setup for pulse compression	63
6.5	Simulation of pulse compression and comparison to the experiment	66
6.5.1	Simulation	66
6.5.2	Compression routine and emulation of the experiment	66
6.5.3	Comparison with the experiment	71
6.5.4	Optimization of the performance and future outlook	73
7	Analytical model for FDML operation	75
7.1	FDML laser with slow gain saturation	75
7.2	FDML laser with gain saturation, self-phase modulation and third order dispersion	77
7.2.1	Spatial evolution of amplitude, chirp and pulse length	79
7.3	Steady state solution	80
7.3.1	Analytical solution	80
7.3.2	Properties of the steady-state solution	81
7.3.3	The frequency dependent gain parameter g_ω	82
7.3.4	The gain parameter g_0	82
7.3.5	The sweep range $\Delta\omega$	82
7.3.6	The sweep filter loss parameter a_s	83
7.3.7	The Henry factor α	83

7.3.8	The sweep length T_R	83
7.3.9	The overall cavity loss a_l	83
7.3.10	The second order dispersion coefficient D_2	83
7.3.11	The nonlinearity γ	84
7.3.12	The saturation parameter r	84
7.3.13	The instantaneous linewidth	84
7.4	Summary of the model and future outlook	84
8	Summary and future outlook	87
	Appendix	88
	Nomenclature	105
	List of Figures	109
	List of Tables	113
	Publications	123
	Acknowledgement	123
	Curriculum Vitae	127

Zusammenfassung (German)

Das Hauptziel dieser Arbeit ist die numerische und analytische Modellierung Fourierdomänen modengekoppelter (FDML) Laser. Diese Aufgabe wird durch numerische Simulationen bewerkstelligt, welche die FDML-Propagationsgleichung mit Hilfe eines split-step Fourier Algorithmus in C++ löst. Basierend auf der vorhergehenden Arbeit von Dr. Christian Jirauschek, wird dieser Simulationscode weiterentwickelt und modifiziert, um die Erforschung der instantanen Linienbreite von FDML-Lasern zu ermöglichen. Dadurch kann die instantane Linienbreite zum ersten Mal theoretisch untersucht und mit den experimentellen Daten eines existierenden FDML-Lasers von Dr. Robert Hubers Gruppe an der LMU München verglichen werden. Die Linienform der FDML-Laserstrahlung wird untersucht, und physikalische Effekte, die zur Linienform beitragen, werden identifiziert. Eine sehr gute Übereinstimmung mit den experimentellen Daten wird vorgefunden, was die Gültigkeit der numerischen Simulation der FDML-Propagationsgleichung untermauert. Sogar Veränderungen der Linienform durch eine Verstimmung des Lasers kann korrekt vorhergesagt werden. Zusätzlich ermöglicht es die Simulation, gezielt Laserparameter ein- und auszuschalten, um deren Auswirkung auf die Linienform zu untersuchen. Auf diese Weise wird entdeckt, dass in einem FDML-Laser die verstärkte spontane Emission (ASE) keinen Beitrag zur instantanen Linienbreite liefert, im Gegensatz zu anderen bekannten Laserquellen. Diese neue Entdeckung ermöglicht eine zusätzliche Einsicht in die Funktionsmechanismen von FDML-Lasern.

Weiterhin wird unter Verwendung numerischer Simulationen die Bildung eines stationären Betriebszustandes untersucht, und das Gleichgewicht der physikalischen Effekte, die zu dessen Entstehung führen. Durch die systematische Untersuchung, welchen Einfluss eine physikalische Größe auf die spektrale Leistungsdichte hat, wird analysiert, welche Effekte sich einander ausgleichen und zur Bildung eines stationären Zustands führen. Es zeigt sich, dass durch die Linienverstärkung im Verstärkermedium, in Kombination mit der Verstärkerdynamik eine Verschiebung des instantanen Leistungsspektrums zu niedrigeren Frequenzen hin, verursacht wird. Die Dispersion führt zusätzlich zu einer zeitabhängigen spektralen Verschiebung. Dem wird durch die asymmetrische Absorption des spektralen Bandpassfilters entgegengewirkt. Der zweite Effekt der auftritt, ist dass die Selbstphasenmodulation in der langen Verzögerungsfaser zu einer spektralen Verbreiterung führt, was wiederum durch den Bandpassfilter kompensiert wird. Die Linienverstärkung und die Dispersion beeinflussen das instantane Leistungsspektrum zusätzlich. Diese Ergebnisse werden wieder detailliert mit den experimentellen Daten von Robert Hubers

Gruppe verglichen und zeigen eine gute Übereinstimmung.

Zum ersten Mal wird die Möglichkeit eines gepulsten Betriebs von FDML-Lasern untersucht. Eine modifizierte Variante der vorhergehenden numerischen Simulation und ein selbst geschriebenes Matlab Programm wird verwendet um die Dispersionskompensation des Experiments zu simulieren. Dies wird durch die exakte Nachbildung aller Effekte im Experiment, das wieder von Robert Hubers Gruppe durchgeführt wird, erreicht. Auf diese Art und Weise kann die Pulskompression simuliert werden, und eine gute Übereinstimmung mit dem Experiment wird erreicht, wobei die kürzest möglichen Pulse eine Länge von 60 ps haben. Auch die Abhängigkeit der Pulslänge von Parametern wie zum Beispiel der Filterbandbreite und der Filterverzögerung werden untersucht und richtig vorhergesagt. Die Simulation ermöglicht zudem die zusätzliche Optimierung des existierenden Aufbaus durch die Vorhersage dass kleinere Filterbandbreiten und eine noch bessere Dispersionskompensation die Leistung eines gepulsten FDML-Lasers bei weitem verbessern können, mit Pulsdauern im Bereich des Zeit-Bandbreite Produkts.

Abschließend wird zum ersten Mal ein analytisches Modell für einen FDML-Laser hergeleitet. Hierbei wird ein Gaußmodell als Ansatz benutzt. Es wird die FDML-Propagationsgleichung gelöst, wobei die Bewegungsgleichungen sowohl mittels des Variationsprinzips als auch mit der Methode der Momente hergeleitet werden. Beide Methoden führen zu den gleichen Bewegungsgleichungen. Es wird gezeigt, dass das simple Gaußmodell nicht ausreicht, um korrekt jeden Effekt des FDML-Betriebs vorherzusagen, sondern ein allgemeinerer Ansatz, wie zum Beispiel ein Hermite-Gauß-Ansatz, benötigt wird.

Abstract (English)

The main objective of this thesis is the numerical and analytical modeling of Fourier domain mode-locked (FDML) lasers. This task is achieved by employing a numerical simulation, that solves the FDML evolution equation based on a split-step Fourier algorithm, written in C++. Based on the previous work by Dr. Christian Jirauschek, this simulation is further developed and modified in order to enable the examination of the instantaneous linewidth of FDML lasers. Using this numerical simulation, the instantaneous linewidth is for the first time theoretically investigated and then compared to experimental data of an existing FDML laser setup provided by Dr. Robert Huber and his group from LMU Munich. The lineshape of the FDML laser output is investigated, and physical effects that contribute to the lineshape are identified. Very good agreement with the experimental data is found, validating the numerical simulation of the FDML evolution equation. Even deformations of the lineshape by a detuning of the laser setup can correctly be predicted by the simulation. In addition to the experiment, the simulation enables the subsequent on- and off-switching of laser parameters, in order to study their impact on the lineshape. It is so found that in an FDML laser, the amplified spontaneous emission (ASE) does not contribute to the instantaneous linewidth, in contrast to other known laser sources. This novel discovery gives additional insight into the working principles of FDML lasers.

Further, using numerical simulations, the formation of a stationary state is investigated, and the balance of physical effects that enable the formation of a steady state is studied. By systematically investigating what effect the various physical quantities have on the spectral power density, it is found which effects balance each other and lead to the formation of a steady-state field. It is here found that a shift of the instantaneous power spectrum towards lower frequencies is caused by the linewidth enhancement of the gain medium in combination with the gain recovery dynamics. Also the dispersion induces a time dependent spectral shift. These effects are then counterbalanced by the asymmetric absorption of the tunable spectral bandpass filter. Furthermore, self-phase modulation in the long fiber delay line causes a spectral broadening, which is counterbalanced by the bandpass filter. Also the linewidth enhancement and dispersion influence the instantaneous power spectrum. These results are also carefully validated with experimental data from the Robert Huber group, again showing good agreement.

For the first time, the possibility of a compression of the FDML output to short pulses is investigated. Using a modified version of the previous numerical simulation and a specially developed Matlab code,

the dispersion compensation of the experiment is simulated. This is done by exactly emulating every effect which occurs in the experiment, again performed by the Robert Huber group. In this way, the pulse compression itself can be simulated and good agreement to the experimental data is found, with the shortest achievable pulses being 60 ps. Also the dependence of the pulse length on parameters such as the sweep filter bandwidth and detuning are investigated and correctly predicted. In addition, the simulation enables a further optimization of the existing setup by predicting that smaller filter bandwidths and a better dispersion compensation can result in greatly reduced pulse durations in the range of the time-bandwidth product.

In the last step, for the first time an analytical model for an FDML laser is presented based on a chirped Gaussian ansatz. Here, the FDML evolution equation is solved, where the equations of motion are being derived using a variational approach, as well as the method of moments. Both methods yield the same equations of motion. It is then found that the simple chirped Gaussian model does not suffice to correctly predict every effect of FDML operation, but a more general approach is needed, such as a Hermite-Gaussian model.

Chapter 1

Introduction

In 1958 a new era for science began, when Townes and Schawlow first formulated the concept of a novel light source based on amplification of visible light by stimulated emission [Sch58]. Only two years later the first laser was built by Maiman [Mai60]. Since then, the laser has become a fundamental tool not only in science and engineering, but also in everyday life. One example for a scientific application is laser cooling, the most prominent example being the possibility of cooling ensembles of bosons to such temperatures that Bose-Einstein condensates can form [Ket03]. Also for precision time and length measurements, a laser is irreplaceable [Did01][Kik86][Beh86]. Other fields of application include newly emerged high energy laser physics for creating nuclear fusion [Hay07], or sensing applications. Laser sensors are used for example for gas detection [Toe97] or even for the detection of land mines [Boh06].

A great evolution step for lasers came in 1964, when Hargrove et al. [Har64] were able to create ultra short laser pulses by means of mode-locking. This opened up a whole new field of applications, ranging from ultra precise measurements of physical quantities [Wit05][Jon05], (e.g in femtochemistry) to commercial applications, e.g. in optical communication [Mur10] [Kat11], and also medical applications, such as tissue ablation [Nee96] and optical coherence tomography [Kra08][Lim05]. One of the mechanisms for achieving very short pulses is called mode-locking, where a fixed phase relationship between the laser modes is achieved by passive [Moc65] or active amplitude modulation [Har64] of the laser light.

Another field where high precision laser interferometry is crucial, is astronomy. Using laser interferometry, LISA is a proposed mission which aims to find gravitational waves in the cosmos [Arm99][Ben98]. Lasers also play a role for large telescopes, where atmospheric turbulences are suppressed by the use of a laser guide star [Max97][Par94] in adaptive optics [Tys10]. In everyday life lasers have been playing an increasing role within the last decades, e.g, small semiconductor lasers in DVD players or laser pointers. A novel way of mode-locking was introduced in 2006 [Hub06], when Fourier domain-mode locking (FDML) was first demonstrated as a means of achieving a modulation of the modes in the frequency or Fourier domain, hence the name. The method used was to employ a tunable Fabry-Perot bandpass filter [Ath81], which is driven in such a way that it exactly matches the roundtrip time of the laser light within the

cavity. This new means of mode-locking overcame the limitations of conventional swept-laser sources with respect to the maximum achievable sweep rate [Hub05]. In conventional lasers, the maximum achievable sweep rate is given by the buildup time of the laser modes within the cavity [Tel75]. In Fourier domain mode-locking however, the tunable bandpass filter is synchronously driven, matching the exact frequency of the laser light. This leads to a fixed phase relation of the modes in the frequency domain, hence the name Fourier domain mode-locking, since it represents a novel mode-locking regime for lasers by frequency rather than amplitude modulation. The FDML laser produces a continuous wave (cw) output [Jav61]. In addition, FDML is true lasing, rather than being a light source based on amplified spontaneous emission (ASE) [Jir08]. Because FDML lasers emit a near infrared cw light output with a coherence length of several millimeters, it is highly suitable for numerous applications, ranging from sensing applications [Lau07], to medical imaging applications such as optical coherence tomography (OCT). The very high sweep rates of FDML lasers compared to standard tunable lasers of several hundred kHz [Jeo08], make it the imaging tool of choice for OCT.

A record sweep rate of above 5 MHz has been achieved using a 325 kHz FDML laser and multiplying the sweep repetition rate by using the so called buffering technique [Hub06][Hub06B][Wie10]. Besides restrictions in the tuning speed of the filter, no fundamental sweep speed limitations arise in FDML. In principle, many types of rapidly tunable filters can be applied, such as Sampled Grating Distributed Bragg Reflector (SGDBR) based filters [Kle11], rotating polygon mirror based filters [Der08], filters based on resonant galvanometer mirrors [Yun03], MEMS-based tunable Fabry Perot filters [Hub05C] etc. Typical instantaneous linewidths of <0.1 nm, corresponding to a coherence length of several millimeters up to centimeters [Vai95], together with the high sweep rates currently make the FDML laser the system of choice for many high speed OCT and sensing applications [Hub06][Sri08][Liu08][Mao09]. To date, other very promising approaches that do not suffer from the inherent limitation of sweep speed have not achieved the combination of speed, tuning range, low noise and output power. A 5 MHz swept source realized by temporally stretching an ultrashort laser pulse achieved an extremely wide tuning range, but had too high noise for high quality OCT imaging [Tsa11]. A wavelength swept ASE source achieved >300 kHz tuning rate, but also exhibited too much noise to fully achieve shot noise limited detection in OCT [Moo06][Eig09]. Tunable VCSELs with a MEMS mirror achieve up to 760 kHz sweep rate [Eig11][Yan09][Jay11] with very good coherence length but smaller sweep range and output power than FDML lasers. Classical swept lasers for OCT have been demonstrated at sweep rates up to 400kHz [Ove11].

The scope of this thesis is to gain further insight into the physical working principles of FDML lasers. Based on previous work by Christian Jirauschek, a numerical simulation is used for this task, which is then further modified for the different analyses. Comparison to the experiments from the Robert Huber group at the LMU are throughout the thesis an important cornerstone to validate the results. Furthermore, a derivation of an analytical model for FDML operation is discussed. The main results of this

thesis are listed below.

- An analysis of the instantaneous linewidth of the FDML laser is presented, in which the central governing mechanisms are found. By subsequently turning on and off certain physical quantities, a unique property of FDML operation is found: The linewidth is not governed by amplified spontaneous emission (ASE) or external noise sources, but is based entirely on the intrinsic properties of the laser.
- The investigation of the spatio-temporal dynamics yields insight into the balance of the physical effects that lead to stationary operation of FDML lasers. Every effect is analyzed and its contribution to the temporal and spatial behavior is listed. A quantitative analysis is presented on how the various effects balance each other, leading to a stable spectrum and output power.
- A numerical method is developed to simulate pulse compression in an FDML laser. Comparison to theory shows good agreement. The minimal achievable pulse length is found to be limited only by the sweep filter bandwidth and the remaining dispersion in the laser setup. Thus, much shorter pulse lengths seem achievable in future laser setups.
- The FDML evolution equation is solved for instantaneous gain saturation without nonlinearity, revealing that a chirped Gaussian solution describes such a setup very well. Numerical simulations are performed in order to validate the result. The FDML equation is then solved for a simplified gain saturation model and additional nonlinearity. The results show that the chirped Gaussian solution does not suffice to describe this FDML setup, and a more general Hermite-Gaussian solution is needed.

The outline of this thesis is as follows:

In Chapter 2, the basic principles of optical pulse propagation are described. Starting point are the Maxwell equations, the foundation of every classical treatment of electrodynamics. First, the linear propagation of electromagnetic waves in linear media is explained. Then, the role of dispersion and gain is discussed, as these effects are important for the treatment of the FDML laser. As gain and loss play an important role in the FDML laser, these effects are also explained for general electromagnetic fields. We also have to treat nonlinear optical propagation occurring in the fiber part of the FDML setup. This is done by first describing the Kerr effect and the effect of self-phase modulation (SPM). In the last step, the nonlinear Schrödinger equation (NSE) is derived, which is the foundation for the later derivation of the FDML evolution equation.

Another cornerstone of this thesis is presented in chapter 3, which comprises the theoretical framework developed by Christian Jirauschek in [Jir08]. There, an analytical equation for FDML operation based on the NSE ansatz is derived. A central step is the simplification of the NSE ansatz, considering for example the role of the sweep filter in FDML operation. As will be seen, the transformation from

the laboratory to the reference frame of the sweep filter will greatly reduce the complexity of the FDML equation, enabling more efficient computation. This leads us to a simplified evolution equation that will be the central governing equation for FDML operation and the starting point for further analytical and numerical investigation. Furtheron, the numerical simulation on which the results are based, and the split-step Fourier algorithm which is necessary for the simulation, is explained. The simulation utilizes the FFTW (fastest Fourier transform in the west) [Fri05] algorithm, with a resolution of 8 million grid points.

In Chapter 4, the most important parameter of FDML operation, the instantaneous lineshape will be analyzed. This property of the FDML laser is indirectly related to the coherence length of the emitted laser light, an increase of the coherence length would be a very desirable goal, with the possibility of enabling new applications for FDML lasers. First, the experimental setup is shown, and the method for experimentally extracting the instantaneous lineshape is explained. The lineshape of the instantaneous power spectrum is then numerically investigated, determining the central governing mechanisms and yielding good agreement between theory and experiment. This is done also for the case that the sweep filter and the cavity roundtrip time are detuned, revealing further insight into the FDML dynamics. Finally it is found that, in contrast to other known laser sources, the instantaneous linewidth is governed by the intrinsic dynamics of the FDML laser, such as the sweep filter and gain action, dispersion and self-phase modulation, and is thus not dominated by ASE or external noise sources.

In Chapter 5, the balance of the physical effects leading to stationary FDML operation is investigated. After explaining the experimental setup of the laser, the temporal propagation of the optical light field within the laser cavity is analyzed. The implementation of the Gaussian gating used in the experiment to retrieve the instantaneous linewidth into the numerical analysis is discussed. Then the experimental and numerical linewidths, as well as the mean frequencies of the instantaneous power spectra are extracted. Good agreement is found between theory and experiment, further validating the theoretical work. Afterwards, all physical effects are discussed that contribute to the shape of the instantaneous linewidth. It is found that the linewidth enhancement of the SOA in combination with the gain recovery dynamics play an important role for the observed shift of the instantaneous power spectrum. Another important physical property is the dispersion, which induces a time dependent spectral shift. It is found that these effects are counteracted by the asymmetric absorption of the tunable bandpass filter. Another important mechanism that is found, is the broadening of the instantaneous power spectrum by the self-phase modulation in the delay fiber. The linewidth enhancement and the dispersion also influence the spectrum. The broadening is again counteracted by the repetitive filtering after each roundtrip in the bandpass filter.

In Chapter 6, the compression of the FDML output is discussed. In regular mode, the FDML laser emits a highly chirped cw output. However, often short pulses are needed. Compression is experimentally achieved by the inclusion of a dispersion compensation fiber (DCF) into the laser setup and external compression with a high dispersion fiber. On the theoretical side ideal external compression is ca be

obtained by compensating the phase of the complex field envelope. A perfect compensation of the phase leads to perfect compression, which is not possible in the experiment, but will be done numerically and also shown analytically. For non-perfect compensation we find typical pulse lengths of 20-40 picoseconds, which is in good agreement with the experimental results.

In Chapter 7, an analytical model for FDML operation is derived, based on the evolution equation from Chapter 2. First, the general solutions of the FDML equation are discussed, coming to the conclusion that they are unsuitable for a straight-forward analytical model, because with our laser parameters, the function arguments become so large that the numerical function evaluation is inhibited. Then, the exact solution of a simplified FDML equation is derived using a chirped Gaussian ansatz. This yields the equations of motion for FDML operation. After that, the equations of motion are derived for the full FDML equation, using the variational principle [Jir06], known from theoretical mechanics, by minimizing the action of the Lagrangian. For comparison, another ansatz for the derivation of the equations of motion is discussed, being the method of moments [Jir11]. Then, the solutions of the equations of motion are discussed and the impact of altering certain parameters of FDML operation is investigated and the effects are discussed.

In Chapter 8, this thesis is summarized and an outlook for FDML lasers is given. In this thesis, several new insights into FDML lasing are gained. It is found that the instantaneous linewidth is an intrinsic property of the FDML laser, determined by the lasing parameters, rather than ASE or external noise sources. Then there is a very good agreement between theory and experiment concerning the position and time dependent propagation of the instantaneous linewidth within the laser cavity. Also, based on the presented analytical model, a future optimization of the FDML laser, especially a reduction of the instantaneous linewidth, seems achievable. This would open up a whole new field of applications for FDML lasers, with sensory applications beyond OCT.

Chapter 2

Propagation of electromagnetic waves in linear and nonlinear media

In the following, the propagation of electromagnetic waves through linear and nonlinear media is explained. The starting point for this are the Maxwell equations, the cornerstone of electrodynamics. Using the Maxwell equations, we then derive the wave equation for the propagation of electromagnetic waves in linear media. The role of dispersion is treated, as well as the role of loss and gain. These are important physical effects that will also be analyzed in detail later for the case of the FDML laser. Then, the propagation of electromagnetic waves in nonlinear media is explained. As the FDML laser has a long delay fiber where nonlinear effects play a role, the Kerr effect is explained in detail. The last step is the derivation of the nonlinear Schrödinger equation, which is later on used as the starting point for the derivation of the FDML evolution equation.

2.1 Linear propagation of electromagnetic waves

2.1.1 Maxwell equations

The Maxwell equations for the propagation of electromagnetic waves in media can be written as [Max64]:

$$\vec{\nabla} \times \vec{H} = \vec{j} + \frac{\partial}{\partial t} \vec{D}; \quad (2.1.1)$$

$$\vec{\nabla} \times \vec{E} = -\frac{\partial}{\partial t} \vec{B}; \quad (2.1.2)$$

$$\vec{\nabla} \cdot \vec{D} = \rho; \quad (2.1.3)$$

$$\vec{\nabla} \cdot \vec{B} = 0; \quad (2.1.4)$$

where \vec{E} is the electric field, \vec{D} is the dielectric flux, \vec{B} is the magnetic flux and \vec{H} is the magnetic field. The current density is denoted as \vec{j} , the charge density is ρ . The Maxwell equations must be supplemented by material equations that describe the interaction of the fields with the medium:

$$\vec{D} = \epsilon_0 \vec{E} + \vec{P}; \quad (2.1.5)$$

$$\vec{B} = \mu_0 \vec{H} + \vec{M}; \quad (2.1.6)$$

where ϵ_0 is the permittivity, μ_0 is the permeability, \vec{P} is the polarization and \vec{M} is the magnetization. We can now derive the wave equation from Maxwell's equation by taking the vector rotation of (2.1.2) and using the relation $\vec{\nabla} \times (\vec{\nabla} \times \vec{E}) = \vec{\nabla} (\vec{\nabla} \cdot \vec{E}) - \Delta \vec{E}$ from vector analysis. We then arrive at

$$\Delta \vec{E} - \mu_0 \frac{\partial}{\partial t} \left(\vec{j} + \epsilon_0 \frac{\partial \vec{E}}{\partial t} + \frac{\partial \vec{P}}{\partial t} \right) = \frac{\partial}{\partial t} \vec{\nabla} \times \vec{M} - \vec{\nabla} (\vec{\nabla} \cdot \vec{E}). \quad (2.1.7)$$

By introducing the velocity constant of light in vacuum

$$c_0 = \sqrt{\frac{1}{\epsilon_0 \mu_0}} \quad (2.1.8)$$

we then arrive at the wave equation

$$\left(\Delta - \frac{1}{c_0^2} \frac{\partial^2}{\partial t^2} \right) \vec{E} = \mu_0 \left(\frac{\partial \vec{j}}{\partial t} + \frac{\partial^2 \vec{P}}{\partial t^2} \right) + \frac{\partial}{\partial t} \vec{\nabla} \times \vec{M} - \vec{\nabla} (\vec{\nabla} \cdot \vec{E}). \quad (2.1.9)$$

2.1.2 Wave equation for linear propagation in isotropic media

The wave equation (2.1.9) greatly simplifies for the case of a dielectric and nonmagnetic medium. In such a medium, with no free charges and thus no currents, we have $\vec{M} = \vec{j} = \vec{0}$ and $\rho = 0$. The wave equation (2.1.9) now simplifies to

$$\left(\Delta - \frac{1}{c_0^2} \frac{\partial^2}{\partial t^2} \right) \vec{E} = \mu_0 \frac{\partial^2 \vec{P}}{\partial t^2} \quad (2.1.10)$$

because we have $\vec{\nabla} \cdot \vec{E} = 0$ for a homogenous medium. Also in the case of weak inhomogenities or weak nonlinearities, this term can be neglected [Gra91][Yar89][Boy03]. A scalar constant χ , the susceptibility, can now be introduced that relates the polarization and the electric field with each other by $\vec{P} = \chi \vec{E}$. The susceptibility can also be linked to the refractive index of the medium. Here, it is convenient to switch to the frequency domain by means of Fourier transformation (see Appendix A). We have the simple relation

$$1 + \chi(\omega) = n^2(\omega); \quad (2.1.11)$$

where ω denotes the angular frequency $\omega = 2\pi f$ and n is the refractive index of the medium. With

the velocity of light in the medium $c = c_0/n$ we can write (2.1.10) in the Fourier domain, which can be written in a very simple form as

$$\left(\Delta + \frac{\omega^2}{c^2}\right)\tilde{\vec{E}}(\omega) = 0; \quad (2.1.12)$$

where $\tilde{\vec{E}}(\omega)$ is the electric field in the Fourier domain.

2.1.3 Dispersion

For the propagation of an optical pulse, which means a temporally limited electromagnetic wave, we can write the electric field as a product of the envelope and a carrier function [DrJ05]

$$\vec{E}(\vec{r}, t) = \mathcal{R} \left[\vec{A}(\vec{r}, t) e^{i(\vec{k}_c \vec{r} - \omega_c t)} \right]. \quad (2.1.13)$$

The envelope function is denoted by $\vec{A}(\vec{r}, t)$, and the carrier is described by the angular carrier frequency ω_c . The wavevector of the carrier is denoted by \vec{k}_c . The envelope function can be written as

$$\vec{A}(\vec{r}, t) = \int_{-\infty}^{\infty} \tilde{\vec{A}}(\vec{r}, \omega) e^{i(\vec{k}(\omega) \vec{r} - \omega t)} d\omega; \quad (2.1.14)$$

with a wavevector $\vec{k}(\omega)$ depending on the angular frequency ω of the envelope function. In the following, we assume that the wavevector is parallel to the z-axis, so that $\vec{k}(\omega) = k(\omega)\hat{e}_z$. We can now expand the wavenumber $k(\omega)$ in the vicinity of the center frequency ω_c with $\omega = \omega_c + \Omega$ into a Taylor series,

$$\begin{aligned} k(\omega) &= k(\omega_c) + \Omega \left(\frac{dk}{d\omega} \right)_{\omega=\omega_c} + \frac{1}{2} \Omega^2 \left(\frac{d^2k}{d\omega^2} \right)_{\omega=\omega_c} + \dots = \\ &k_c + \Omega k'(\omega_c) + \frac{1}{2} \Omega^2 k''(\omega_c) + \dots, \end{aligned} \quad (2.1.15)$$

where $\Omega \ll \omega_c$. We therefore have a rapidly oscillating carrier, and a slowly oscillating envelope [Zin98]. The phase velocity is given by $v_{ph} = \frac{\omega_c}{k_c}$. The group velocity v_g denotes the velocity of the envelope given by

$$v_g = 1 / \left(\frac{dk}{d\omega} \right)_{\omega=\omega_c}. \quad (2.1.16)$$

We can now introduce a dispersion function, which contains terms higher than the first order in (2.1.15) [DrJ05]:

$$D(\Omega) = \sum_{m \geq 2} D_m \Omega^m; \quad (2.1.17)$$

with the dispersion coefficients

$$D_m = \frac{1}{m!} \left(\frac{d^m k(\omega)}{d\omega^m} \right)_{\omega=\omega_c}. \quad (2.1.18)$$

For the analysis of the FDML laser in later chapters, the second- and higher order dispersion coefficients will play a crucial role in understanding the properties of FDML dynamics.

2.2 Linear and nonlinear media

In linear isotropic media, we have the relation $\vec{P} = \epsilon_0 \chi \vec{E}$ fulfilled, where χ is the scalar susceptibility. In linear anisotropic media however, we find

$$P_i = \sum_j \epsilon_0 \chi_{ij} E_j; \quad (2.2.1)$$

with the susceptibility tensor χ_{mn} . The electric field and the polarization can now have different directions with respect to each other. For anisotropic, nonlinear materials we can write the relation for linking the polarization and the field as a Taylor series [Abr70]:

$$P_i = \epsilon_0 \left[\sum_j \chi_{ij}^{(1)} E_j + \sum_{jk} \chi_{ijk}^{(2)} E_j E_k + \sum_{jkl} \chi_{ijkl}^{(3)} E_j E_k E_l + \dots \right]. \quad (2.2.2)$$

The susceptibility tensors have different orders, where $\chi_{ij}^{(1)}$ denotes the linear susceptibility, $\chi_{ijk}^{(2)}$ is the second order susceptibility. The Pockels effect [Poc68], for example, is a second order effect. The Kerr effect, discussed in the next subsection is for example an effect of the third order susceptibility $\chi_{ijkl}^{(3)}$ [Agr06].

2.2.1 Kerr effect

If the refractiveindex is dependent on the pulse intensity, we can split the refractiveindex into twoparts, one that behaves like in (2.1.11), and one that is dependent on the intensity. We can then write as an approximation[Kae05]:

$$n = n(\omega, |A|^2) \approx n_0(\omega) + n_{2,L} |A|^2. \quad (2.2.3)$$

The pulse envelope $A(z, t)$ is here normalized, so that $|A|^2$ is the intensity of the pulse. The intensity dependent refractive index is denoted by $n_{2,L}$. As a consequence of the Kerr effect, we have to discuss the self-phase modulation, that also plays an important role in the FDML laser.

2.2.2 Self-phase modulation

As a consequence of the Kerr effect, $n_{2,L}$ induces a phase-shift on the pulse envelope during the propagation of the pulse. We can introduce the self-phase modulation (SPM) coefficient $\gamma = k_c n_{2,L}$ and write for the field envelope

$$\frac{\partial}{\partial z} A(z, t) = i\gamma |A(z, t)|^2 A(z, t). \quad (2.2.4)$$

SPM only leads to a phase shift in the time-domain [Kae05], which means that in general only the spectrum of the pulse changes, not the intensity profile.

2.2.3 Nonlinear Schrödinger equation

The simplest form of a nonlinear Schrödinger equation (NSE) [Zak68][Zak74] can be found by combining the effects of second order dispersion and self-phase modulation, which yields the simplest form of a NSE:

$$i \frac{\partial}{\partial z} A(z, t) = D_2 \frac{\partial^2}{\partial t^2} A(z, t) - \gamma |A(z, t)|^2 A(z, t). \quad (2.2.5)$$

This equation has the form of a Schrödinger equation from quantum mechanics [Mes03]. For the case of $\vec{r} = z\hat{e}_z$, the wavefunction $\Psi(z, t)$ corresponds to the field envelope $A(z, t)$, and the potential $V(z, t)$ becomes in this case $-\gamma |A(z, t)|^2$. The potential is in this case dependent on the intensity of the field envelope itself, therefore the equation is called nonlinear. The NSE can now be analogously derived for additional physical effects. In the simplest case of (2.2.5), analytical solutions to this differential equation can be found [Has73] for anomalous dispersion. In this case, the SPM and the dispersion act on the pulse, both counteracting the effects of one another and leading to a stable pulse formation. These steady-state solutions are called solitons. Nonlinear Schrödinger equations can now be found for more complex scenarios by investigating the effect of a physical quantity on the field envelope $A(z, t)$. Assuming that the effects act simultaneously on the optical system, the NSE can be accordingly derived by adding up the different effects into the NSE. For example, we can add the effect of a gain medium, arriving at

$$i \frac{\partial}{\partial z} A(z, t) = ig \left(z, i \frac{\partial}{\partial t} \right) + D_2 \frac{\partial^2}{\partial t^2} A(z, t) - \gamma |A(z, t)|^2 A(z, t).. \quad (2.2.6)$$

Here, we made use of a property of the Fourier transform (see Appendix A.1), where the gain $g(z, \omega)$ in the frequency domain becomes $g(z, i \frac{\partial}{\partial t})$ in the time domain.

In this manner, more complex NSEs can be derived, describing more complex optical systems. For FDML operation, we have a NSE that takes into account all physical effects that occur within the laser, see chapter 3.3.

Chapter 3

Fourier domain mode-locking: Applications, experimental setup, governing equation and numerical simulation

First, typical applications are presented, where the FDML laser is of great benefit, even surpassing currently available options with respect to performance. Such applications are in general sensing applications, where the high frequency swept infrared light with a large tuning range is of benefit. Besides using FDML lasers for thermometry [Kra07], or for the detection of chemicals [Kra07B], the main focus lies on the applications in optical coherence tomography (OCT). This procedure is analogous to ultrasound sonography but with electromagnetic waves instead of sound waves. This technique allows for ultra-high resolution images of biological tissue in real-time in vivo, with unprecedented detail and frame-rates [Hub10]. With a coherence length of up to 2.1 cm, the limitation of FDML lasers having a too low coherence length of only a few millimeters, has recently been overcome [Adl11], enabling much deeper scanning of biological tissue than previously possible. With possibilities of future optimizations, new fields for FDML lasers could open up, enabling a whole new range of potential applications. In the following, a typical setup of an FDML laser is shown, on which our work is based, except for the laser setup which is used for the pulse compression in Chapter 6. In Chapters 4 and 5, every comparison with experimental data is done using measurements performed with this FDML setup. We derive the central FDML governing equation from the nonlinear Schrödinger equation (NSE) ansatz presented in the previous chapter, which will be the central governing equation in this thesis. We then present the numerical simulation that is used to solve the FDML evolution equation, using a split-step Fourier method [Agr06]. Because a straight-forward

simulation is inhibited in the case of an FDML laser, we do a transformation from the laboratory frame into the reference frame of the tunable bandpass filter, in order to greatly reduce the computational effort.

3.1 Applications of FDML lasers

3.1.1 Chemical detection and sensing applications

FDML lasers have several benefits that make them a good choice in general for sensing applications that require infrared light with a very large tuning spectrum and high frequency sweep speeds. With the limitation of FDML lasers recently overcome, being that the coherence length is now up to 2.1 cm [Adl11], the imaging depth is greatly increased, making FDML lasers not only a feasible option for biological imaging applications, but for sensing applications in general.

FDML lasers have recently been used for engine gas thermometry [Kra07], where they are used to investigate molecular absorption spectra in an engine. Here, the low-noise and high speed properties of the FDML laser enable real time spectroscopy with a data acquisition speed of about 100 kHz. Aside from engine gas thermometry, the real-time investigation of molecular absorption spectra would also allow FDML lasers for the detection of chemicals in general [Kra07B], for example for the finding of explosive chemicals in security.

3.1.2 Optical coherence tomography

The main application of FDML lasers however, is for biological imaging applications such as optical coherence tomography (OCT) [Sch99][Fer93][Swa93], where a rapidly swept laser source with a large spectral tuning range is of great benefit [Hub06]. In its main application, OCT, the FDML laser is far superior to standard tunable laser sources, because of the much higher sweep speed. This is possible, because in FDML lasers, the sweep speed is only limited by the mechanical response time of the FDML laser, and not by the buildup time of lasing in the cavity as in the standard tunable laser. Here, the lasing has to build up repetitively from noise successively after each roundtrip. The maximum achievable sweep speed is thus limited by the buildup time of lasing within the cavity. Because this is overcome in FDML lasers, sweep speeds in the MHz range have recently been achieved, and tuning ranges of over 200 nm [Wie10]. This enables in this case high quality 2D and 3D scans of biological samples in vivo and in vitro at a very high scanning speed. The acquired resolution is in the range of $\approx 10 \mu\text{m}$.

In OCT, a long wavelength (typically near infrared) light source with a low coherence length is pointed towards a biological sample that is to be analyzed. Because the coherence properties of the light are destroyed when it is refracted on the sample, only the non-refracted light retains its coherence properties. With an interferometer, the scattered light is then overlapped with the non-scattered light and by means of Fourier analysis of the interference pattern, the initial image of the sample can then be reconstructed.

This technique is analogous to the principle of ultrasound scanning [Don58], only with coherent electromagnetic waves instead of sound waves [Hua91]. The reflective profile of a sample is called an A-scan or axial scan [Kim11], which represents the reflected amplitude of the light along the optical propagation axis. This terminology is directly derived from the ultrasound terminology, because this technique is older than the OCT technique, but based on the same imaging principles with sound waves instead of light waves. In B-scan mode [Per00], the brightness of the image represents the amplitude of the reflected light. In this mode, a cross-sectional image is acquired, by combining a number of a-scans. A greyscale image then shows the amplitude of the reflected light, revealing the structure of the biological sample. In C-scan or "en face" imaging mode [Pod04], structures are visualized, that have the same optical delay. Some benefits of OCT include the high acquired resolution in the micrometer range, the capability of direct imaging of the tissue without need of previous preparation ("in vivo") and the non-hazardous attributes of the used optical waves. Here, FDML proves to deliver even more benefits, allowing with its coherence length a scanning depth of up to centimeters [Adl11], and with its very high sweep speeds, a very high data acquisition rate, which in turn translates to a high frame-per-second count. As in regular OCT, the samples can be scanned also "in vivo", because of the very low energy of the laser light in the mW regime, which is also diffuse when used for OCT. Special fields are for example ophthalmology where it can be used to obtain detailed images from a human eye in motion. In general, it can be applied to all biological samples. In Fig. 3.1.1, an OCT image is shown for an "in vivo" image of a human finger [Hub06]. The resolution of this image is 4096x1024, and the axial scanning rate is 42000 axial scans per second which corresponds to 0.097 s per image. With 10 frames per second and such a high resolution, FDML delivers unprecedented image properties. This is only possible due to the very high data acquisition rates that the high sweep speeds of FDML lasers allow.

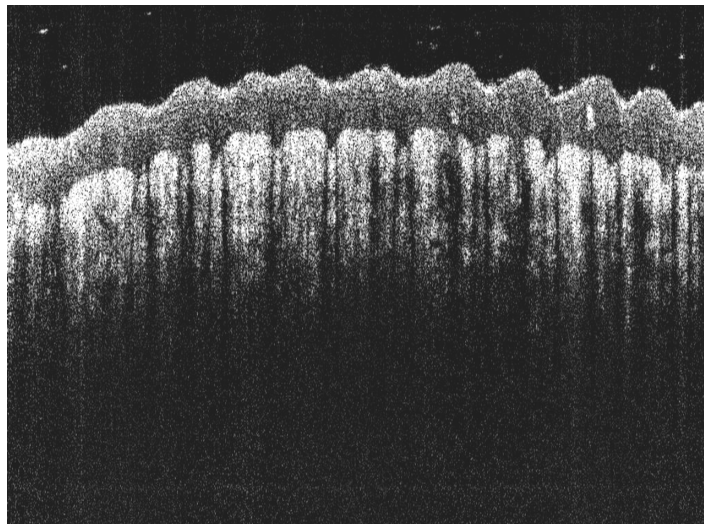


Figure 3.1.1: Image of a human finger "in vivo". The image resolution is 4096x1024 pixels which is acquired in 0.097 s. This corresponds to 42000 axial scans per second and 10 frames per second. Image courtesy of Robert Huber (Ludwig-Maximilians Universität München).

Newer FDML OCT setups enable even better performance. As shown in [Wie10], OCT setups with sweep ranges of up to 5.2 MHz can deliver scanning rates of about 20 million axial scans per second. 3D scans of biological tissue posed until recently a high challenge, because the acquisition time was too long or the 3D data sets were unevenly distributed in each of the three dimensions. For high definition, real-time 3D scans, very large data sets of up to 4.5 GVoxels/s are acquired. In Fig. 3.1.2, three OCT images of the human finger are shown at different data acquisition speeds [Wie10].

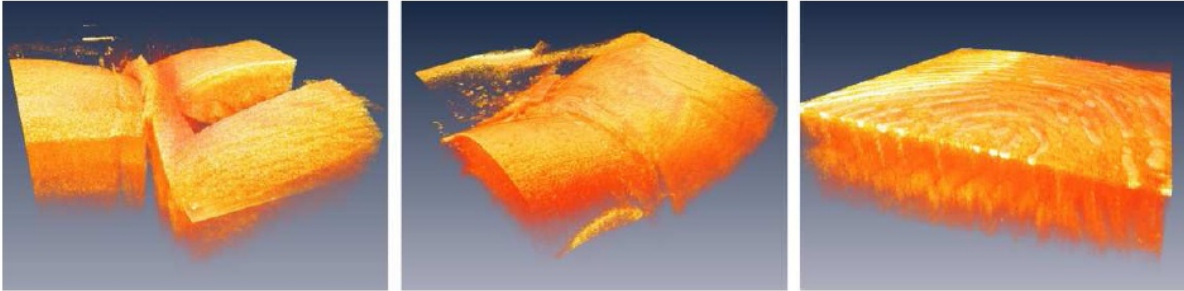


Figure 3.1.2: Examples of 3D images acquired by an FDML OCT setup as in [Wie10] with different setups. The left image is an OCT image of the human finger near the nail acquired at a 1 MHz scanning rate. The image in the middle is at a scanning range of 2.6 MHz. The right image is taken using a setup that operates at 5.2 MHz scanning rate. Images courtesy of Robert Huber (Ludwig-Maximilians Universität München)

A field where OCT is especially suited for imaging is in retinal OCT, where the human eye can be scanned "in vivo" without potential risks. Here, FDML laser setups provide the necessary high data acquisition rates, with over 1 million axial scans per second (1.37 MHz scanning rate)[Wie10]. Such high speeds enable the acquisition of wide-field, densely packed data sets within only a few seconds. The resolution of this setup is $11 \mu\text{m}$ at 684 kHz scanning speed or $19 \mu\text{m}$ at 1.37 MHz. As shown in Fig. 3.1.3, the images acquired by the FDML setup in [Wie10] provide a very high detail of the macula of the human eye, an oval shaped spot near the center of the retina. Here, the two setups are compared, both consisting of 1900x1900 axial scans.

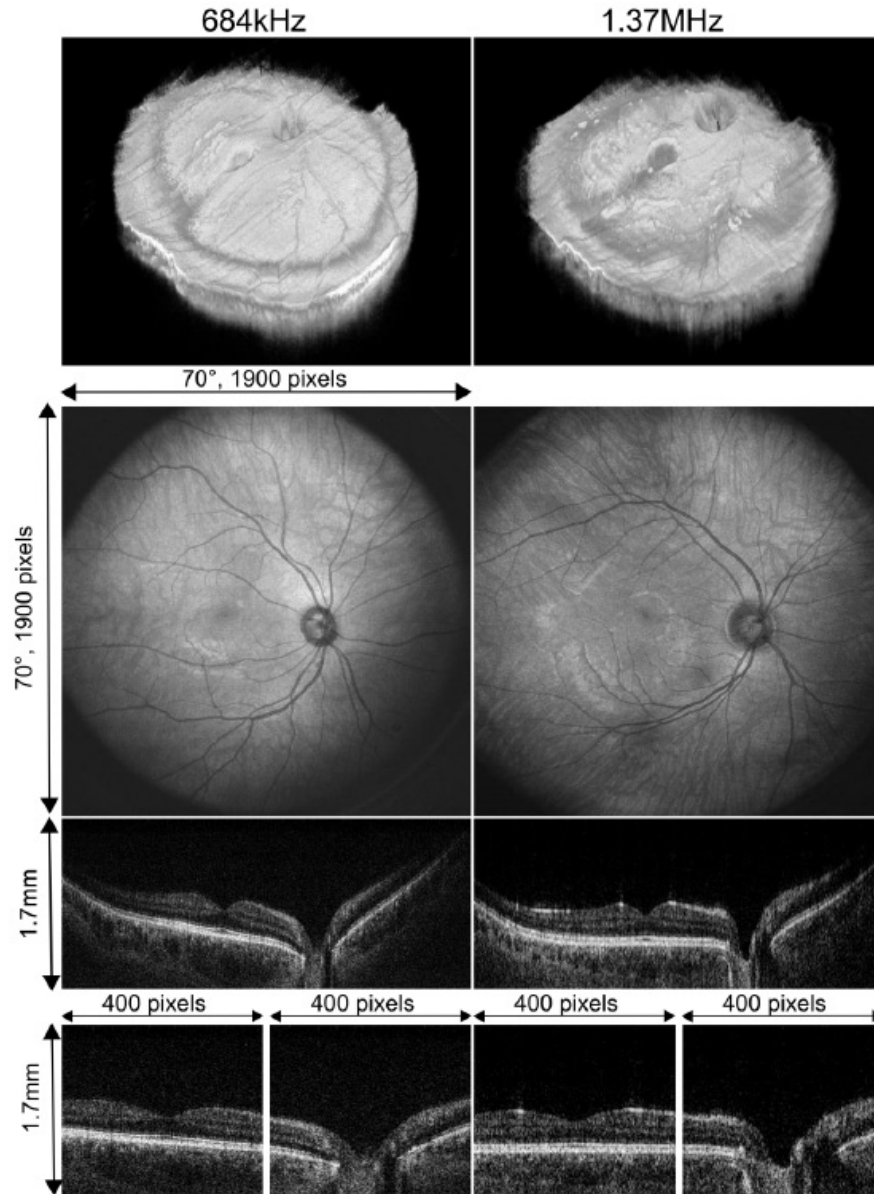


Figure 3.1.3: The top image shows a rendering of the 3D data set acquired by the FDML setup in [Wie10]. The data set consists of 1900x1900 axial scans and an ultra-wide imaging field of 70°. The middle pictures show a reconstruction of the macula in front view. The second last row shows a cross-sectional image through the macula and the optic disc. The bottom row shows enlarged images of the macula and the optical nerve. Images courtesy of Robert Huber (Ludwig-Maximilians Universität München).

3.2 Experimental setup of the FDML laser used for our simulations

Fourier domain mode-locking is achieved in our case by the implementation of a tunable narrow bandpass filter (FFP-TF, Lambda Quest, LLC.) with a bandwidth of 0.15 nm into a fiber laser ring geometry,

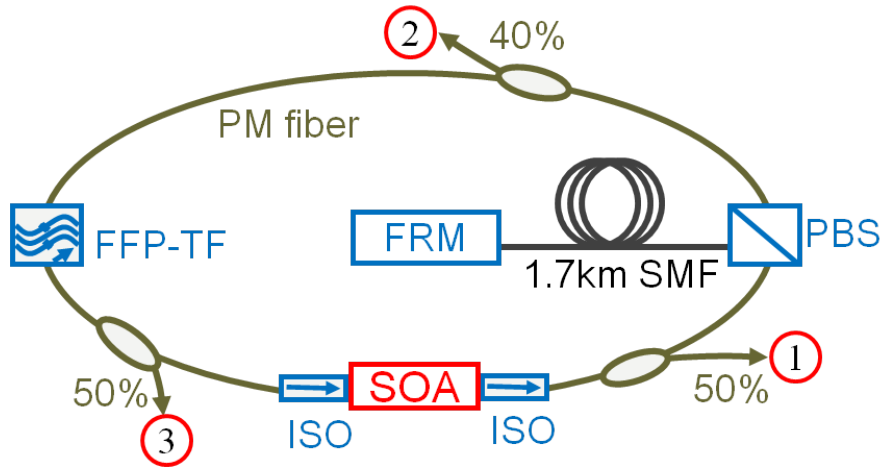


Figure 3.2.1: Experimental setup of FDML laser. The central elements are the tunable Fabry-Perot narrow bandpass or sweep filter (FFP-TF), the solid state optical amplifier (SOA) as a gain medium, and the 3.4 km single mode fiber (SMF) delay line. This laser has a center wavelength of 1320 nm, a sweep frequency of 57 kHz, and a tuning range of 105 nm.

with a solid state optical amplifier (SOA, Covega Corp., "BOA 1132") as a gain medium and a single mode fiber (SMF) as a delay length. The setup used for this thesis is shown in Fig. 3.2.1. The filter is driven around a center wavelength of 1320 nm. The tuning range is 105 nm, and the sweep frequency is 57 kHz. This corresponds to a roundtrip time of $17.32 \mu\text{s}$ of the laser light in the cavity. The roundtrip time is directly proportional to the length of the SMF. In this setup, the length of the delay line is doubled by the implementation of the Faraday rotating mirror (FRM), after the light has passed through the polarizing beam splitter (PBM). This beam splitter maintains the polarization of the laser light. In addition the elements are connected by a polarization maintaining (PM) fiber. Light can be coupled out at three different points within the laser cavity, which is useful for the analysis of the optical field dynamics in Chapter 4. The first one is after the SOA, where 50 % of the light is coupled out, the second one is after the SMF, where 40 % is coupled out, and the third one is after the sweep filter, where 50 % of the light can be coupled out. If for example, the light after the SOA is analyzed, the other outcouplers remain deactivated, so that only outcoupler number 1 would couple out light. This can be done analogously for the other outcouplers. To ensure unidirectional lasing, and to reduce light scattering within the fiber, two optical isolators (ISO) are mounted directly before and after the SOA.

The sweep filter itself is driven sinusoidally, or can be alternatively driven with any periodic function such as sine, cosine and ramp- or step-functions. The period of this filter drive function is chosen such, that it exactly matches the roundtrip time of the laser light. The roundtrip time is in turn determined by the distance the light travels within the cavity, which in this case is two times the length of the SMF fiber (3.4 km). A shorter SMF would directly result in a shorter roundtrip time and a higher sweep frequency. Basically, the upper limit is only given by the mechanical response time of the sweep filter. This overcomes the limitations in standard tunable lasers, where the maximum sweep frequency

is limited by the buildup time of the lasing, enabling far higher sweep frequencies. Sweep frequencies for OCT applications typically range from several 100 kHz [Jeo08], to frequencies beyond 5 MHz [Kle11], that have recently been achieved.

The sweep filter, with its bandwidth of 0.15 nm, lets only modes of the wavelength pass, that are within this narrow transmission window. Therefore, only light waves are allowed that have a certain frequency at a certain time. This leads to a fixed phase relationship directly in the frequency domain, hence the name Fourier domain mode-locking. In contrast to standard mode-locked lasers, the FDML laser emits a train of highly chirped pulses, producing a cw output.

In this setup, the sweep filter is driven with the angular driver frequency $\omega_0(t) = -\frac{\Delta\omega}{2}\cos(\omega_s t)$. The filter drive function is shown in Fig. 3.2.2. As can be seen, it is symmetrical around the center angular frequency of $1.428 \cdot 10^{15} \text{ s}^{-1}$, corresponding to 1320 nm.

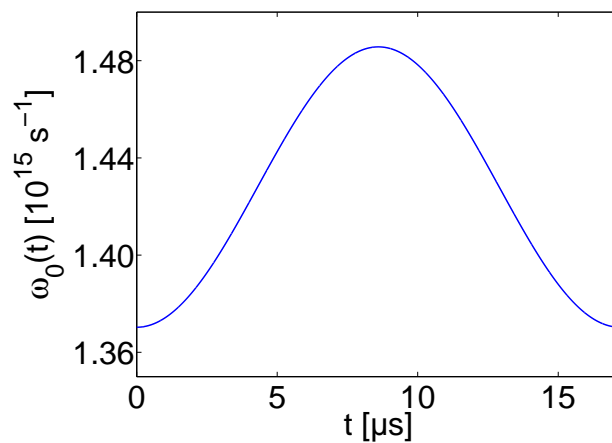


Figure 3.2.2: The filter is driven with an angular frequency of $\omega_0(t) = -\frac{\Delta\omega}{2}\cos(\omega_s t)$, with ω_s being the sweep frequency of 57 kHz. The center frequency of the sweep is 1320 nm.

3.3 FDML equation

This system can be described by a nonlinear Schrödinger equation in the slowly varying amplitude approximation [Agr06]. As described in chapter 2.2.3, the NSE Ansatz can be modified in order to incorporate the physical effects that take place within a laser. The simplest example of a NSE in optics is for a laser where there acts only second order dispersion and self-phase modulation simultaneously on the envelope $A(z, t)$, as in (2.2.5). However, in an FDML laser, several effects occur that have to be taken into account. The FDML equation for the complex field envelope $A(z, t)$ in the laboratory frame can be written as [Jir08]:

$$\frac{\partial}{\partial z} A(z, t) = \left[g \left(z, i \frac{\partial}{\partial t} \right) (1 - i\alpha) - a \left(z, i \frac{\partial}{\partial t} \right) - iD_2(z) \frac{\partial^2}{\partial t^2} + D_3(z) \frac{\partial^3}{\partial t^3} + i\gamma(z) |A(z, t)|^2 \right] A(z, t); \quad (3.3.1)$$

This equation is a partial differential equation with respect to the retarded time t and the propagation direction along z . This simplification can be done because this is a fiber laser where the transverse mode profile is approximately constant. Therefore we can assume a 1-dimensional propagation direction. The coefficient α describes the Henry- or linewidth enhancement factor [Hen82], D_2 and D_3 are the second- and third order dispersion coefficients and γ is the self-phase modulation caused by nonlinear optical propagation, as discussed in chapter 2.2.2. It has only a constant, non-zero value in the delay fiber and vanishes in the other laser components. The gain and loss in the laser have also to be taken into account and are described by $g(z, i \frac{\partial}{\partial t})$ and $a(z, i \frac{\partial}{\partial t})$. They are functions of the position z but also of the frequency in the Fourier domain. Inverse Fourier transforming this frequency dependency to the time-domain, yields the dependency on $i \frac{\partial}{\partial t}$, which is a mathematical property of the Fourier transform (See Appendix A.1). As will be seen in the next section, a straight-forward numerical simulation based on (3.3.1) is not possible because of the huge time-bandwidth product of this laser setup. Therefore, in order to reduce the numerical complexity of this problem, a transformation of the complex field envelope $A(z, t)$ into the reference frame of the sweep filter is needed. This reference frame is now moving along with the sweep filter center frequency as seen in Fig. 3.2.2. Because the spectral width of the sweep filter is with 0.15 nm only 0.1% of the tuning range of 105 nm, we can greatly reduce the time-bandwidth product by a factor of 1000. The instantaneous frequency of the carrier wave is now adjusted to the sweep filter position, it therefore gives the transformation for the complex field envelope into the new reference frame [Jir08]:

$$u(z, t) = A(z, t) \exp \left(i \int^t \omega_0(t') dt' \right). \quad (3.3.2)$$

Inserting this relation into (3.3.1) yields the tranformed FDML equation

$$\begin{aligned} \frac{\partial}{\partial z} u(z, t) = \exp \left(i \int^t \omega_0(t') dt' \right) & \left[g \left(z, i \frac{\partial}{\partial t} \right) (1 - i\alpha) - a \left(z, i \frac{\partial}{\partial t} \right) - iD_2(z) \frac{\partial^2}{\partial t^2} + D_3(z) \frac{\partial^3}{\partial t^3} \right] \\ & \cdot \exp \left(-i \int^t \omega_0(t') dt' \right) \left[i\gamma |u(z, t)|^2 - a_s \left(i \frac{\partial}{\partial t} \right) \right] u(z, t). \end{aligned} \quad (3.3.3)$$

The sweep filter loss is described by $a_s(i \frac{\partial}{\partial t})$. In the frequency domain, the sweep filter can be implemented as a static loss coefficient $a_s(\omega)$. The sweep frequency f_s is in our setup slow, so that the two terms $\propto u \frac{\partial}{\partial t} \omega_0$ and $\propto \omega_0 \frac{\partial}{\partial t} u$ can be neglected, which further simplifies the FDML evolution equation. The spectral width of u is now given by the narrow sweep filter bandwidth and not by the bandwidth induced by the whole sweep range. Therefore, we can assume that the frequency dependent gain and loss of

(3.3.1) do not change much over the frequency range of the transformed field envelope $u(z, t)$. We then arrive at a simplified FDML evolution equation in the swept-filter reference frame, which is the central equation also for other theoretical and numerical considerations in later chapters:

$$\frac{\partial}{\partial z} u(z, t) = \left[g(\omega_0)(1 - i\alpha) - a(\omega_0) + i\omega_0^2 D_2 + i\omega_0^3 D_3 - iD_2 \frac{\partial^2}{\partial t^2} + i\gamma |u|^2 - a_s \left(i \frac{\partial}{\partial t} \right) \right] u(z, t). \quad (3.3.4)$$

The filter drive function depends on time, $\omega_0 = \omega_0(t)$ (Fig. 3.2.2). This simplified equation is much more accessible for numerical simulations and is used in the next section as a basis for that. In the next section, a numerical simulation is presented for solving (3.3.4).

3.4 Numerical simulation

3.4.1 Split-step Fourier algorithm

The huge time-bandwidth product in (3.3.1) of $17.32 \mu\text{s} \cdot 18 \text{ THz}$ would require about $3 \cdot 10^8$ grid points for the simulation, an amount too large to be feasible currently. The FDML equation in the swept-reference filter frame (3.3.4) on the other hand, requires a considerably lower amount of grid points for computation. By the transformation, the amount of necessary grid points has been reduced by a factor of about 100. Because the filter blocks all light far outside the passband, not the entire spectral sweep bandwidth has to be taken into account; instead, a spectral window of 2.8 nm around the filter center frequency is here considered, corresponding to 500 GHz. Since the temporal simulation window is adapted to the roundtrip time $T=17.32 \mu\text{s}$, due to the implicit periodic boundary conditions of the algorithm [Jir08], the frequency resolution is $f=1/T=57.7 \text{ kHz}$. Thus, about 8 million grid points are used, as compared to 300 million without switching to the swept-filter reference frame. The 8 million grid points are used in a split-step Fourier method [Agr06] with the FFTW algorithm [Fri05] to simulate the FDML laser on the basis of (3.3.4). The number of grid points has been chosen as a power of 2 ($2^{23} \approx 8 \text{ million}$), because the FFTW algorithm requires a power of 2 in order to reduce the computing time. The basic idea of the split-step Fourier scheme is to split up a general partial differential equation into a linear and a nonlinear part. The simplest NSE from Chapter 2.2.3 for example, can be written as

$$\frac{\partial}{\partial z} A(z, t) = \left(\hat{L} + \hat{N} \right) A(z, t); \quad (3.4.1)$$

where \hat{L} denotes the linear part given by the second-order dispersion, and \hat{N} denotes the nonlinear part given by the self-phase modulation. The same also applies for (3.3.4), only with greater complexity. The self-phase modulation and the gain saturation in the FDML laser are nonlinear effects, whereas the other parts of (3.3.4) are linear effects. The solution is then computed in small steps, while the linear and the nonlinear parts are treated separately [Agr06]. Because the linear part is computed in the time domain,

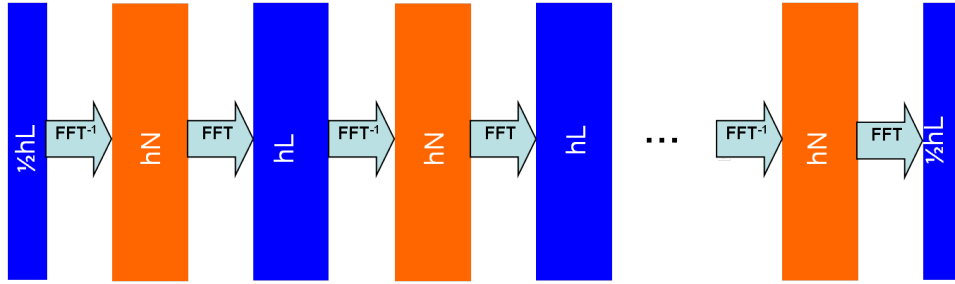


Figure 3.4.1: The split-step Fourier method splits a nonlinear partial differential equation into linear and nonlinear parts, which are treated consecutively in the time and in the frequency domain. The step size is h , while L and N denote the linear and nonlinear part of the differential equation, in our case 3.4.1.

and the nonlinear part is treated in the frequency domain, the solution is acquired by consecutively Fourier transforming and back-transforming in small steps. This is visualized in Fig. 3.4.1, where L and N denote the linear and nonlinear parts, respectively, and h is the step size. At the beginning and at the end we have to be in the time domain, therefore the step size here is only half the step size h . The resolution of 8 million grid points means that the process of consecutive Fourier and inverse Fourier transforms takes place 8 million times.

3.4.2 Implementation of the various elements of the FDML laser

The SOA is implemented as a lumped element in the simulation, which means that the SOA that has a spatial elongation, is treated as a point-like structure. By integrating over the length of the SOA, we obtain the amplitude gain G given by

$$G = e^{\int^z g dz'}. \quad (3.4.2)$$

For modeling the gain, the spectral gain profile of the SOA is experimentally determined, as well as the frequency dependent saturation behavior. This is shown in Fig. 3.4.2. There, the spectral gain profile for different incident powers of the optical light field as measured in the experiment is shown. Another effect that has to be taken into account when modeling the gain, is the gain recovery dynamics. We use a quasi-instantaneous gain saturation model [Jir08] in order to take into account the following two effects: First, the carrier lifetime τ_c in the SOA is much faster than the optical power modulations that are caused by tunable bandpass filter. Secondly, optical fluctuations caused by ASE can be faster than τ_c . This circumstance is taken into account by a moving average value for the optical power $P_{av}(t)$ instead of the power $P(t)$:

$$P_{av}(t) = \tau_c^{-1} \int_{-\infty}^t P(\tau) e^{\frac{\tau-t}{\tau_c}} d\tau; \quad (3.4.3)$$

where τ_c acts as an exponential memory decay time [Jir08]. For the carrier lifetime and the Henry factor, typical values are implemented, $\tau_c = 380\text{ps}$ and $\alpha = 5$ [Bil06].

ASE has two effects: The simulation can self-start from ASE, and a constant noise floor is added to the output of the laser. We take a noise source with a constant spectral power density P_f at the SOA input, which is then implemented as additive white Gaussian noise [Cas00]. The spectral power of the noise source is experimentally measured to $P_f = 3.2$ mW. Also, the gain properties of the SOA and the overall cavity power loss have been carefully measured, and the results are also implemented into the simulation. The gain and loss curve with the frequency dependency and also the power saturation properties of the gain, are shown in Fig. 3.4.2.

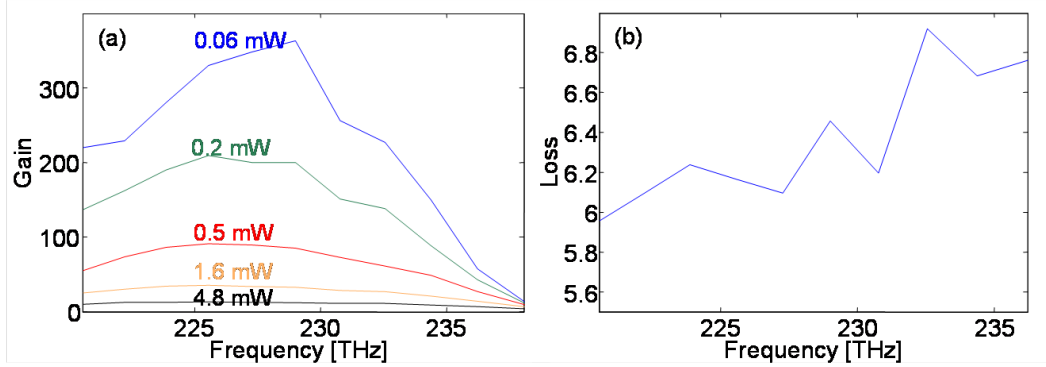


Figure 3.4.2: (a) Experimentally measured SOA power gain (linear scale) as a function of the optical frequency for different values of the incident optical power. (b) Experimentally measured overall cavity power loss (linear scale) as a function of the optical frequency. The sweep filter has been tuned to maximum transmission at each measured frequency.

The delay fiber is an SMF28 fiber, and is implemented according to the specifications from the manufacturer Corning, with the corresponding dispersion, loss, and self-phase modulation. The self-phase modulation has a value of $\gamma = 0.00136$ W⁻¹m⁻¹, and the second and third order dispersion coefficients are $D_2 = -2.7603 \cdot 10^{-28}$ s²/m and $D_3 = 1.2183 \cdot 10^{-41}$ s³/m, respectively.

The last element of the FDML laser, that has to be modeled is the sweep filter. It is modeled also as a lumped element (like the SOA), which has a Lorentzian transmission characteristic:

$$t_s = e^{-\int a_s dz} = \frac{\sqrt{T_{max}}}{\left(1 - \frac{2i\omega}{\Delta}\right)}; \quad (3.4.4)$$

with $\Delta = 169$ ps⁻¹ and $T_{max} = 0.5$.

The total loss in the laser cavity $a(\omega)$ is a function of the frequency and has also been experimentally measured and built into the simulation [Jir08].

The simulation typically converges after a few hundred roundtrips, and convergence is ensured in the time, as well as in the frequency domain by consecutively comparing the simulated outputs for each roundtrip. Small fluctuations are remaining from the ASE noise, so that the output has very small changes from roundtrip to roundtrip. All laser parameters are taken either from literature or retrieved directly from the experiment. This means that the simulation is totally self-consistent, it thus does not

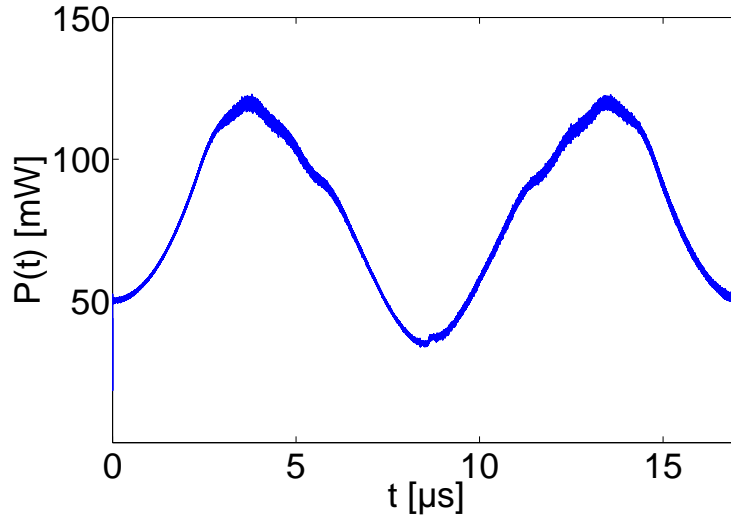


Figure 3.4.3: Simulated power output for an FDML laser centered at 1320 nm with a sweep range of 105 nm, a roundtrip time of 17.32 μs , and a filter drive function according to Fig. 3.2.2.

depend on fitting parameters. A typical time-dependent power output of a simulation for the FDML laser centered at 1320 nm with a sweep range of 105 nm, a roundtrip time of 17.32 μs , and a filter drive function according to Fig. 3.2.2 is shown in Fig. 3.4.3. Based on the comparison of the simulated power output with the experimental data in [Jir08], a good agreement between theory and simulation is found, which will be continued in this thesis for other investigations of FDML properties.

3.4.3 C++ code

The code itself is written in C++, where a subroutine is written for every element of the laser. The basis of the whole simulation is the complex FFTW field, which is a complex valued array with the real part $u[0]$, and the imaginary part $u[1]$. This field is now consecutively computed for every element of the laser. The first element is the gain, and because the gain is a nonlinear effect, its effect on the field $u[0]$ and $u[1]$ is computed in the time domain. As already mentioned in the previous subsection, the gain curve has been experimentally obtained, together with its saturation behaviour. Also, the gain lifetime has been taken into account. These effects are implemented into the code accordingly, where the gain curve is calculated with a cubic spline interpolation routine from the experimental data points. Then, the effect on the fields is calculated in the time, and after that, the field is Fourier transformed into the frequency domain. Then, the field is fed into the next subroutine, representing the next element of the laser. This would in our case be the delay fiber. Because in the delay fiber, linear effects such as dispersion, and nonlinear effects such as SPM are acting on the complex field $u(z, t)$, the linear part is treated in the subroutine for dispersion, and the nonlinear part in another subroutine. Here again we have the principle that the nonlinear part is treated in the time domain. Now, this consecutive Fourier transforming, and backtransforming is done for the 2^{23} or 8388608 grid points. So, the complex FFTW field is computed

for every element of the laser consecutively, starting with the gain, then the delay fiber and then the sweep filter. Every physical effect from the FDML evolution equation (3.3.4) is implemented accordingly, as explained in subsection 3.4.2. When the complex field has been computed after passing every single element of the FDML laser, meaning that every subroutine of the code has been passed, a complete roundtrip has been completed. Then, the field is passed into the first element of the laser again, starting the second roundtrip in the laser. This procedure can be applied infinitely many times, with convergence of the field typically achieved within a few hundred roundtrips. The output of the simulation, the complex FFTW field, is saved into a file, with a typical size of 230 MB, due to the large amount of grid points. The field is then read into Matlab, where the power can be easily plotted by calculating the absolute square $|u(z, t)|^2$ of the complex FFTW field. Convergence of the output is assured by plotting the power output consecutively for each roundtrip, with the point of convergence reached when the output does not change any more for different roundtrips.

The complex FFTW field saved into the 230 MB data files, is also the starting point for every later analysis, or simulation plot in this thesis. In Fig. 3.4.3 for example, the complex FFTW field is read into Matlab, and the absolute square of the field is plotted, giving the power over time. Later on, the field is computed in the Fourier domain, and segregated into smaller subintervals, in order to retrieve the instantaneous linewidth (see Chapter 4.2 and Chapter 5).

Chapter 4

Instantaneous lineshape analysis of FDML lasers

Using the previously presented FDML governing equation (3.3.4) from Chapter 3, the first goal of this chapter is to investigate the dependence of the FDML linewidth on cavity parameters and relevant physical effects. In contrast to the experiment, the numerical simulation allows us to change the laser parameters easily. We then can examine the effect that this change has on properties such as the instantaneous linewidth and thus the coherence length of the laser, which is inversely proportional to the instantaneous linewidth. The gained insight from this method of changing the laser parameters can then be used to find ways to increase the instantaneous coherence length from the mm range to the cm or m range in the future, enabling a whole new variety of biological and non-biological imaging and sensing applications. The second goal is to investigate if ASE and environmental instabilities ultimately limit the FDML linewidth performance, as in typical semiconductor based lasers.

The simulations are performed employing the procedure described in chapter 3. Linewidths around 10 GHz are found, which is significantly below the sweep filter bandwidth of 27 GHz [Tod11]. The effect of detuning between the sweep filter driver frequency and the cavity roundtrip time is studied revealing features that cannot be resolved in the experiment. Shifting of the instantaneous power spectrum against the sweep filter center frequency is also analyzed. It is then shown that in contrast to most other semiconductor based lasers, the instantaneous linewidth is governed neither by external noise sources nor by amplified spontaneous emission, but it is directly determined by the complex FDML dynamics. This is in contrast to other known laser sources and is found to be a specific property of FDML lasers.

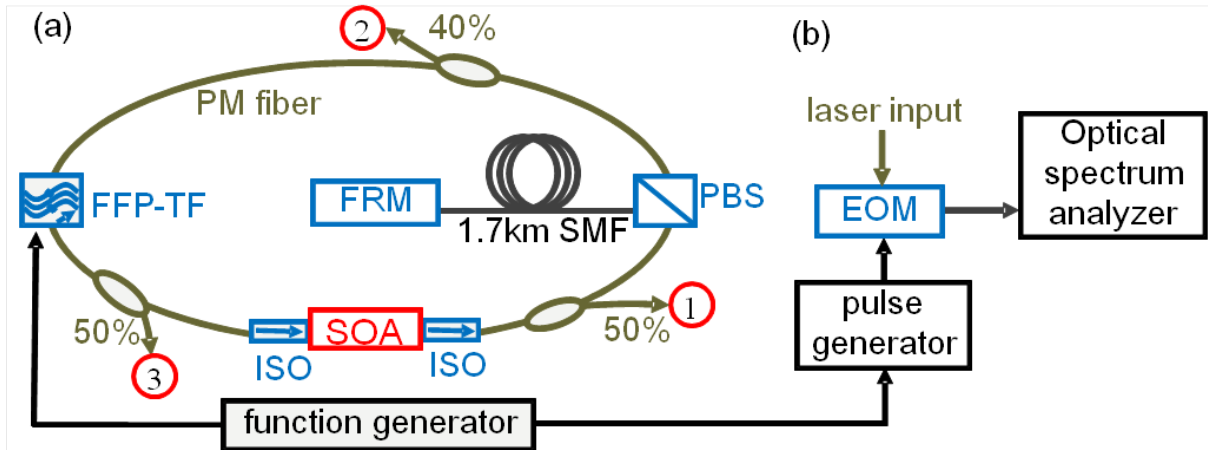


Figure 4.1.1: The experimental setup shown in (a) is the same as in Fig. 3.2.1, and in (b) the measurement of the instantaneous lineshape is performed. The function generator drives the sweep filter and is linked to a pulse generator, which in turn is coupled to the electro-optical modulator (EOM). The EOM takes the outcoupled light and feeds it then into the optical spectrum analyzer.

4.1 Experimental setup and measurement of the instantaneous linewidth

The experimental setup in 4.1.1(a) is the setup shown in Fig. 3.2.1, with a few additions for the measurement of the instantaneous lineshape, which is shown in Fig. 4.1.1(b). In swept laser sources, such as the FDML, the instantaneous linewidth is the most important parameter, because it determines the coherence length. In contrast to the time-integrated linewidth, the instantaneous linewidth is defined as the spectral linewidth that the laser emits at a given point in time. In order to measure the instantaneous linewidth experimentally, the setup of Fig. 4.1.1(b) is additionally employed.

As seen, the function generator drives not only the sweep filter, but also triggers a 1.6 ns pulse in the pulse generator (Picosecond Pulse Labs, model 2600). The pulse generator in turn is connected to the electro-optical modulator (EOM, Photline "MX13"), in such a way that it always cuts out a 1.6 ns long optical waveform at the same spectral position of the sweeps. The laser light can be coupled out at the three different points within the laser cavity, and is fed into the EOM, where the 1.6 ns gating of the laser light takes place. Several effects lead to a broadening of the measured instantaneous linewidth, compared to the numerical simulation. First, the optical spectrum analyzer has a finite resolution of 20 pm, corresponding to a spectral width of 3.5 GHz at 1310 nm. Furthermore, the 1.6 ns gating window leads to a Fourier broadening of 1 GHz according to the time-bandwidth product. Longer gating times would suppress this effect, but lead to considerable smearing of the linewidth due to the sweep filter dynamics. For a sweep filter driven by a cosine wave, the broadening has its maximum value of 3.81 GHz at 5.3 and 3.3 μs , whereas at 1.3 and 7.3 μs , it is only 1.85 GHz due to the slower sweep speed at that point. The combination of all these effects leads to a broadening of the experimentally measured spectrum by about 4-8 GHz compared to the theoretically calculated values.

4.2 Calculation of the instantaneous linewidth

The starting point for the analysis of the instantaneous linewidth is the FDML propagation equation (3.3.4) in the swept-filter reference frame. The experimental setup used for the simulation is the one presented in chapter 2. The simulation that is described in chapter 3, calculates the complex field envelope $u(z, t)$ of (3.3.4) in the swept-filter reference frame. The instantaneous linewidth can now be obtained from the simulation data by Fourier transforming the complex field envelope, yielding the instantaneous power spectrum $|u(z, f)|^2$, where f denotes the frequency with respect to the center frequency of the sweep filter. The duration T of one roundtrip can now be segregated into a given number of subintervals, and the instantaneous power spectrum at different times can be calculated by Fourier transforming $u(z, t)$ for each interval. Here, we divide the axis into 16 intervals of $1.08 \mu\text{s}$, summing up to the total roundtrip time of $17.32 \mu\text{s}$. This way we can simulate the temporal evolution of the instantaneous power spectrum. Because the simulation is performed in the swept-filter reference frame, the simulation is not broadened by the ongoing sweeping action during a time-gate as it is in the experiment. The instantaneous power spectrum is here computed after the SOA. The instantaneous linewidth corresponds to the full width at half maximum (FWHM) of the instantaneous power spectrum.

4.3 Results

4.3.1 Agreement with the experiment

In Fig. 4.3.1, the instantaneous power spectra are compared at different times t for the nondetuned case, where the sweep filter frequency matches exactly the roundtrip time. In Fig. 4.3.1(a), $t = 1.3 \mu\text{s}$, where the sweep filter center frequency varies only slowly, and in Fig. 4.3.1(b) $t = 3.3 \mu\text{s}$, where the cosine function is the steepest, thus the frequency changes fast. For this reason, the experimental spectrum in Fig. 4.3.1(b) is considerably broadened as compared to the simulated spectrum, with a full width at half-maximum (FWHM) of 12.07 GHz for the experimental result vs. 5.81 GHz for the simulation [Tod11].

For further validation, the detuned case is investigated, where the sweep filter is not completely synchronous to the roundtrip time of the light field in the laser cavity. A positive detuning means that the sweep filter is ahead of the light field, whereas a negative detuning means that the light field is ahead of the sweep filter in time. For the detuned case, also good agreement between theory and experiment is obtained under various conditions. In Fig. 4.3.2(a), Fig. 4.3.2(b) and Fig. 4.3.2(c), the instantaneous power spectrum is displayed at $t = 7.3 \mu\text{s}$ for zero, -2 Hz and + 2 Hz detuning, respectively. The detuning between the sweep period and the roundtrip time affects not only the time dependent output power [Jir08], but also the instantaneous power spectrum. More specifically, we observe a pronounced high-frequency tail for both negative and positive detuning, see Fig. 4.3.2(b) and Fig. 4.3.2(c). This

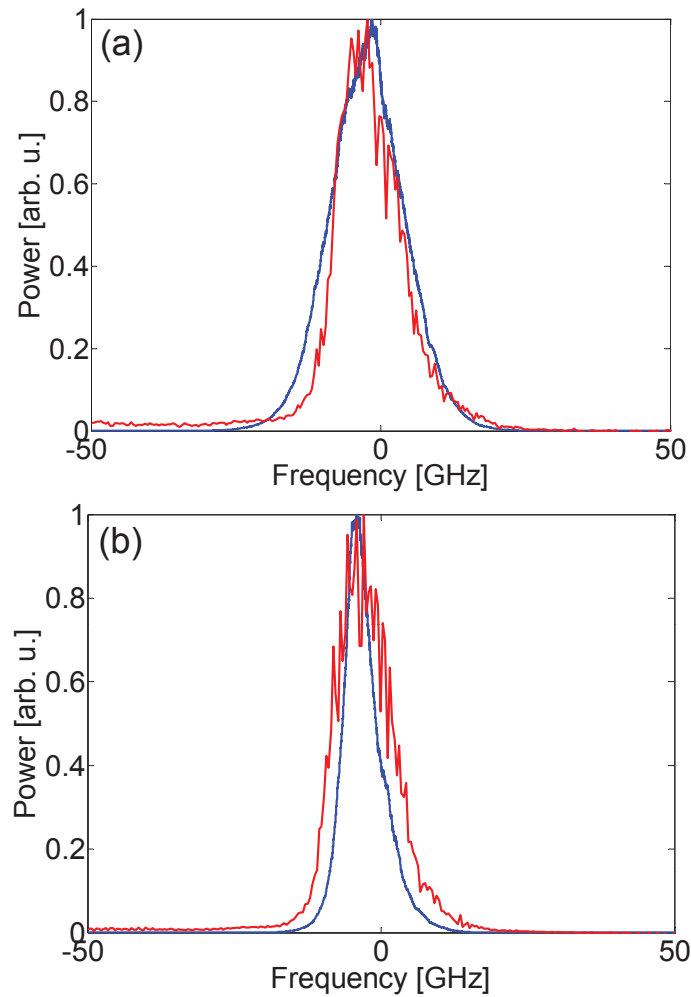


Figure 4.3.1: Experimental (red) and simulated (blue) instantaneous power spectra after the SOA at (a) $1.3 \mu\text{s}$ and (b) $3.3 \mu\text{s}$ for no detuning.

asymmetry gets reduced for a smaller amount of detuning, as can be seen by comparison with the non-detuned case shown in Fig. 4.3.1(a). The main source of this asymmetry is found to be the third order dispersion term D_3 . In chapter 5, we analyze the impact of the third order dispersion in more detail. In Fig. 4(b), the asymmetry manifests itself as a small side peak, which is not resolved in the experiment due to the limited resolution as discussed above [Tod11].

4.3.2 Timing offset, linewidth enhancement factor and spectral shift

In our simulation, where the frequency axis moves along with the sweep, a broadening of the instantaneous power spectrum due to the sweep filter dynamics is eliminated. Thus, we can analyze the instantaneous power spectrum averaged over the whole roundtrip time, which is not possible in the experiment. In the experimental setup, only small "cut-outs" of the output can be examined. In Fig. 4.3.3(a), the instantaneous power spectrum is plotted for zero detuning and with the laser parameters as in the experiment, where the linewidth enhancement factor is assumed to be $\alpha = 5$ (red) [Hen82] and $\alpha = 0$ (blue). The sweep filter transmission function is also shown for comparison. Figure 4.3.3(b)

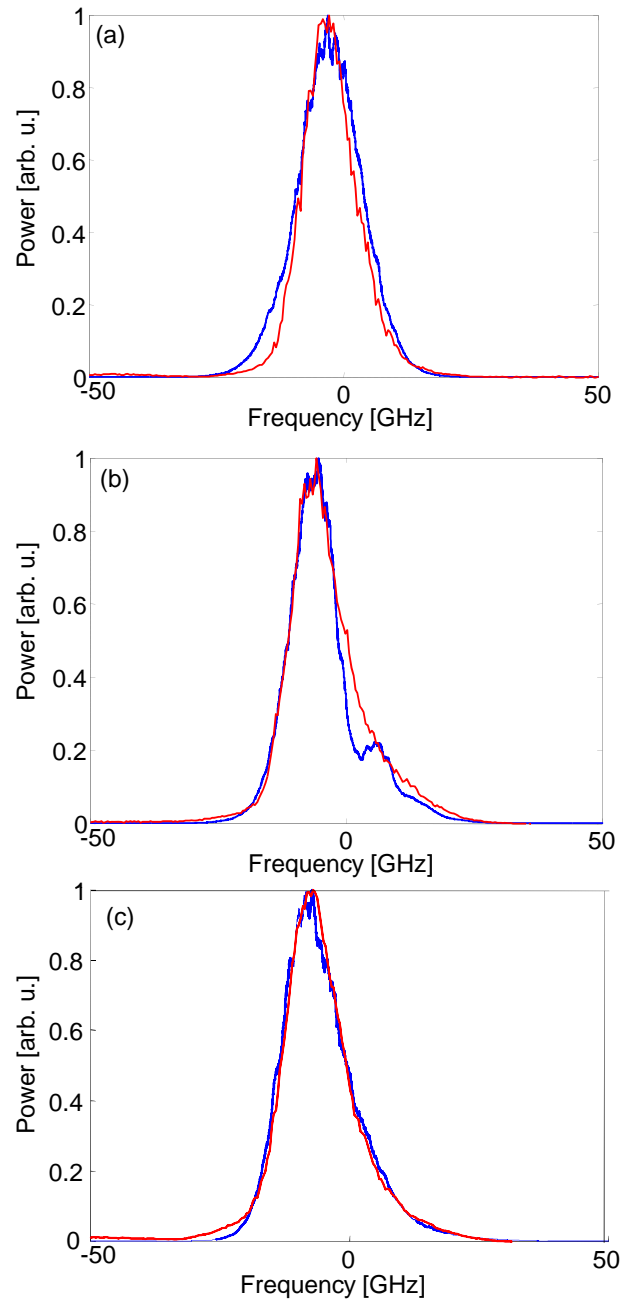


Figure 4.3.2: Theoretical (blue) and experimental (red) power spectra at $7.3 \mu\text{s}$ for (a) no detuning, for (b) a detuning of -2 Hz and for (c) a detuning of $+2 \text{ Hz}$.

shows the same simulation, but now with ASE only used at the start of the simulation to seed lasing. From Fig. 4.3.3(a) we can extract that the frequency shift of the power spectrum is due to the linewidth enhancement in the SOA, as also observed for conventional swept laser sources. The cause of this frequency shift is explained in detail in Chapter 5. There it is found that a combination of the linewidth enhancement and the carrier decay lifetime in the SOA are the sources of this phenomenon.

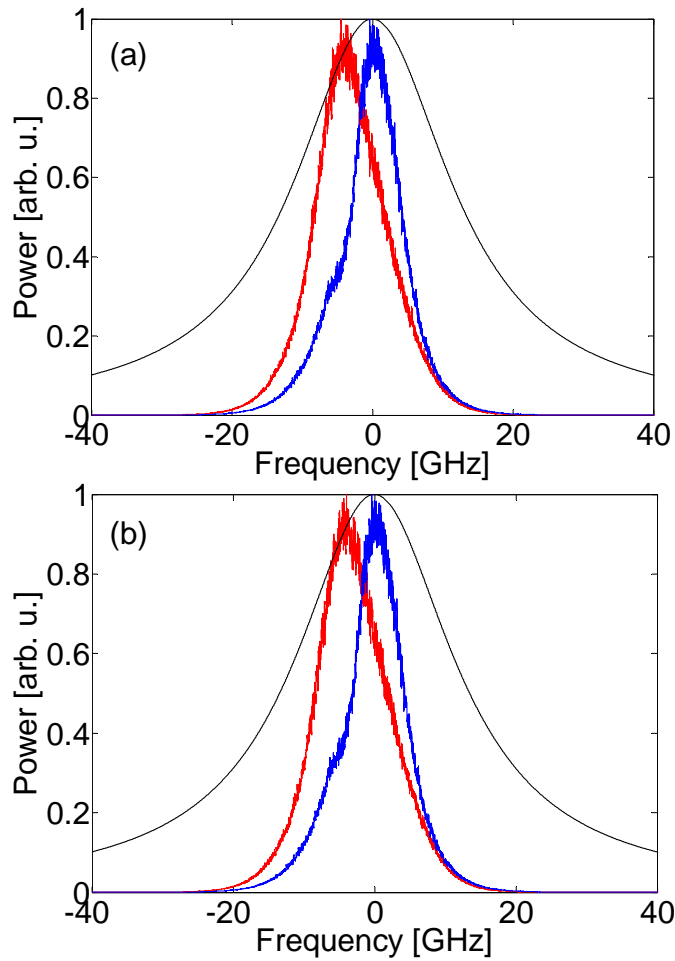


Figure 4.3.3: (a) Simulated instantaneous power spectrum for $\alpha = 5$ (red) and $\alpha = 0$ (blue), the sweep filter transmission function is drawn in black. (b) The instantaneous power spectrum for $\alpha = 5$ (red) and $\alpha = 0$ (blue) but without ASE.

Here, we additionally observe a significant broadening of the linewidth from 7.25 GHz (without ASE) and 7.41 GHz (with ASE) to 10.08 and 9.99 GHz, respectively, indicating that SOAs with low or optimized values for α might be preferred. This finding might also indicate that for light sources with very narrow instantaneous linewidth, post amplification as presented in [Hub05B] might lead to decreased coherence properties, depending on α . The qualitative and quantitative agreement of experimental and simulation results presented above show the validity of our model. Furthermore, these results clearly indicate that the linewidth is not dominated by external noise sources, such as fluctuations of the pump current, frequency or amplitude instabilities of the filter drive waveform or acoustic vibrations, since such effects are not contained in the simulation. Our model can now be used to identify the physical effects governing the instantaneous linewidth by successively switching on and off the effects in the simulation, which is not possible in experiment. The central question is if the linewidth is dominated by ASE, as is usually the case for semiconductor and other lasers in the absence of external noise sources [Hen82]. In Fig. 4.3.3(b), the linewidth is displayed as obtained with ASE used only for initial seeding. Comparison with Fig.

4.3.3(a) shows that the power spectrum is virtually unchanged without ASE. Rather, the instantaneous lineshape is governed directly by the FDML dynamics. Thus, the linewidth is an inherent property of the FDML laser caused by the interplay of the various physical effects taking place simultaneously in the laser, such as the sweep filter and gain action, dispersion and self-phase modulation.

4.3.3 Conclusions

In conclusion, the instantaneous power spectrum of an FDML laser is theoretically and experimentally investigated. The linewidth enhancement factor results in a frequency shift relative to the sweep filter center frequency as well as a broadening, and third order dispersion leads to an asymmetry of the instantaneous power spectrum. Good agreement between simulation and measurement is obtained for both the non-detuned and the detuned case, confirming the validity of our theoretical model. The simulations reveal that the instantaneous linewidth is not governed by external noise sources or ASE, but results directly from the FDML dynamics due to the sweep filter and gain action, dispersion and self-phase modulation [Tod11]. Such a theoretical understanding of the effects governing the instantaneous power spectrum is important for a further optimization of the linewidth and thus the coherence properties of FDML lasers. An improvement of the coherence length from the mm range up to cm or even tens of cm would result in the accessibility of new areas for FDML lasers, such as industrial sensing applications or the use of FDML lasers as scanning devices for larger areas.

Chapter 5

Balance of physical effects causing stationary operation of FDML lasers

For this chapter, the experimental setup is the same as in Fig. 4.1.1. However, now the focus lies on what physical effects lead to the formation of a stationary field [Tod11B]. As in the previous chapter, we divide the roundtrip time into subintervals and then Fourier transform the output power in each of these intervals separately, so that we can examine the temporal evolution of the instantaneous power spectrum. The number of the intervals should be sufficiently high to obtain a good temporal resolution. On the other hand, in order to avoid Fourier broadening of the instantaneous power spectra, the subintervals should not be too short. We choose 16 subintervals with a duration of $1.08 \mu\text{s}$ each, so that the effect of Fourier broadening is still negligible.

The finite time-gating of 1.6 ns (full width at half-maximum) in the measurement setup in Fig. 4.1.1 leads to Fourier broadening as well as spectral broadening due to the sweep filter dynamics during the measurement. As discussed above, both effects can be suppressed in the simulation: The time gating is chosen long enough as to avoid Fourier broadening, and the field envelope u in (3.3.4) is described in the swept filter reference frame where the frequency axis moves along with the sweep filter center frequency. However, for direct comparison of the simulated and the experimentally measured spectra, the effects of finite time gating should be considered in the simulation. For the implementation of these effects, the relation between the complex field envelope u in the swept filter reference frame and the untransformed envelope function A has to be used [Jir08],

$$u = A \cdot \exp\left(i \int^t \omega_0(t') dt'\right). \quad (5.0.1)$$

The sweep filter is driven by a cosine function, given by $\omega_0(t) = -\Delta\omega/2\cos(2\pi t/T)$. For a measurement at time t_0 , we can use a Taylor expansion and write the integral in the exponent of (5.0.1) as

$$\int_{t_0}^t \omega_0(t') dt' = \omega_0(t_0)(t - t_0) + \frac{1}{2} \frac{\partial \omega_0}{\partial t} \Big|_{t=t_0} (t - t_0)^2 + \dots; \quad (5.0.2)$$

where the first term induces merely a spectral shift in the Fourier domain and is not further considered, while the second term induces spectral broadening. We therefore obtain for the gated field envelope the relation

$$A = u \cdot \exp \left[-\frac{(t - t_0)^2}{2\sigma^2} - \frac{i}{2} \frac{\partial \omega_0}{\partial t} \Big|_{t=t_0} (t - t_0)^2 \right]; \quad (5.0.3)$$

with the Gaussian pulse duration $\sigma = 1.6\text{ns}/2/\ln(2)^{1/2} = 0.961$ ns. The power spectrum is given by $|A(z, f)|^2$, where $A(z, f)$ denotes the Fourier transform of $A(z, t)$, and the frequency axis is here centered around the sweep filter center frequency at the time t_0 .

An additional effect which has to be considered, is that the experimentally obtained power spectra are averaged over several thousands of roundtrips, thus eliminating fluctuations which arise during the short gating time. In order to take into account this effect, we average the simulated gated spectra over 20 non-subsequent roundtrips, starting from roundtrip 900 to ensure convergence of the simulation. This proves sufficient for eliminating fluctuations. On the other hand, averaging turns out to be unnecessary for the simulated spectra obtained without gating, since there fluctuations are eliminated due to the much longer time intervals over which the spectra are extracted. Furthermore, the optical spectrum analyzer used in the experimental setup shown in Fig. 4.1.1 has a finite resolution of 20 pm, corresponding to a spectral width of 3.5 GHz at 1310 nm. To imitate this effect, the obtained numerical spectra are smoothed over 4000 points.

In Fig. 5.0.1, the simulated instantaneous power spectrum after the SOA at $t=5.3 \mu\text{s}$ is shown for gating and averaging considered (blue dotted curve) and without taking these effects into account (green dotted curve), and compared to the experimental data (dash-dotted curve). The FWHM values are 13.77 GHz, 10.13 GHz and 15.81 GHz, respectively. As can be seen, the consideration of the time gating in the simulation is essential for a precise comparison to experiment. Without the inclusion of these effects, the simulated FWHM linewidth does not match the experimental data very well, as expected.

5.1 Temporal and spatial evolution of the optical cavity field

In Fig. 5.1.1, the simulated temporal evolution of the instantaneous power spectra is shown after the SOA. The spectra change with time, but show an overall shift towards negative frequencies. In this section, we theoretically and experimentally investigate the temporal evolution of the spectral properties, as well as the spatial evolution along the resonator axis. In particular, we investigate how the interplay of the various effects leads to the formation of a steady state light field.

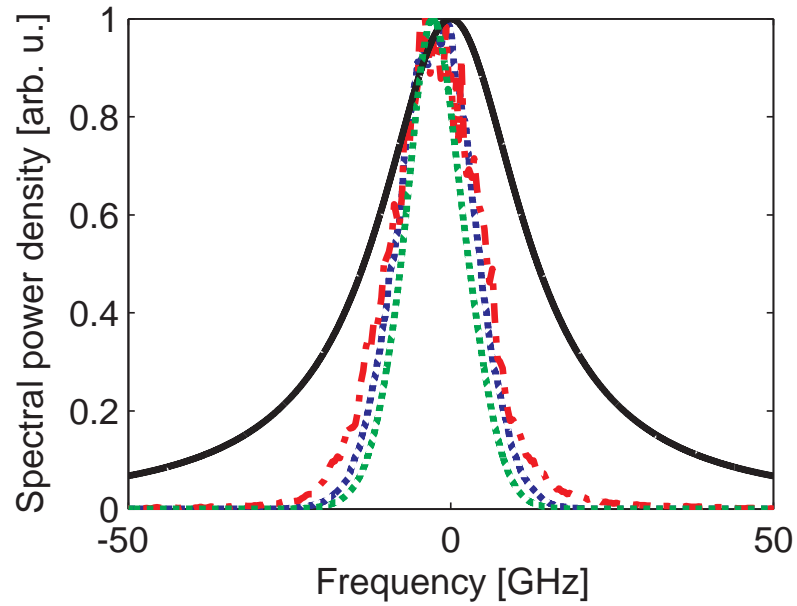


Figure 5.0.1: Instantaneous power spectrum at $t=5.3 \mu\text{s}$ after the SOA for the simulation with gating considered (blue dotted curve), for the simulation without gating (green dotted curve), and as obtained from experiment (dash-dotted curve). The sweep filter transmission (solid curve) is shown for comparison.

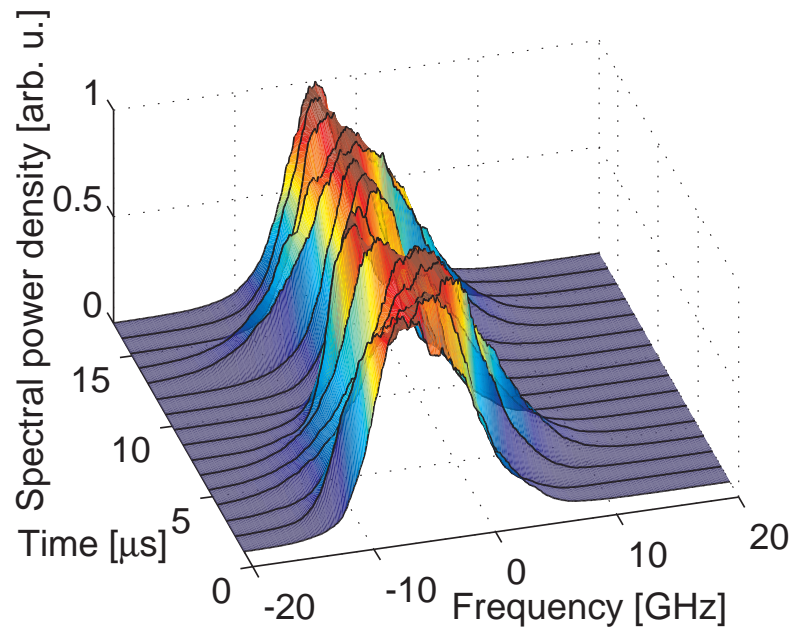


Figure 5.1.1: Simulated temporal evolution of the instantaneous power spectrum after the SOA over a full roundtrip without gating included.

5.1.1 Discussion of the spectral shaping effects

FDML simulations indicate that the temporal and spatial evolution of the laser field, here characterized by its instantaneous power spectrum, is dominated by the gain dynamics including linewidth enhancement, the dispersion and self-phase modulation in the optical fiber, and the sweep filter action [Jir08, Tod11B].

In the following, we investigate how each of these effects contributes to the spectral shaping of the light field. First, we analyze the contribution of the linewidth enhancement factor to the spectral shaping, which has been observed to cause a shift of the power spectral peak to lower frequencies [Tod11B]. This effect is here more closely investigated. We can solve (3.3.4) keeping only the term associated with the optical gain, and obtain

$$u = u_0 \cdot G^{(1-i\alpha)/2} \quad (5.1.1)$$

where the total power gain is related to the gain coefficient by integrating over the length of the gain medium, $G = \exp[2 \int g(\omega_0) dz]$. For the modeling of the gain dynamics, we have to consider both the saturation behavior and the spectral dependence [Tod11B], which is done by using an ansatz

$$G(t) = \frac{G_0[\omega_0(t)]}{1 + P_{av}(t)/P_{sat}[\omega_0(t)]}. \quad (5.1.2)$$

The spectral dependence enters through the frequency dependent peak gain G_0 and saturation power P_{sat} . The saturation is modeled based on a quasi-instantaneous gain saturation approach [Tod11B], accounting for the finite carrier lifetime in the SOA which governs the gain recovery dynamics, assuming a typical value $\tau_c = 380$ ps [Bil06]. In this approach, the saturation level of the gain at a time t is not directly determined from the instantaneous optical power $P(t)$, but rather based on a moving average value, introduced in (3.4.3). In this way, relaxation processes in the gain medium, which lead to a non-instantaneous gain recovery for changes of the optical power on timescales faster than the carrier lifetime, can be adequately taken into account [Tod11B]. Such fast changes can arise due to the complex FDML dynamics itself, and are also induced by ASE and other noise sources. For the simulated optical power shown in Fig. 3.4.3, these high frequency contributions are largely suppressed because of the smoothing applied there, corresponding to a sampling rate of 500 MHz to imitate the experimental measurement setup. However, these contributions give rise to a broadened instantaneous linewidth, as shown in Fig. 5.0.1 We investigate the influence of the linewidth enhancement factor, taking a Gaussian spike $P_0 = u_0^2 = P_g \exp(-t^2/T_g^2)$ where the peak power is set to $P_g = 10P_{sat}$ and T_g is chosen so that the corresponding power spectrum has a full width at half-maximum value of 10 GHz, similarly to the observed instantaneous linewidths [Tod11B].

In Fig.5.1.2(a), the Gaussian spike $P_0(t)$ and the moving average value $P_{av}(t)$ from (3.4.3) for $\tau_c = 380$ ps is shown. As can be seen, the relaxation process induces an asymmetry in form of a slow decay of $P_{av}(t)$. In Fig.

5.1.2(b), the power spectrum of the Gaussian input pulse is shown along with the output power spectrum after the gain medium, obtained with (5.1.1) for $\alpha = 5$. The peak of the output spectrum is shifted by -3.6 GHz.

Further simulations show that the shift is almost exclusively due to the linewidth enhancement, i.e., the imaginary part of the term $(1 - i\alpha)$ in (5.1.1), and not the real part corresponding to the amplification. In other words, the combination of linewidth enhancement and the

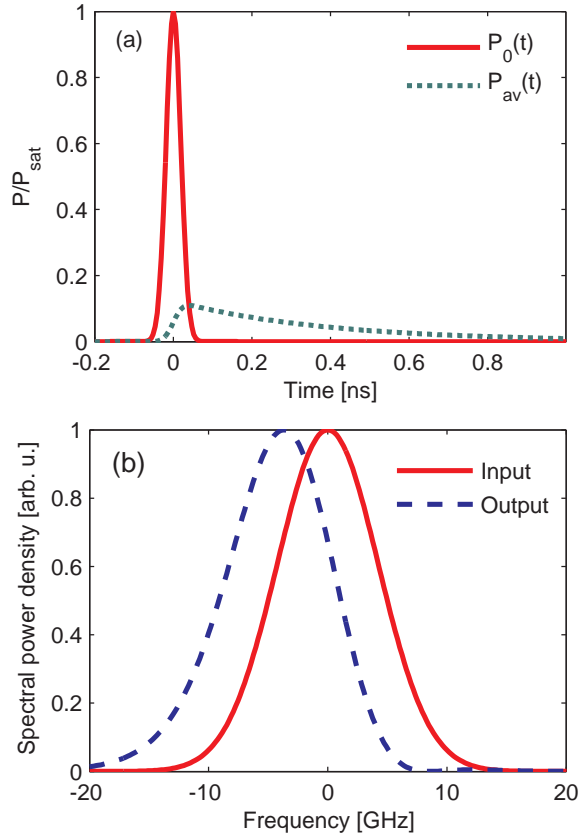


Figure 5.1.2: (a) Gaussian input pulse and the corresponding averaged power as a function of time. (b) Power spectrum of the Gaussian input pulse and output powerspectrum after the gain medium.

recovery dynamics in the gain medium leads to the spectral red shift.

Now we focus on the dispersive effect in the optical fiber. In previous simulations we found that if the sweep rate is detuned with respect to the roundtrip time of the light within the cavity, the third order dispersion D_3 causes a spectral asymmetry, which is however greatly reduced for the non-detuned case considered here [Tod11B]. In the following, we investigate the time dependent influence of dispersion for no detuning. Considering only the relevant terms in (3.3.4), we can obtain a closed analytical solution. For the propagation through a dispersive fiber of length L , the field envelope at the end of the fiber is given by

$$u(z + L) = u(z)\exp\{i [\omega_0^2(t)D_2 + \omega_0^3(t)D_3] L\} = u(z)\exp [i\phi(t)]. \quad (5.1.3)$$

Here we have neglected the term $-iD_2 \frac{\partial^2}{\partial t^2} u$, which by itself does not affect the power spectrum. As described in subsection 3, the instantaneous power spectrum at a time t_0 is obtained by dividing the roundtrip time into subintervals and Fourier transforming the output power in the corresponding interval separately. In the subinterval centered around t_0 , the exponent in (5.1.3) can be approximated by a Taylor expansion,

$$\phi(t) \approx \phi(t_0) + \frac{\partial}{\partial t}\phi(t_0)(t - t_0) + \dots \quad (5.1.4)$$

While the 0th order term $\phi(t_0)$ just represents a constant phase shift, the 1st order term containing $\frac{\partial}{\partial t}\phi(t_0)$, which corresponds to the instantaneous frequency, induces a spectral shift by the amount

$$\delta f = -\frac{\frac{\partial}{\partial t}\phi(t_0)}{2\pi} = -\frac{1}{2\pi} [2D_2\omega_0(t_0) + 3D_3\omega_0^2(t_0)] \frac{\partial}{\partial t}\omega_0(t_0)L \quad (5.1.5)$$

in the Fourier domain. It should be pointed out that dispersion as a linear effect does not change the photon energy, but causes an additional delay of the optical field in the fiber. Due to the sweep dynamics, this re-timing of the optical field leads to an additional spectral shift of the instantaneous power spectrum with respect to the sweep filter center frequency, as described by (5.1.5). In Fig. 5.1.3, the spectral shift according to (5.1.5) as a function of t_0 is shown for a single propagation through the optical fiber with $D_2 = -276 \text{ fs}^2/\text{m}$, $D_3 = 12183 \text{ fs}^3/\text{m}$, and $L = 3400 \text{ m}$. Since the center wavelength in our simulation is 1320 nm, which is close to the zero dispersion point $D_2 = 0$, the influence of D_3 is dominant.

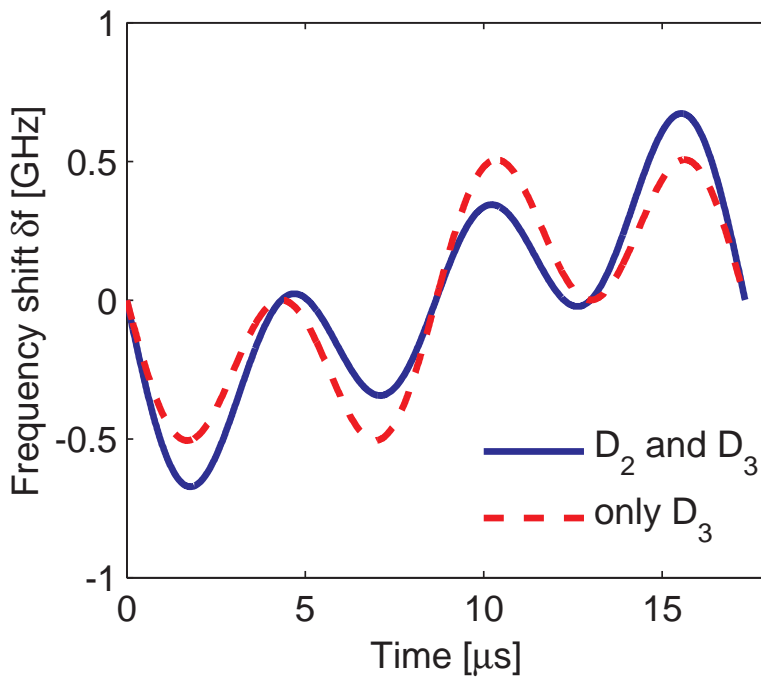


Figure 5.1.3: Temporal dependence of the frequency shift caused by the fiber dispersion.

The self-phase modulation in the optical fiber is well known to induce spectral broadening [Agr06]. For a very slowly varying output power level, as in the ideal FDML laser, this effect might be negligible. However, in real operation, the optical power exhibits high frequency fluctuations as discussed above. As a consequence, self-phase modulation has a considerable influence on the instantaneous power spectrum.

In the following, we investigate this effect, using a Gaussian spike as a model for optical power fluctuations. Considering only the relevant term in (3.3.4), we obtain the solution

$$u(z + L) = u(z)\exp(i\gamma|u(z)|^2L). \quad (5.1.6)$$

The effect of the self-phase modulation is illustrated in Fig. 5.1.4 for $\gamma = 0.00136$ W/m and again a fiber length of $L=3400$ m, assuming the same Gaussian input pulse as in Fig. 5.1.2, here with a peak power of 200 mW. While self-phase modulation does not induce a frequency shift, it causes spectral broadening.

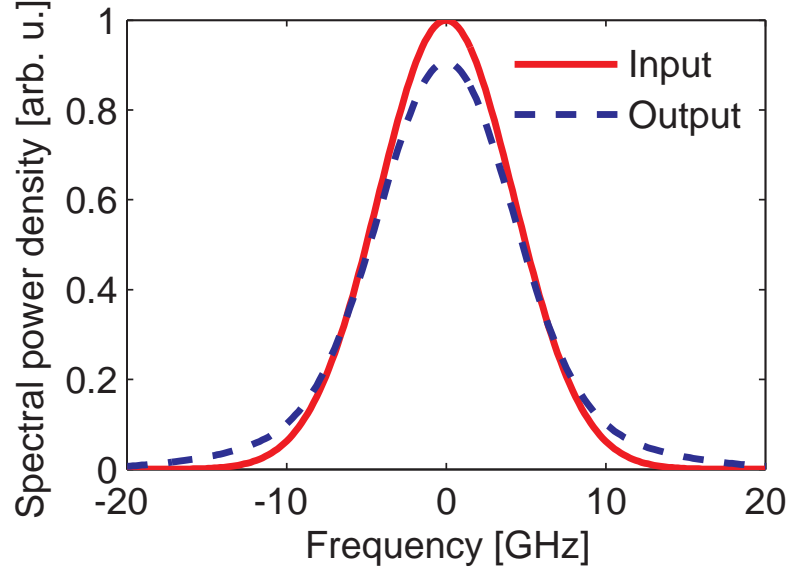


Figure 5.1.4: Power spectrum of the Gaussian input pulse and output power spectrum after self-phase modulation.

Next we investigate the effect of the sweep filter, which, as we will show in the following, acts as a bandpass filter and balances the frequency shift induced by the dispersion and the linewidth enhancement. We solve (3.3.4) in frequency domain keeping only the term associated with the sweep filter and using $\omega = 2\pi f$, and obtain the pulse envelope in Fourier domain

$$U(\omega) = t_s(\omega)U_0(\omega). \quad (5.1.7)$$

The sweep filter is modeled as a lumped optical element, where the transmission characteristic is related to the sweep filter coefficient by integrating over the length of the sweep filter [Tod11B], with

$$t_s(\omega) = \exp\left[-\int a_s(\omega)dz\right] = \frac{T_{max}^{1/2}}{1 - 2i/\Delta}. \quad (5.1.8)$$

Here, we choose $\Delta = 0.169$ ps⁻¹, corresponding to a Lorentzian filter with an FWHM bandwidth of 0.156 nm. The effect of the sweep filter is illustrated in Fig. 5.1.5 for the same Gaussian input pulse as in Fig. 5.1.2, but shifted by -10 GHz relative to the sweep filter center frequency. The low frequency wing of the

spectrum is "cut off" by the sweep filter, which induces an effective shift of the output spectrum towards higher frequencies. Similarly, spectra centered around positive frequencies are effectively shifted to lower frequencies, thus reducing the spectral shift. Furthermore, the sweep filter acts as a bandpass, narrowing the linewidth of the instantaneous power spectrum.

Due to its complex transmission characteristic (see (5.1.8)), the filter induces not only absorption, but also a frequency dependent phase offset $\phi = \arctan(2\omega/\Delta)$. Approximating the phase by a first order Taylor series expansion in analogy to (5.1.4), $U(\omega)$ in (5.1.7) acquires an additional linear phase, which corresponds to a delay of the optical field in time domain. Due to the sweep dynamics, this re-timing of the optical field is associated with an additional spectral shift. However, for the sweep filter parameters of the investigated laser, this time delay amounts to only 10 ps at the center and even less in the wings of the filter, corresponding to a maximum frequency shift of 30 MHz, which is much smaller than the effective shift caused by the sweep filter absorption. We have confirmed this by comparing simulations with and without considering the phase in (5.1.8), yielding very similar results and thus showing the negligible influence of these phase contributions.

The resulting instantaneous power spectra in steady state operation are thus determined by a balance between the frequency shift induced by dispersion and linewidth enhancement on the one hand, and the compensating effect of the sweep filter on the other hand.

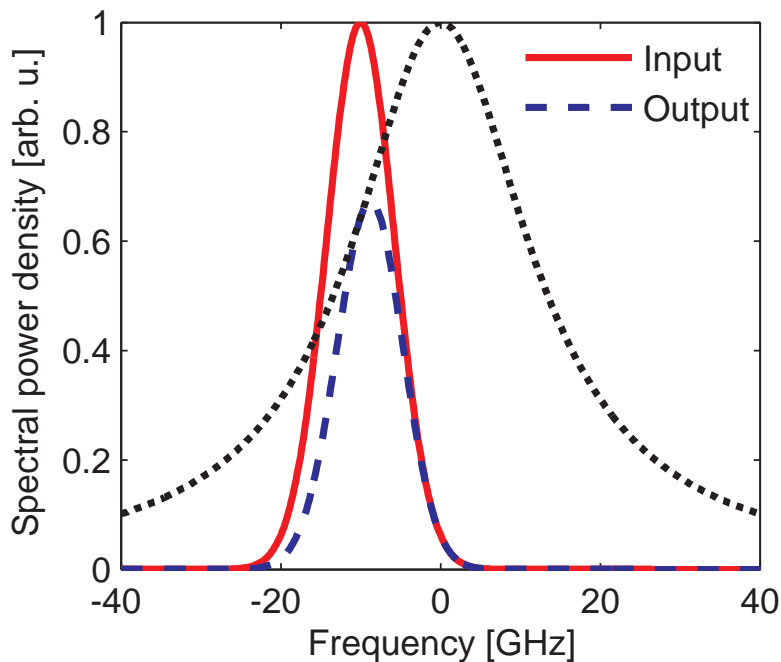


Figure 5.1.5: Power spectrum of the Gaussian input pulse and output power spectrum after the sweep filter. The sweep filter transmission (dotted curve) is shown for comparison.

5.1.2 Analysis of the FDML dynamics in steady state operation

In order to better understand the interplay of the various optical cavity elements leading to the formation of a steady state light field, the temporal evolution of the instantaneous power spectrum at various points in the cavity is monitored. The simulation results are shown in Fig. 5.1.6 for the mean frequency and full width at half-maximum (FWHM) linewidth, extracted from the obtained spectra without gating. In Fig. 5.1.6(a), the temporal evolution of the mean frequency, extracted from the obtained power spectra, is shown after the SOA, the fiber and the sweep filter. By comparing the results after the sweep filter and the SOA, it can be seen that the SOA causes a negative frequency shift at all times. This is due to the linewidth enhancement, as shown in Fig. 5.1.2. The fiber dispersion induces a negative frequency shift during the forward sweep, and a positive shift during the backward sweep, as illustrated in Fig. 5.1.3. However, the linewidth enhancement dominates, leading to negative mean frequency values at all times. Finally, the sweep filter partly compensates this negative shift, stabilizing the operation and leading to the formation of a steady state. In Fig. 5.1.6(b), the temporal evolution of the FWHM linewidth is shown, as obtained for a single roundtrip. The sweep filter acts as a bandpass (see Fig. 5.1.5), thus narrowing the linewidth and compensating for the broadening induced by the SOA and the fiber. The linewidth maxima coincide with the power maxima (see Fig. 3.4.3). The reason is that the phase offset due to self-phase modulation, and thus the resulting spectral broadening, depends on the optical power, see (5.1.6). The investigated setup operates at around 1320 nm close to the zero dispersion point $D_2=0$. For lasers operating at different wavelengths, the second order dispersion can play a major role. To investigate this effect, simulations have been performed using the value of D_2 at 1550 nm (anomalous dispersion regime) and at 1060 nm (normal dispersion regime). In both cases the overall linewidth increases significantly, and also the linewidth change during a roundtrip is more pronounced. For the D_2 at 1550 nm, the instantaneous linewidth varies between 7.10 and 27.15 GHz, and similar values are obtained for the D_2 corresponding to 1060 nm.

5.1.3 Comparison to experiment

In order to verify the validity of our simulation approach, we compare the numerical results to the experimental data. To enable a quantitative comparison, we include in our simulations the experimental effects of time gating, averaging and limited measurement resolution as in Section 4.1. First, we extract the full width at half-maximum (FWHM) linewidth of the simulated and experimental spectra as a function of time. In Fig. 5.1.7, the theoretical and experimental linewidth is plotted versus time. The experimental data indicates an asymmetry of the linewidth evolution for the forward and the backward sweep, with maxima obtained at around 4.3 μs and 13.7 μs , the positions where the sweep filter speed is maximum. This trend is also confirmed for the simulations with gating included, which yield reasonable qualitative and quantitative agreement with the experiment. The simulation data without gating reveal a much smaller linewidth dependence, demonstrating that the observed maxima are mainly due to the

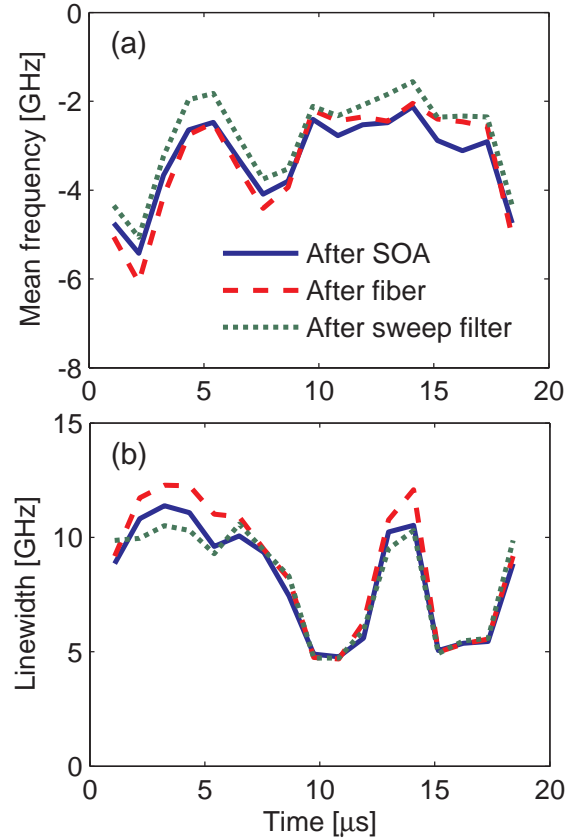


Figure 5.1.6: Simulation results for the temporal evolution of (a) mean frequency and (b) linewidth.

fast sweep filter dynamics at these positions, leading to a maximum broadening effect during the finite time gating.

In the following, we compare the instantaneous power at various positions in the laser cavity. The time is fixed to $t = 5.3 \mu\text{s}$. In Fig. 5.1.8, the experimental (dashed curve) and theoretical (dotted curve) spectral power density is plotted after the SOA, the fiber and the sweep filter, respectively. Since the instantaneous power spectrum is measured on an absolute frequency scale and the time dependent sweep filter center frequency at the measurement time is not known with sufficient accuracy, it is not possible to determine the frequency shift of the experimental power spectra. Thus, the frequency axis of the experimental spectra is chosen so that the experimental and simulated peak positions coincide. In Fig. 5.1.8(a), the FWHM spectral width after the SOA is 15.81 GHz for the experimental spectrum and 13.77 GHz for the simulated spectrum, respectively. The mean frequency of the simulated spectrum is located at -2.28 GHz with respect to the sweep filter reference frame. In Fig. 5.1.8(b), the spectral power density is plotted after the SMF. The FWHM is 13.82 GHz for the experimental data, and 13.83 GHz for the simulation, respectively. The simulated mean frequency shift is -2.39 GHz. Fig. 5.1.8(c) shows the instantaneous power spectra after the sweep filter. Now the FWHM is 12.68 and 13.19 GHz for the experimental and theoretical data, respectively, while the simulated mean frequency shift is -1.71 GHz.

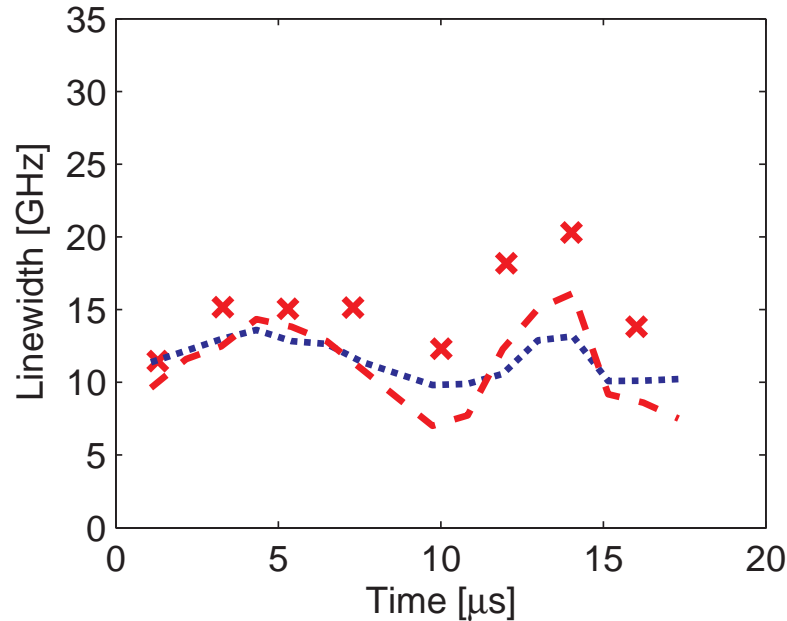


Figure 5.1.7: Simulated and measured temporal evolution of the linewidth. Shown are simulation results with gating considered (dashed curve) and without gating (dotted curve), as well as experimental data (crosses).

Altogether, the results displayed in Fig. 5.1.7 and Fig. 5.1.8 show good qualitative and quantitative agreement between the simulation and experiment, confirming the validity of the chosen simulation approach. The inclusion of optical gating, averaging over several roundtrips and limited measurement resolution in the simulation enables us to evaluate the additional linewidth broadening caused by these effects, thus allowing for a closer comparison with experiment, and an assessment of the influence of these effects on the experimental data. Remaining deviations between theoretical and experimental results are mainly ascribed to uncertainties in some of the used laser parameters. For example, the relaxation time and linewidth enhancement factor of the SOA may deviate somewhat from the assumed typical values. Furthermore, the spectral features depend strongly on the detuning of the sweep filter with respect to the cavity roundtrip time [Tod11B]. While the zero detuning point can be exactly fixed in the simulation, it can only be approximately determined in the experiment based on criteria such as the maximum obtained output power.

5.2 Conclusion

In conclusion, the chapter provides an answer to the question, why FDML lasers operate in a stationary regime. A quantitative analysis is given about which effects balance each other, leading to a stable spectrum and output power: (1) A red shift of the instantaneous power spectrum towards lower frequencies is caused by the linewidth enhancement of the SOA in combination with the gain recovery dynamics. Also the dispersion induces a time dependent spectral shift. These effects are counterbalanced by the

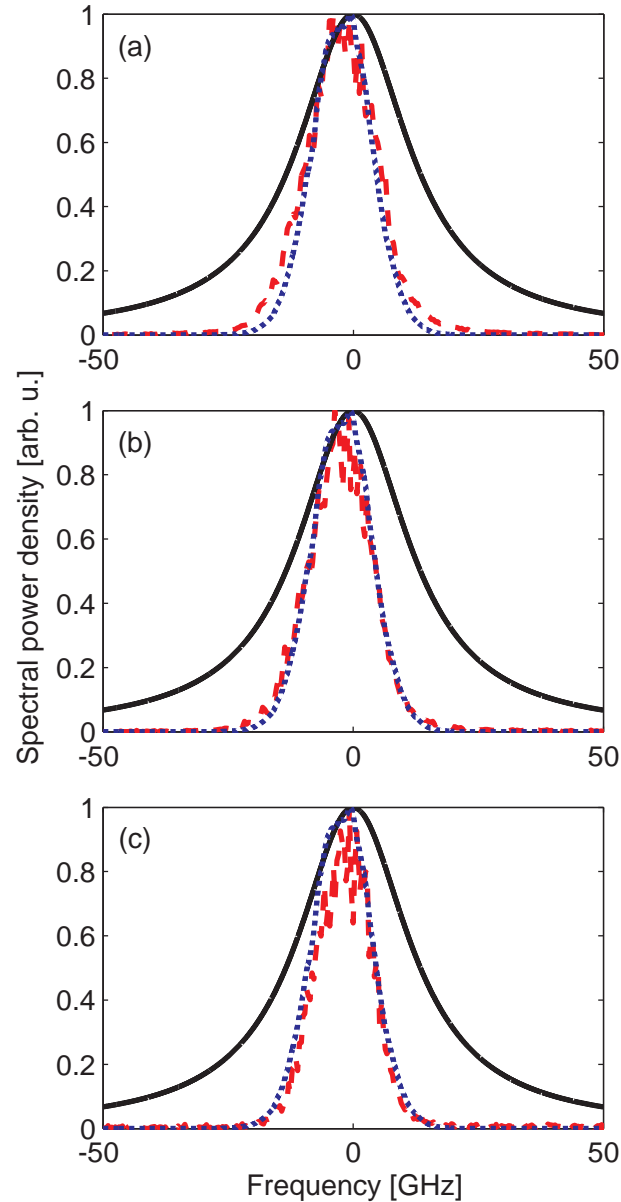


Figure 5.1.8: Experimental (dashed) and theoretical (dotted) instantaneous power spectra after (a) the SOA, (b) the SMF and (c) the sweep filter at $t=5.3 \mu\text{s}$.

asymmetric absorption of the tunable spectral bandpass filter. For a red-shifted spectrum, the sweep filter transmission function causes an effective shift to higher frequencies by reducing the low-frequency spectral wing. (2) Self phase modulation in the long fiber delay line causes a spectral broadening, and also the linewidth enhancement and dispersion influence the instantaneous power spectrum. The broadening is counterbalanced by the bandpass filter, narrowing the spectrum again by the repetitive filtering event at each roundtrip.

For these investigations, a detailed analysis of the optical field propagation in the FDML laser is presented. The temporal evolution of characteristic spectral parameters at various positions in the cavity,

such as the frequency shift and the linewidth, is investigated, yielding the described insight into the formation of a steady state light field. All relevant physical effects are considered in our model. A comparison of numerical results to experimental data shows good agreement, validating the theoretical model. These new insights represent an important step towards understanding the fundamental mechanisms governing the steady state dynamics in the FDML regime, and are helpful towards a further optimization of the FDML laser.

Chapter 6

Pulse compression in an FDML laser

6.1 Types of ultrashort pulsed lasers

As has been shown in the previous chapters, the FDML laser has a cw power output. This means that the power does not fluctuate too much over the course of time. The power output can of course have a time-dependency, however the power does not fall to zero, so that separate pulses would evolve. This is the case for a pulsed laser. Laser pulsing can be achieved in several ways. One way is Q-switching, which has first been proposed in 1958 [Tay00], with first experimental realisations in the early 1960s [Clu62]. Here, ultrashort pulses are achieved via the integration of an attenuator into the laser resonator, which suppresses lasing so that inversion can build up. In active Q-switching, the attenuator is externally controlled. The pulse duration is therefore controlled externally. In passive Q-switching, a saturable absorber is inserted into the laser cavity. By varying the pump power, the repetition rate of the pulses can be controlled, and also by the amount of saturable absorber in the cavity. Another way is mode-locking. Here, the phase relationship between the distinct laser modes is fixed in such a way, that the power output is pulsed [Lam64][Kui70]. This can be achieved by active or passive mode-locking techniques [Har64][Moc65], where by a modulation of the amplitude of the light-field, the phase relation between the different modes gets fixed, or locked.

In active mode-locking for example, an acousto-optic modulator is placed into the laser cavity. This device can be driven with an electrical signal, which in turn modulates the light field in the cavity sinusoidally. The modes in the cavity have a frequency-spacing $\Delta\nu$. Now the modulator is driven in such a way, that the driver frequency exactly matches $\Delta\nu$. The amplitude modulation itself causes sidebands at frequencies which have the same spacing. If this process is now applied for a long enough time-span, all the modes will be phase-locked at some point in time.

In passive mode-locking, a saturable absorber is placed into the cavity in order to block out low intensity light. High intensity light is preferably transmitted. Because of random intensity oscillations, this process repeats, and the high intensity light is amplified selectively, whereas the low-intensity light

is absorbed. After a long enough time-span this then leads again to a pulse-train with a fixed frequency spacing $\Delta\nu$.

For both cases, a fixed phase relation in the frequency domain then leads to distinct, separate pulses in the time-domain. These pulses can get very short, with shortest pulses in the atto-second range [Ant96], and commercial applications with femtosecond lasers are already emerging. Femtosecond lasers can be divided into different types, the first one being bulk lasers. This type of laser is passively mode-locked with pulse lengths typically in the range of 30 fs to 30 ps. Typical output powers lie between 100 mW and 1 W and repetition rates of 50 to 500 MHz. The most prominent lasers in this category are titanium-sapphire lasers [Mou86][Gib96][Sut99], which have achieved pulse durations of below 10 fs [Sti95], with the lowest achieved pulse length of 5 fs [Ell01][Nog08].

Another type of laser for short pulse durations are fiber lasers [Koe64], which are mostly passively mode-locked. They have pulse durations of 50 to 500 fs and repetition rates of 10 to 100 MHz [Bur73][Sto74][Mea85].

Dye lasers are another example of mode-locked lasers, which are however not so common since they pose high technical disadvantages in comparison to bulk lasers. They are capable of producing pulses below 1 ps length, with shortest pulses of ≈ 20 fs length [Val85][Sha74][Sha75]. Recently, continuous wave operation of a dye laser has been achieved [Bor06].

Semiconductor lasers can generate very short pulses by means of active mode-locking, below 500 fs [Gar02], but have very high repetition rates of above 1 THz [Ara96]. This makes them suitable for applications in optical fiber communication for very fast data transmission.

6.2 Ideal pulse compression

In an FDML laser, the fixed phase relationship between the different intracavity modes is achieved directly in the frequency domain by the use of the sweep filter as described in chapter 2 in detail. The output of the FDML laser is cw, and in order to operate the laser in pulsed mode, dispersion compensation is a crucial element to achieve this. In order to generate very short pulses, the phase of the complex field envelope $u(z, \omega)$ has to be cancelled out almost completely in the frequency domain, so that the resulting field in the time domain is very short. A regular Gaussian pulse in the time domain can be written as:

$$u(t) = u_0 e^{-\frac{t^2}{2\sigma_T^2}}. \quad (6.2.1)$$

Via Fourier transform, the envelope in the frequency domain has the following relation:

$$\tilde{u}(\omega) = \mathcal{F}[u(t)] = u_0 \int_{-\infty}^{\infty} e^{-\frac{t^2}{2\sigma_T^2}} e^{i\omega t} dt = u_0 \sqrt{2\pi\sigma_T^2} e^{-\frac{\omega^2\sigma_T^2}{2}}. \quad (6.2.2)$$

In comparison, a frequency chirped Gaussian of the form

$$u_{ch}(\omega) = u_0 e^{\frac{-\omega^2 \sigma_T^2}{2} - iD\omega^2}, \quad (6.2.3)$$

with a quadratic dispersion relation leads to a wider pulse in the time domain:

$$u_{ch}(t) = \mathcal{F}^{-1}[u_{ch}(\omega)] = u_0 \sqrt{\frac{1}{\sigma_T^2 + 2iD}} \exp\left[\frac{-t^2}{2(\sigma_T^2 + 2iD)}\right]. \quad (6.2.4)$$

The power spectrum $P_{ch}(t)$ is then given by

$$P_{ch}(t) = \frac{|u_0|^2}{\sqrt{\sigma_T^4 + 4D^2}} \exp\left(-\frac{t^2}{\sigma_T^2 + 4D^2/\sigma_T^2}\right) = |u_0|^2 e^{\frac{-t^2}{2\sigma_{T,ch}^2}}. \quad (6.2.5)$$

It follows that for $D \neq 0$, $\sigma_{T,ch} > \sigma_T$. This means that the additional dispersive phase in the frequency domain leads to a longer pulse in the time domain.

In order to compensate the effect of the frequency chirp, the pulse from (6.2.3) can now be led through a dispersive medium so that the effect of the phase is cancelled out (ideal compression):

$$u_{comp}(\omega) = u_0 e^{\frac{-\omega^2 \sigma_T^2}{2} - iD\omega^2} e^{iD\omega^2} = u_0 e^{\frac{-\omega^2 \sigma_T^2}{2}}, \quad (6.2.6)$$

which yields the shorter pulse in the time domain. This form of ideal compression is of course not achievable under real circumstances, because the phase is not entirely smooth, but has a fine structure. Therefore a compensation of the phase can never cancel out the complete phase. The shortest achievable pulse in the time domain is always limited by the time-bandwidth product of the system. For a Gaussian shaped pulse, the following relation suffices:

$$t_{limit} \cdot \Delta f \approx 0.44. \quad (6.2.7)$$

In our case, $\Delta f = 18$ THz which yields in the Fourier limit a pulse length of $t_{limit} = 24.4$ fs. This can be checked by computing the expression (6.3.5), and extracting the phase angle using Matlab. The unwrap routine can compute the correct phase angle, which then can be subtracted. Then, we Fourier backtransform into the time domain and get the compressed pulse.

6.3 Analytical treatment of pulse compression for the example of a linear ramp

We now investigate the compression of a linear ramp. The sweep filter drive function $\omega_0(t)$ is now given by

$$\omega_0(t) = \frac{\Delta\omega}{T}t, \quad (6.3.1)$$

with the sweep range $\Delta\omega$ and the roundtrip time T . According to (3.3.2), the envelope in the laboratory is given by

$$A(z, t) = u(z, t) \exp\left(-i \int^t \omega_0(t') dt'\right). \quad (6.3.2)$$

For this example we set $u(z, t) = 1$, because we are only interested in the mathematical properties of the phase, which are relevant for pulse compression and assume a time-constant amplitude A for an "ideal" FDML field. Further, we are not interested in the spatial dependency of the envelope, so that we can write:

$$A(t) = \exp\left(-i \int^t \omega_0(t') dt'\right) = e^{-i \frac{\Delta\omega}{2T} t^2}. \quad (6.3.3)$$

We now want to calculate the Fourier transform of a single sweep

$$A(t)_{single} = [\Theta(t + T/2) - \Theta(t - T/2)] e^{-i \frac{\Delta\omega}{2T} t^2}, \quad (6.3.4)$$

where $\Theta(t)$ denotes the Heavyside step-function.

$$\begin{aligned} \tilde{A}(\omega)_{single} &= \mathcal{F}[A(t)_{single}] = \int_{-\infty}^{\infty} [\Theta(t + T/2) - \Theta(t - T/2)] e^{-i \frac{\Delta\omega}{2T} t^2} e^{i\omega t} dt = \\ &= \int_{-T/2}^{T/2} e^{-i \frac{\Delta\omega}{2T} t^2} e^{i\omega t} dt = \\ &= \sqrt{\frac{\pi T}{2\Delta\omega}} e^{i \frac{T\omega^2}{2\Delta\omega}} \left[\operatorname{erfi}\left(\frac{(\frac{1}{2} - \frac{i}{2})(\Delta\omega t - T\omega)}{\sqrt{\Delta\omega T}}\right) \right]_{-T/2}^{T/2}, \end{aligned} \quad (6.3.5)$$

with the imaginary error function $\operatorname{erfi}(z) = -i \cdot \operatorname{erf}(iz)$, $z \in \mathbb{C}$. For the numerical evaluation of (6.3.5), we need to make use of the asymptotic expansion of the error function for large values of $\mathcal{R}(z)$ and $\mathcal{I}(z)$. In our example, with the laser setup explained in Chapter 3.2 and 4.1, we have values of $\Delta\omega = 1.135 \cdot 10^{14} \text{ s}^{-1}$, $T = 17.32 \text{ } \mu\text{s}$, and $\omega \in [1.373 \cdot 10^{15}; 1.487 \cdot 10^{15}] \text{ s}^{-1}$. For $\omega = 1320 \text{ s}^{-1}$, at the center frequency which is also the steepest point of the sweep curve, we have values in the order of 10^5 for $\mathcal{R}(z)$ and $\mathcal{I}(z)$, respectively. Therefore we need an asymptotic expansion for (6.3.5).

The envelope of the single sweep in the frequency domain $\tilde{u}(\omega)_{single}$ is a complex field, that can be written in the form

$$\tilde{u}(\omega)_{single} = |\tilde{u}(\omega)_{single}| e^{i\Phi(\omega)}. \quad (6.3.6)$$

In order to compress the pulse in the time domain, we have to cancel out the phase $\Phi(\omega)i$ as was shown in the previous example with the chirped Gaussian. A constant phase factor does not change the width of the pulse in the time domain, therefore a constant phase is analogous to the case of zero phase. This form of ideal compression is not achievable under real circumstances, but only shows the maximal achievable limit of compression. The resulting field where the phase is subtracted, is then Fourier transformed back into the time domain, where we then get the compressed pulse.

The compressed pulse in the time domain is then given by

$$u(t)_{comp} = \frac{T}{2\pi} \int_{-\infty}^{\infty} |\tilde{u}(\omega)_{single}| e^{i \cdot const} e^{-i\omega t} d\omega. \quad (6.3.7)$$

We can now plot the intensity of the complex field $u(t)_{comp}$, which is given by the absolute square $|u(t)_{comp}|^2$. The intensity of the ideally compressed pulse is shown in Fig. 6.3.1. A pulse length of 49 fs can be extracted, which is about twice the pulse length for the estimate of a Gaussian in the previous example. However, even though the pulse shape for the linear ramp differs from a Gaussian, it suffices as a rough estimate.

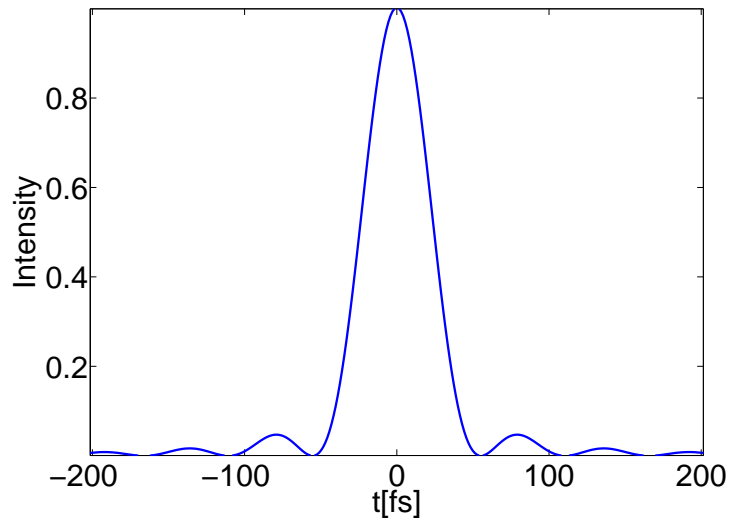


Figure 6.3.1: Fourier limited pulse compression in an FDML laser for the example of a linear ramp. The extracted FWHM pulse length is 49 fs, for the laser parameters of the laser setup explained in chapter 2.2.

6.4 Experimental setup for pulse compression

The experimental setup for pulse compression is in its structure similar to Fig. 3.2.1 or Fig. 4.1.1, in that the same mechanisms apply for the working of the FDML laser itself. The laser setup for the pulse compression is shown in Fig. 6.4.1(a). This laser operates at a center wavelength of 1560 nm, with a tuning range of 211 nm [Eig11B]. The sweep frequency is also much higher with 390 kHz. This is accomplished by using a much shorter delay fiber, which comprises of 246 meters of single mode fiber

(Corning SMF 28), as in the previous setup, but additionally 16 meters of dispersion compensation fiber (DCF, Corning HFDK). The reason for the additional DCF fiber is to reduce the remaining dispersion in the delay line to almost zero in order to improve the coherence properties of the laser. We have a sigma-ring configuration [Jir08B], where the optical circulator (CIR) passes the light along to the delay fiber. The light is then reflected at the Faraday rotation mirror (FRM), and it passes the CIR again, so that the delay length is passed twice, resulting in a total delay length of 524 m. The total time $T_R = 2.56 \mu\text{s}$ which the light needs to pass the delay length results in a sweep frequency of $f_s = 390 \text{ kHz}$. The optical isolators (ISO) ensure unidirectional lasing by cancelling out unwanted reflections. The polarization controllers (PC) enable the adjustment of the polarization in the fiber.

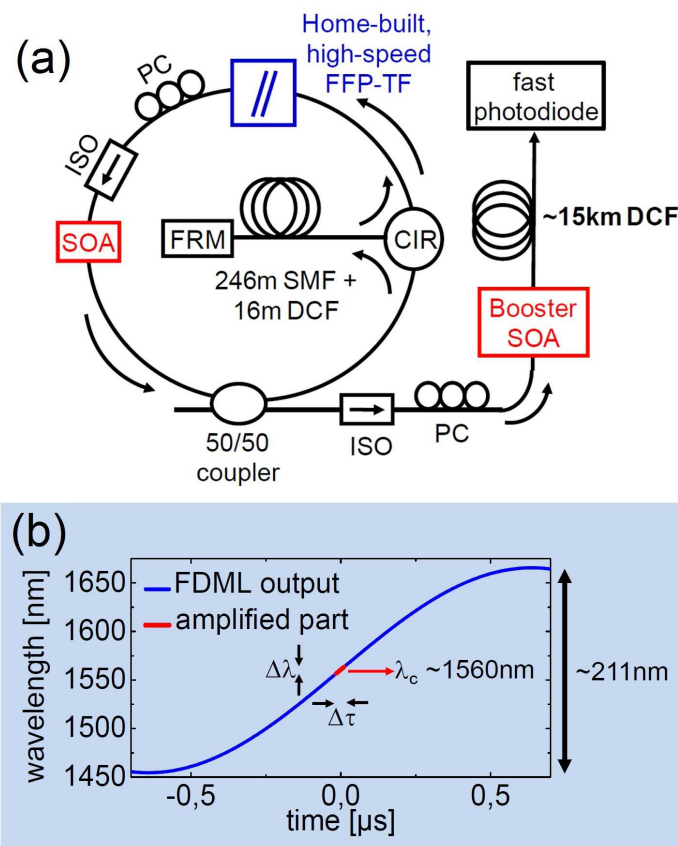


Figure 6.4.1: (a) The FDML laser setup operated at 1560 nm center wavelength and a sweep frequency of 390 kHz. The post-amplification devices are used to amplify the output signal. The dispersion compensation fiber (DCF) is used for temporal compression and the detection system detects the short pulses. The SOA denotes the semiconductor optical amplifier, ISO denotes the optical isolator, PC is the polarization controller, FRM is the Faraday rotation mirror, CIR denotes the optical circulator and FFP-TF denotes the fast Fabry-Perot tunable filter, built by Robert Hubers group at LMU München. (b) Typical wavelength over time characteristics of the FDML output, including the part used for temporal compression.

The SOA in the sigma-ring is polarization independent as in the previous setup and has the gain maximum at $\approx 1550 \text{ nm}$. The last element in the sigma-ring is the sweep filter, where a very fast sweep filter (FFP-TF) is used, self-built by the group of Robert Huber at LMU München [Eig11B]. This type of sweep

filter offers a very high sweep of $250 \text{ nm}/\mu\text{s}$ needed for these high repetition rates. 50% of the light from the sigma-ring is outcoupled, and the laser light is passing along to another ISO and PC as in the sigma-ring. Then the laser output arrives at the booster SOA, which serves as a switch for the laser output. This means that it only amplifies and transmits a fraction of each forward sweep, in order to determine the bandwidth $\Delta\lambda$, the temporal width $\Delta\tau$ and the center wavelength $\lambda_c = 1560 \text{ nm}$, which is then used for the temporal compression. We here have $\Delta\lambda = 6 \text{ nm}$ and $\Delta\tau = 24 \text{ ns}$. The booster SOA is voltage controlled by a fast current modulator, which in turn is fed by the voltage control. The voltage control is also driving the sweep filter, so that the booster SOA is linked to the wavelength-position of the sweep filter, which then enables the SOA to amplify and transmit the exact same location in the forward sweep as intended. In contrast to the SOA in the sigma-ring, the booster SOA is polarization dependent, so that the polarization of the light changes the amplification. ISOs are positioned all along the way in order to focus the laser beam even more. The temporal compression itself is then achieved in the 15 km long DCF fiber positioned after the booster SOA. In the last step, the pulses are then analyzed with an analog sampling oscilloscope or with an intensity autocorrelator, reading the signals of the fast photodiode. In Fig. 6.4.1(b), the wavelength-time characteristics of a laser output is shown for a center wavelength of 1560 nm and passing the DCF spool on time (1x). It can be seen that the amplified part is a very small fraction of the total forward sweep. The compression itself takes place by the use of the DCF fiber. As explained in the previous section, the dispersion slope of the DCF fiber is used to compensate the phase of the FDML optical field. A compensation of the phase in the frequency domain results in a significantly shorter pulse in the time domain. Theoretically, the achievable limit is given by the time-bandwidth product, and is below 100 fs for this setup. However, technical limitations inhibit reaching this limit. For one thing, the voltage feed-back system that couples the SOA boost with the sweep filter is not 100% accurate. An active FDML frequency feed-back stabilization could overcome this limitation. Another limiting factor is the sweep filter performance. An even faster responding sweep filter with a narrower transmission window would also result in a greatly reduced pulse length. Lastly, the remaining dispersion in the resonator also lengthens the pulse. Thus, an even better dispersion compensation would also reduce the pulse length again. In Section 6.5, different methods are discussed that could overcome those limitations, resulting in a pulse length that would reach the time-bandwidth limit [Eig11B]. An FDML laser with such a performance might open up whole new fields of applications.

6.5 Simulation of pulse compression and comparison to the experiment

6.5.1 Simulation

The simulation is technically identical to the simulation described in Chapter 3.4.1 and 3.4.2. However, we have here included the laser parameters from this setup, meaning that we have a different tuning range, center frequency and also different dispersion slopes and gain characteristics. The SOA gain characteristics have again been measured experimentally, as in Chapter 3.4.2. Also, the dispersion has been measured experimentally and implemented into the code. Because we now have a delay line consisting of 246 m of SMF fiber and 16 m of DCF fiber, we have different dispersion values. Because of the dispersion compensation, the values for D_2 and D_3 are much lower than in the previous simulations, at values of $D_2 = -3.0835 \cdot 10^{-28} \text{ s}^2/\text{m}$, $D_3 = 5.7187 \cdot 10^{-42} \text{ s}^3/\text{m}$. We also take the fourth order dispersion into account, making the simulation more precise. We have a fourth order dispersion coefficient of $D_4 = -1.3731 \cdot 10^{-55} \text{ s}^4/\text{m}$. The tuning range is now 211 nm, and the center wavelength is at 1560 nm. Another important factor in this experimental setup, is that although in the sigma-ring, the setup is polarization independent, the booster SOA is polarization dependent. This is neglected in the simulation, because the simulation is for the sigma-ring, and the compression afterwards is done separately. However, it is possible that the polarization dependence of the compression setup after the sigma-ring, could have an effect on the pulses in the experiment, which are not accounted for in the simulation. However, as will be seen, the results from the simulation indicate that this effect is small, because they match the experimental data very well.

As in the previous simulation code, we save the resulting complex FFTW field into files, which are then read using Matlab. In the next subsection, it is explained how the mechanism of emulating the pulse compression in the experiment, is achieved for our simulation.

6.5.2 Compression routine and emulation of the experiment

The emulation of the compression is done using Matlab. The complex FFTW field $u[0]$ and $u[1]$ is read into Matlab from the data files from the simulation itself. They contain the complex FFTW field in the time domain for the experimental setup of Fig. 6.4.1 for the sigma-ring, thus without compensation. The compensation itself is now performed in Matlab.

6.5.2.1 Transformation to the laboratory frame

As stated, the complex FFTW field $u[0]$ and $u[1]$, is the output of the simulation for the field $u(z, t)$, which is the field in the swept-filter reference frame. In the experimental setup however, the field $A(z, t)$ in the laboratory frame is used for the compression. We therefore have to backtransform the field $u(z, t)$

into the laboratory frame, using the relation (6.5.1), so that we have for $A(z, t)$:

$$A(z, t) = u(z, t) \exp \left(-i \int^t \omega_0(t') dt' \right); \quad (6.5.1)$$

with $\omega_0(t) = -\frac{\Delta\omega}{2} \cos(2\pi/T \cdot t)$. This is also implemented into the Matlab code accordingly.

6.5.2.2 Emulation of the analog sampling oscilloscope

The complex field is averaged over 20 roundtrips, in order to simulate the effect that the analog sampling oscilloscope has in the experiment. Here, the output is not displayed for single roundtrips, but is instead averaged over many roundtrips. Therefore we simulate this effect by averaging over 20 roundtrips. A higher number of roundtrips would result in too large data files, given that one roundtrip data file already contains 238 MB, so that an averaged FFTW field output has more than 4 GB of data.

6.5.2.3 Emulation of the fine-tuning of the tuning range

Another effect that can easily be done in the experiment, is changing the tuning range of 211 nm, which corresponds to $\Delta\omega_0 = 1.6343 \cdot 10^{14} \text{s}^{-1}$. When viewing the compressed pulse on the sampling oscilloscope, in the experiment the optimal point of the tuning can be found, where the pulse is shortest. In the simulation however, a change of the tuning range would impose the need for a different tuning range, and this again would result in the need for a complete new simulation. A complete simulation for every small detuning however is simply not feasible. Therefore, the tuning range detuning is accounted for in the Matlab routine by multiplying $\Delta\omega_0$ with a factor that corresponds to the experimental detuning factor. We can then emulate this fine-tuning of the experiment for our pulse compression. It is always the case that the best result for the pulse length is very near to $\Delta\omega = \Delta\omega_0$, with a deviation in the range of 1%.

6.5.2.4 Unwrapping of the phase

In order to unwrap the phase $\Phi(\omega)$ from the Fourier transformed field $\tilde{A}(z, \omega)$ in the frequency domain, we use Matlab's unwrap routine, which extracts the phase from a complex valued array, displaying the field in the form $\tilde{A}(z, \omega) = |\tilde{A}(z, \omega)| e^{i\Phi(\omega)}$. In the simulation, the position z is fixed after the SOA, corresponding to the light being coupled out in the experiment via the 50/50 FC 6.4.1. Therefore the position dependency is eliminated, so that we have $\tilde{A}(\omega) = |\tilde{A}(\omega)| e^{i\Phi(\omega)}$.

6.5.2.5 Cut-out window and compensation of phase oscillations

Before performing the phase compensation itself, another effect is taken into account that could possibly lead to phase oscillations. The cut-out window in the experiment is $\Delta\tau = 24$ ns. We take this into account by dividing the field $\tilde{A}(\omega)$ into 128 subintervals, so that one subinterval corresponds to $T_R/128 =$

$2.56/128\mu\text{s}=20$ ns. Because of the FFTW algorithm, the number of subintervals has to be a power of 2, with 128 being most suitable, yielding a subinterval length that is with 20 ns very near to the actual cut-out window of 24 ns. As in the experiment, we now cut-out a 20 ns portion of $A(t)$ at the steepest point of the sweep, then Fourier transform this portion of $A(t)$ into the frequency domain, yielding $\tilde{A}(\omega)$. However, now the problem can arise that to the left and to the right of $\tilde{A}(\omega)$, the pulse is immediately cut-off, giving rise to oscillations when Fourier transforming. This can be overcome by adding zero-valued entries to the left and the right of $\tilde{A}(\omega)$. Afterwards, this effect is subtracted again. By this method, artificially caused phase oscillations are suppressed.

6.5.2.6 Compensation of the phase

After all these steps, the last step is to compensate the pulse. This is achieved by subtracting the average phase from the 20 roundtrips $\Phi(\omega)_{avg}$ from the phase $\Phi(\omega)$ that we have unwrapped from $\tilde{A}(\omega)$. We then have only a very small residual phase left. This process is analogous to a phase compensation with the best possible fit curve. Then, we Fourier transform back into the time domain, and now have the compressed pulse field

$$A(t)_{comp} = \mathcal{F}^{-1}[|\tilde{A}(\omega)|e^{i(\Phi(\omega)-\Phi(\omega)_{avg})}]. \quad (6.5.2)$$

6.5.2.7 Frequency detuning

In the experiment, the no-detuning case is found by fine-tuning the sweep filter driver frequency so that the instantaneous power spectrum has the highest intensity. This is also the case where we have the best compression. However, it is not pre-defined that the case for no detuning in the experiment, matches also the case for no detuning, e.g $\Delta f = 0$ Hz in the simulation. The no detuning condition in the experiment is not 100% accurate, so that we can witness in the simulation the best case compression at a detuning different than zero. This case then corresponds to the experimentally witnessed case. Later on we also investigate the role of detuning on the pulse length.

6.5.2.8 Results from the numerical simulation

Several simulations have been performed, with different detunings, ranging from $\Delta f = -0.5$ Hz to $\Delta f = 0.5$ Hz in steps of 0.1 Hz. This is done in order to investigate the dependence of the pulse compressibility on the detuning. We can then find the case where the pulse length is shortest, which as stated does not necessarily have to be $\Delta f = 0$ Hz. The pulse length can further be optimized by fine-tuning the tuning range $\Delta\omega$, analogous to the experiment. In order to check for a potential optimization of the pulse length, for future applications, cases have been also simulated where the FWHM sweep filter bandwidth is changed, ranging from a very narrow bandwidth of 1 pm to 400 pm, with the standard setting of figure 6.4.1 being 310 pm. Also, a perfect dispersion compensation has been investigated, in

order to verify if a potential better dispersion compensation in future experimental setups could have an impact on the pulse length. In Table 6.1, the FWHM pulse lengths are shown for different settings of detuning. A strong dependency on the detuning is found, with the dependency decreasing at lower filter bandwidths. It is also found that the case with 0% dispersion and very narrow filter bandwidths delivers very short pulses, that come down to the range of the time-bandwidth product. In Fig. 6.5.1, a typical simulated pulse compression is shown, with the tuning for $\Delta\omega = \Delta\omega_0$, which means that the detuning of the tuning range is zero. In Fig. 6.5.1(a), the cut-out of the power over time is shown in the time domain. The length of the cut-out is 20 ns. In (b), the Fourier transformed spectral power density is shown in the frequency range where it is different from zero. In (c), the spectral phase $\Phi(\omega)$ is plotted in green, whereas the phase that is averaged over 20 roundtrips, $\Phi(\omega)_{avg}$ is drawn also, but it is directly covered by $\Phi(\omega)$, because the phase difference is so small.

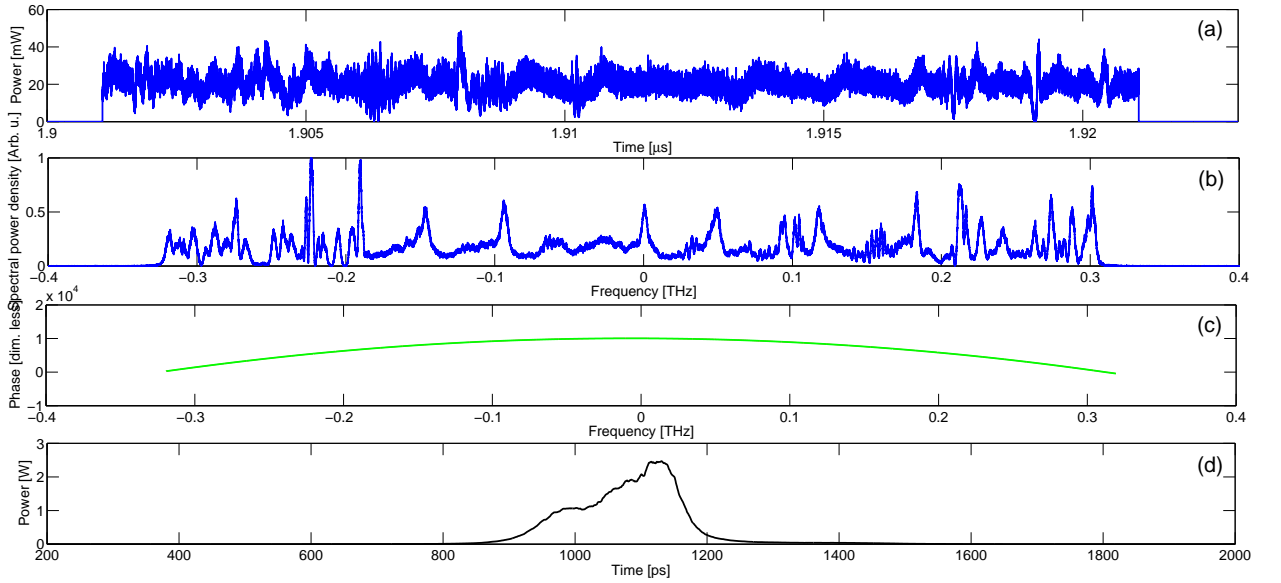


Figure 6.5.1: (a) The cut-out of the power over time, with a duration of 20 ns. (b) The spectral power density of the cut-out in the frequency domain. (c) The spectral phase distribution. The phase $\Phi(\omega)$ and the averaged phase $\Phi(\omega)_{avg}$, which is then subtracted, are in this plot indistinguishable, because the difference is only very small. (d) The compressed pulse with a length of 84 ps. The finite resolution of the sampling oscilloscope is emulated by the smoothing of the pulse. This smoothing lengthens the pulse by 45 ps. This effect is then subtracted, which results in the 84 ps pulse length.

Hence, the resulting subtracted phase is small, and when Fourier transforming back into the time-domain, the compressed pulse, shown in (d), is obtained. The pulse length in total is 129.64 ps (FWHM), however it is broadened by smoothing. The curve is smoothed in order to emulate the finite resolution of the analog sampling oscilloscope. By the process of the smoothing algorithm, the curve is broadened by an amount of 45.80 ps. In order to obtain the real pulse length, we have to subtract this artificial broadening effect, resulting in a pulse length of 83.84 ps. As will be shown in the next section, this result matches the experimental data well.

The process shown in Fig. 6.5.1 can then be applied to the other simulated data. The shortest pulses are then found for every case. The results in dependency of the detuning for the standard filter

Detuning [Hz]	-1.5	-1.0	-0.7	-0.6	-0.5	-0.4
Pulse length [ps]	283.27	188.93	147.65	118.51	106.67	83.84
Detuning [Hz]	-0.3	-0.2	0	0.2	0.5	1.0
Pulse length [ps]	142.59	160.91	176.20	179.52	181.35	246.50

Table 6.1: The results of the pulse lengths from the simulation in dependence of the detuning. As can be seen, the pulse length has the tendency to become larger for larger detunings, with the shortest pulse at -0.4 Hz. It is noteworthy that the shortest pulse is not located at 0 Hz detuning, but the zero detuning point in the experiment does not necessarily have to coincide with the zero detuning point in the simulation, as explained in chapter 6.5.2.7.

Detuning [Hz]	-0.4	-0.3	-0.2	-0.1	0
Filter bandwidth [pm]					
400	120.49	-	-	-	214
200	75.68	-	-	-	104.64
100	98.43	91.29	70.95	74.14	88.76
50	72.64	64.44	54.43	59.73	43.67
20	38.81	32.64	24.46	28.85	34.51
10	13.07	13.26	11.64	17.77	14.88
5	-	-	-	-	16.19
2	-	-	-	-	1544
1	-	-	-	-	$2 \cdot 10^4$

Table 6.2: The pulse length in ps in dependency of the detuning and the sweep filter bandwidth. The dashes mean that these points have not been simulated. As can be seen, the detuning dependency decreases with smaller filter bandwidths. It is also noteworthy that below 10 pm filter bandwidth, the pulse length begins increasing again, and between 5 pm and 2 pm there is a huge increase, resulting in non-existent compression at 1 pm bandwidth. In this case, there is no compression possible and therefore the pulse length equals the time length of the cut-out window. The pulse length decreases until this point with smaller filter bandwidths, reaching the smallest value at 10 pm filter bandwidth and -0.2 Hz detuning. Because the detuning is symmetric with respect to the pulse lengths, only the negative detuning has been simulated.

bandwidth of 310 pm are shown in Table 6.1.

In Table 6.2, the results for different sweep filter bandwidths are shown, and their dependence on the detuning. Because the detuning is symmetric with respect to the pulse lengths, only the negative detuning has been simulated. Several conclusions can be drawn from the results. First, the dependency of the pulse length from the detuning decreases with smaller filter bandwidth. Therefore, for small filter bandwidths it suffices to only simulate on detuning, in this case zero detuning. Secondly, the pulse length gets shorter for smaller filter bandwidths, with the shortest pulse having a length of 11.64 ps at 5 pm filter bandwidth. Therefore, there lies enormous potential for shorter pulses in building sweep filters with smaller transmission bandwidths, a challenge for future FDML setups. The third result is that at a certain lower border for the sweep filter bandwidth, the pulse length dramatically increases. This barrier is located between 5 pm and 2 pm bandwidth, and for 1 pm there is already no pulse compression at all, because no single pulse is established, so that the pulse length equals the time cut-out window of 20 ns.

In order to further investigate possibilities of reducing the pulse length, also a perfect dispersion compensation has been investigated, resulting in absolute 0% dispersion for the setup. This perfect dispersion compensation can of course not be achieved under real circumstances, it is however nonetheless

Detuning [Hz]	-0.4	-0.2	0	0.2	0.4
Filter bandwidth [pm]					
310	136.92	150.18	11.07	152.17	188.04
5	-	-	-	-	0.563
1	-	-	-	-	0.423

Table 6.3: The pulse length in ps for perfect dispersion compensation (0% remaining dispersion in the cavity) in dependency of the detuning and the sweep filter bandwidth. It is noteworthy that now the shortest pulse is at 0 Hz detuning with a very short pulse length of 11.07 ps even at the standard filter bandwidth of 310 pm. For smaller filter bandwidths of 5 pm and 1 pm, very short pulses of several hundred femtoseconds can be achieved, which is in the order of the time bandwidth product of 100 fs.

interesting to see what pulse lengths are achievable and where the limit lies. The total limit is given by the time-bandwidth product, and as will be seen, for no dispersion and very small filter bandwidths, we achieve pulse lengths in the order of the time bandwidth product, being about 100 fs. The results are shown in Table 6.3. For the standard filter setting of 310 pm, detuning has also been investigated, and as can be seen very short pulse lengths of 11.07 ps can be achieved. Here however, the shortest pulse is located exactly at zero detuning. The effect that the shortest pulse has previously been located at detunings different from zero is therefore caused by the remaining dispersion in the cavity. For very short filter bandwidths, we reach time regions that are of the order of the time-bandwidth product which is around 100 fs for this setup.

6.5.3 Comparison with the experiment

In this section we compare the results from the simulated compression with the experimental data from the Robert Huber group of LMU München. In Fig. 6.5.2, the results for the pulse lengths in the experiment are shown [Eig11B]. In Fig. 6.5.2(a), a pulse is shown that is achieved for 1x DCF (see 6.4.1(a)) and a bandwidth of $\Delta\lambda \approx 6$ nm. The FWHM pulse length is 68 ps. In Fig. 6.5.2(b), the dependency of the pulse length from the detuning is shown. The asymmetry in the plot is artificially induced by the sampling oscilloscope. It can be seen that the shortest pulses are achieved for zero detuning. However, the zero detuning case does not necessarily coincide with the zero detuning from the simulation. The criterion for finding the zero detuning case in the experiment is the highest pulse intensity, which is not 100% accurate.

When we now compare the data from our simulations to the experiment, we can see that the pulse lengths agree well. From Fig. 6.5.2(a) we can extract a pulse length of 68 ps, whereas the shortest pulse from the simulation with standard filter bandwidth is 83.84 ps (see Table 6.1), only higher by a small amount. The deviation can be explained by the fact that the polarization dependency of the experimental setup is not incorporated into the simulation. Possible effects caused by polarization can hence lead to a higher compressability in the experiment that is not taken into account in the simulation. This could explain the shorter pulse length in the experiment. We can now plot the numerical results from Table 6.1 for different detunings and Table 6.2 for different filter bandwidths and compare it with the experimental

data. This is shown in Fig. 6.5.3.

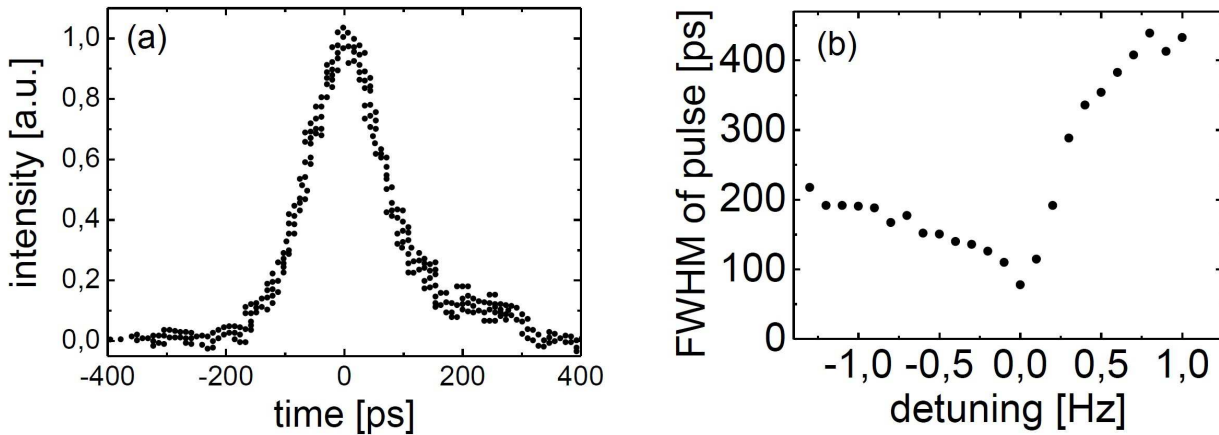


Figure 6.5.2: (a) Pulse with a length of 68 ps for 1x DCF and $\Delta\lambda \approx 6$ nm. (b) The dependency of the pulse length from detuning. The asymmetry is caused by the sampling oscilloscope.

In Fig. 6.5.3(a), the simulation results for the shortest pulses from Table 6.2 are plotted together with the two experimentally measured points for different filter bandwidths. It can be seen that the behaviour of the pulse length becoming shorter with smaller filter bandwidth is also present in theory. In theory, we can additionally lower the bandwidth to points that are not reachable in the experiment, far below 310 pm. It can be seen that the pulse length decreases to a very low 11.64 ps, before increasing again below 10 pm filter bandwidth. Therefore there is a lower limit to the pulse length with respect to the sweep filter bandwidth.

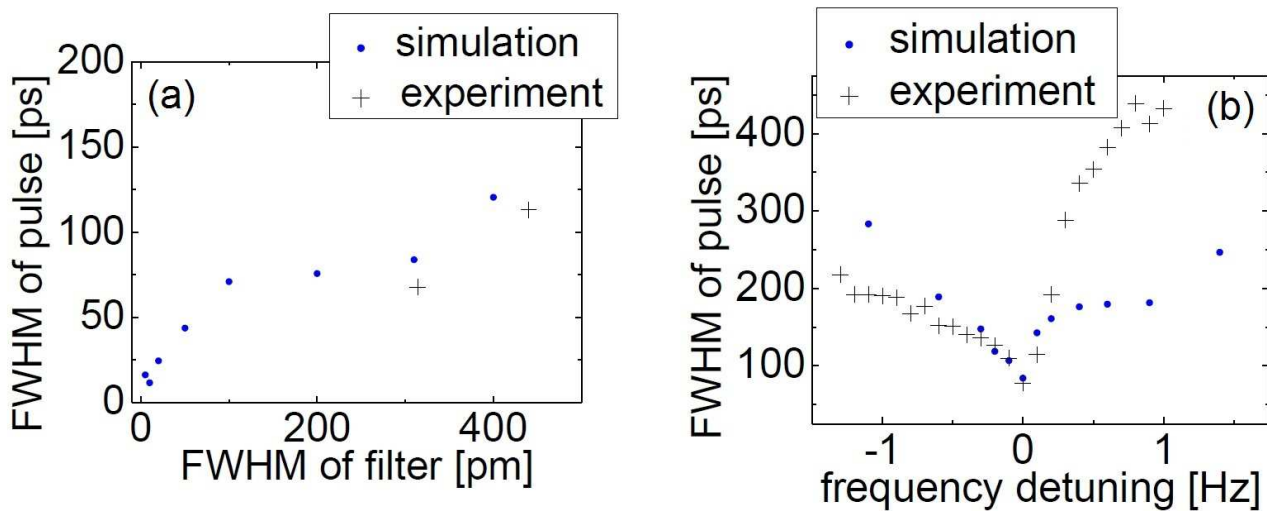


Figure 6.5.3: (a) The simulation data from Table 6.2 together with the experimental results [Eig11B]. As can be seen, the pulse length decreases with smaller filter bandwidths, reaching its minimum at 10 pm. The experimental data also shows that the pulse length decreases, which is measured for two different filter bandwidths. (b) The simulation data from Table 6.1 together with the experimental results. As can be seen, the general behaviour that the pulse length increases with higher detuning is also present in theory. In theory, the shortest pulse length is achieved at -0.4 Hz detuning with 83.84 ps. This is only slightly higher than the experimental result of 68 ps.

In Fig. 6.5.3(b) the simulated results are shown together with the experimental data for different filter detunings. As already stated, the asymmetric behaviour in the experiment is an artificial effect

induced by the sampling oscilloscope. Therefore, it is not present in the simulation data. However, a small asymmetry is also visible in the simulation data. The reason for this asymmetry lies in the pulse form. As can be seen in Fig. 6.5.1(d), the pulse has an asymmetric form itself. For certain cases, this asymmetry is quite large, so that an extension slope is present at one side of the pulse. If now this extension is only slightly above the FWHM threshold, the pulse length increases a lot. This is the case for the detunings -0,3 Hz to +0.2 Hz. Therefore it seems as if the pulse width is strongly increased. The general behaviour with respect to detuning however is very similar for the experimental and simulation data. As the point of zero detuning is not measurable with 100 % accuracy, it is acceptable to compare the -0.4 Hz detuning of the simulation to 0 Hz detuning in the experiment. Considering these effects, the results agree well, and the general behaviour matches also.

6.5.4 Optimization of the performance and future outlook

It has been shown that the FDML laser can be optimized for pulse compression in twofold ways. The first way is to build sweep filters with smaller bandwidths. In theory, the filter bandwidth can be changed in the simulation as wished, under real circumstances however, fabrication processes inhibit sweep filter bandwidths below a certain point. However, there is still great potential for smaller filter bandwidths and thus shorter pulses. In Table 6.3, the case of perfect dispersion compensation is shown, stating that perfect dispersion compensation would enable even shorter pulses, at a standard filter bandwidth of 310 pm, reaching a sharp limit of 11.07 ps at zero detuning. However, if a better dispersion compensation together with very short filter bandwidths is achieved at the same time, pulses in the range of the time-bandwidth product become feasible. In the simulation, the shortest pulse has a length of only 423 femtoseconds, only roughly 4 times the time-bandwidth limit. Even though under real circumstances, total dispersion compensation and very small filter bandwidths of below 20 pm cannot be achieved as of today, there is still great potential for improving both these properties. It is thus possible, that in future FDML setups, pulse lengths on the order of one picosecond can be achieved. This would open up a whole new field for FDML applications, for example in material processing.

Chapter 7

Analytical model for FDML operation

In order to better understand the underlying physical principles of FDML operation, an analytical solution to the FDML evolution equation (3.3.4) is a very desirable goal. In this chapter, we first start with a simplified form of the FDML evolution equation without self-phase modulation or third order dispersion, and without the gain saturation behavior. We then use a chirped Gaussian ansatz in order to solve this equation and investigate some properties of the solution. In the next step, we use the chirped Gaussian ansatz in order to solve the FDML evolution equation. We do this employing two different methods, first the variational approach [Arn89], and the method of moments [Bur07]. Both methods yield the same equations of motion, which are then to be solved, delivering the parameters for the chirped Gaussian ansatz. We can then compare the results from the analytical model with a simulation that solves the FDML evolution equation numerically. As will be seen, the resulting solution delivers not a cw-solution, but pulses with a length of about $1 \mu\text{s}$ for the FDML laser of Fig. 3.2.1 and Fig. 4.1.1. Therefore the chirped Gaussian solution cannot fully describe the FDML dynamics, but represents the lowest order solution of the FDML evolution equation. The exact solution has to be more general than the Gaussian solution. A more general solution is needed, where the Hermite-Gaussian model might be a possible ansatz [Pam04].

7.1 FDML laser with slow gain saturation

The FDML evolution equation (3.3.4) without instantaneous gain saturation does not take into account the gain saturation effects taking place in the SOA. This process is nonlinear and more difficult to solve than this simplified ansatz, therefore it is a good starting point in order to later on investigate more complicated solutions. The FDML evolution equation without gain saturation, third order dispersion and self-phase modulation is of the following form:

$$\partial_z u(z, t) = g_0(1 - i\alpha) - [g_\omega(1 - i\alpha) - iD_2] \cdot \omega_0^2(t) - a_l + (a_s - iD_2)\partial_t^2 u(z, t), \quad (7.1.1)$$

where $\omega_0(t)$ denotes the sweep filter driver function, that here is a ramp function of the form $\omega_0(t) = \frac{\Delta\omega}{T_R}t$. T_R denotes the roundtrip time of the laser, here $T_R = 17.32 \mu\text{s}$. The gain parameters g_0 and g_ω denote the saturated gain and the frequency dependent gain parameters. The parameters a_l and a_s denote the cavity and the sweepfilter loss coefficients, respectively. The linewidth-enhancement or Henry factor is denoted by α [Hen82]. In this model, the sweep filter is implemented as a Gaussian filter, therefore it is multiplied with ∂_t^2 , instead of a Lorentzian sweepfilter $a_s(i\partial_t)$. In our case, the laser parameters are position independent because the optical elements are here distributed over the resonator. We now choose a chirped Gaussian ansatz of the form

$$u(z, t) = u_0 e^{\kappa z} e^{-t^2(\frac{1}{2T^2} - ib)}. \quad (7.1.2)$$

Here, κ denotes a complex phase parameter, T is the length of the Gaussian pulse, and b is the chirp parameter. Inserting (7.1.2) into (7.1.1) yields

$$\kappa u(z, t) = \left[g_0(1 - i\alpha) - g_\omega(1 - i\alpha) \frac{\Delta\omega^2}{T_R^2} t^2 + iD_2 \frac{\Delta\omega^2}{T_R^2} t^2 - a_l \right] + \quad (7.1.3)$$

$$(a_s - iD_2) - 2 \left(\frac{1}{2T^2} - ib \right) + \left[-2t \left(\frac{1}{2T^2} - ib \right) \right]^2 u(z, t). \quad (7.1.4)$$

The real part of the phase parameter κ must vanish, else $u(z, t)$ would either vanish for $z \rightarrow \infty$ and $\mathcal{R}\{\kappa\} < 0$, or get infinitely large for $z \rightarrow \infty$ and $\mathcal{R}\{\kappa\} > 0$. Therefore we have the constraint $\mathcal{R}\{\kappa\} = 0$ and through comparing the coefficients we get the two conditions

$$a_l + \frac{a_s}{T^2} - g_0 = 2D_2b; \quad (7.1.5)$$

$$\frac{a_s}{T^4} - g_\omega \frac{\Delta\omega^2}{T_R^2} = 4a_s b^2 + \frac{4D_2b}{T^2}. \quad (7.1.6)$$

For the imaginary part $\mathcal{I}\{\kappa\}$ we get in the same way the two conditions

$$\mathcal{I}\{\kappa\} + g_0\alpha - \frac{D_2}{T^2} = 2ba_s; \quad (7.1.7)$$

$$\frac{D_2}{T^4} - \frac{g_\omega\alpha\Delta\omega^2}{T_R^2} - \frac{D_2\Delta\omega^2}{T_R^2} = 4b^2D_2 - \frac{4ba_s}{T^2}. \quad (7.1.8)$$

So we have a set of 4 equations for the unknowns g_0 , $\mathcal{I}\{\kappa\}$, T and b , depending on the laser parameters a_l , a_s , D_2 , g_ω , $\Delta\omega$, T_R and α . Solving these four equations with respect to the unknowns, yields four solutions for every unknown. The physically relevant solution is the solution where T is real and positive, and the solutions for the other parameters are the ones linked to this solution. Solving (7.1.6) with respect to b yields a quadratic equation for b with the solutions

$$b_{1/2} = -4D_2 \pm \sqrt{16D_2^2 - 16a_s T^2 \left[(g_\omega - D_2 \alpha) \frac{\Delta\omega^2 T^2}{T_R^2} - \frac{a_s}{T^2} \right]} \frac{1}{8a_s T^2}. \quad (7.1.9)$$

Inserting this into (7.1.8) yields a fourth order equation for T that depends only on the laser parameters:

$$\frac{\Delta\omega^2}{T_R^2} \left[\frac{D_2(g_\omega - D_2 \alpha)}{a_s} - g_\omega \alpha - D_2 \right] = \frac{1}{T^4} \left[2D_2 \left(\frac{D_2^2}{a_s^2} + 1 \right) + \left(\frac{D_2^2}{2a_s^2} \mp \frac{1}{2} \right) \sqrt{16(D_2^2 + a_s^2) - \frac{16a_s(g_\omega + D_2 \alpha)\Delta\omega^2}{T_R^2} T^4} \right]. \quad (7.1.10)$$

The positive and real solution for T can be written as

$$T = \left(\frac{a - b + c - d - e - f - g - h + k}{l} \right)^{1/4}; \quad (7.1.11)$$

with $a, b, c, d, e, f, g, h, k, l$ being lengthy terms of the FDML parameters (see Appendix D). The corresponding chirp is also given in Appendix D. We use the laser parameters as in the experimental setup, shown in Table 7.1. We find that $T = 1.216$ ns. This is a very short pulse compared to the roundtrip time $T_R = 17.32$ μ s. This simplified model cannot explain the cw output of the FDML laser. However, it can be used as a model for an FDML laser with a slow saturable gain absorber, vanishing nonlinearity and third order dispersion. With such an FDML laser, a pulsed mode could be achieved without the need for additional dispersion compensation as described in the previous chapter.

7.2 FDML laser with gain saturation, self-phase modulation and dispersion

The more complicated case arises when the gain saturation is also considered. This means that the gain of the medium is dependent on the power of the light field $|A(z, t)|^2$, as explained in chapter 2.4.1. We here use a linearized gain ansatz, where the nonlinear behavior is accounted for with a nonlinearity factor r . It is given by the relation $r = 1/(2P_{sat}L)$ [Jir11]. In our case it has a value of $r = 0.3667$ $\text{W}^{-1}\text{m}^{-1}$. In addition, we also take into account the nonlinearity γ and the third order dispersion. We can then write the FDML evolution equation (3.3.4) as

$$\begin{aligned} i\partial_z u - D_2 \partial_t^2 u + \gamma |u|^2 u + D_2 \frac{\Delta\omega^2}{T_R^2} t^2 u - \alpha \left(g_0 - r |u|^2 - g_\omega \frac{\Delta\omega^2}{T_R^2} t^2 \right) u = \\ = i \left(g_0 - r |u|^2 - g_\omega \frac{\Delta\omega^2}{T_R^2} t^2 - a_l + a_s \partial_t^2 \right) u. \end{aligned} \quad (7.2.1)$$

In order to solve this equation we again use a chirped Gaussian ansatz. There are now two methods

to deduce the equations of motion for this problem. The first one is the variational principle [Arn89]. It is based on the principle that the action functional of a physical system is extremal [Ham34]. From this, the Lagrangian equations are derived, which are a set of partial differential equations that describe a conservative, as well as a non-conservative system. In Appendix B, we derive the equations of motion for (7.2.1) using the variational principle for a chirped Gaussian test-function.

Another possibility of deducing the equations of motion is the use of the method of moments [Bur07], [Jir11]. In this approach, generalized moments are used to derive the energy and momentum of a test-function. There are higher order moments also, and relations between the moments are used to derive the evolution equations [Jir11]. In Appendix C, the derivation of the equations of motion is done using the method of moments and a chirped Gaussian test-function. Both methods are equivalent, and yield the exact same equations of motion for (7.2.1). The chirped Gaussian test-function is chosen in both cases, because it is the exact solution to the example of an FDML laser with instantaneous gain saturation, as shown in the previous section. Therefore, it is investigated if the chirped Gaussian ansatz is also suited for the case of gain saturation and additional self-phase modulation and third order dispersion. The chirped Gaussian ansatz is again of the form

$$u(z, t) = Ae^{i\Phi(z)}e^{-t^2(\frac{1}{2T^2} - ib)}, \quad (7.2.2)$$

with an amplitude A , a phase factor Φ , chirp b and the pulse length T . The equations of motion for the FDML laser of this example can then be written as:

$$\frac{\partial b}{\partial z} = -\frac{4a_s b}{T^2} + 4D_2 b^2 - \frac{D_2}{T^4} - \frac{(\gamma + \alpha r)A^2 \sqrt{2}}{4T^2} + \frac{(D_2 + \alpha g_\omega)\Delta\omega^2}{T_R^2}; \quad (7.2.3)$$

$$\frac{\partial T}{\partial z} = -4D_2 b T - g_\omega \frac{\Delta\omega^2}{T_R^2} T^3 + \frac{a_s}{T} - 4a_s b^2 T^3; \quad (7.2.4)$$

$$\frac{\partial A}{\partial z} = 2D_2 b A + g_0 A - \frac{rA^3}{\sqrt{2}} - a_l A - \frac{a_s A}{T^2}. \quad (7.2.5)$$

The evolution equation for Φ is decoupled, and thus can be ignored in the following. A constant phase factor does not contribute to the physical properties of the pulse, and later on the power is investigated. This simplifies the solution and the steady-state solution is easier to find. The condition for the steady state solution is

$$\frac{\partial A}{\partial z} = \frac{\partial b}{\partial z} = \frac{\partial T}{\partial z} = 0. \quad (7.2.6)$$

Therefore the condition that has to be fulfilled for the steady-state, is:

$$-\frac{4a_s b}{T^2} + 4D_2 b^2 - \frac{D_2}{T^4} - \frac{(\gamma + \alpha r)A^2 \sqrt{2}}{4T^2} + \frac{(D_2 + \alpha g_\omega)\Delta\omega^2}{T_R^2} = 0; \quad (7.2.7)$$

$$-4D_2bT - g_\omega \frac{\Delta\omega^2}{T_R^2} T^3 + \frac{a_s}{T} - 4a_s b^2 T^3 = 0; \quad (7.2.8)$$

$$2D_2b + g_0A - \frac{rA^2}{\sqrt{2}} - a_l - \frac{a_s}{T^2} = 0; \quad (7.2.9)$$

After a certain amount of space propagated through the FDML laser, the light in the cavity does not change any more, except for ASE induced small fluctuations [Jir08]. Therefore, the steady-state solution is of interest, because it describes the field after a certain number of roundtrips. The equations (7.2.7)-(7.2.9) can now be solved in order to find the values of A , b and T in dependence of our laser parameters. For this, two methods are employed, the first one being solving the equation analytically, and the second one being a numerical simulation in order to find the steady-state solution.

7.2.1 Spatial evolution of amplitude, chirp and pulse length

In the following, we investigate the spatial evolution of the amplitude, the chirp and the pulse length. The equations (7.2.3)-(7.2.5) show the evolution of the parameters for the amplitude A , the chirp b and the pulse length T over the distance z that has been travelled in the resonator. Solving this set of coupled partial differential equations gives us the spatial evolution of these parameters. This is done by solving the equations of motion in Matlab, using the built-in ODE45 ordinary differential equation solver.

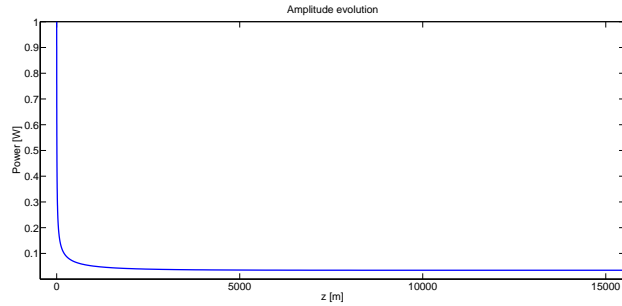


Figure 7.2.1: The spatial evolution of the amplitude is shown here. It can be seen that after about 10^4 m, which corresponds to about three roundtrips, the power does not change any more. It converges towards a value of 34.6 mW.

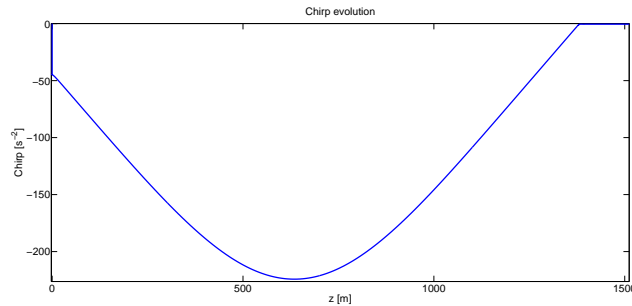


Figure 7.2.2: Here, the spatial evolution of the chirp is shown. It can be seen that the chirp first decreases with increasing z , then reaches a minimum after about $6 \cdot 10^3$ m, then rises again and reaches convergence towards a value of $1.649 \cdot 10^9$ s⁻² after a distance of about $1.4 \cdot 10^4$ m, which corresponds to about four roundtrips.

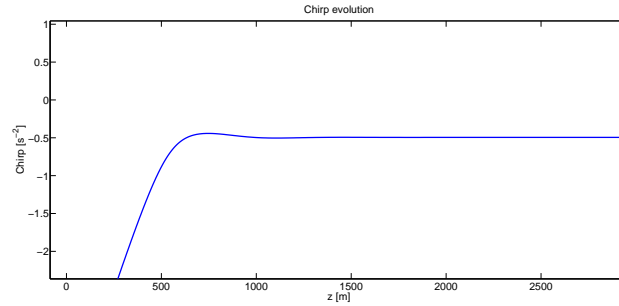


Figure 7.2.3: This is a zoomed in portion of the chirp evolution, in order to better illustrate the point where convergence is reached.

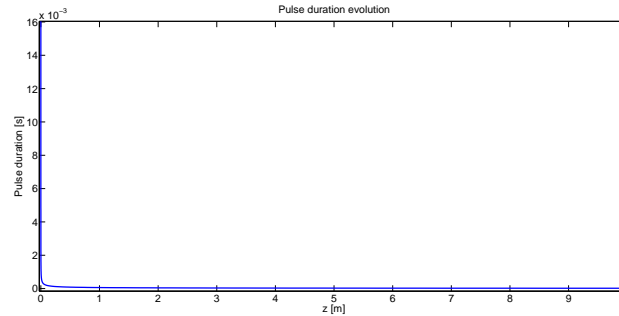


Figure 7.2.4: The spatial evolution of the pulse duration. It can be seen that after a few meters, the pulse duration has already converged towards a value of $19.373 \mu\text{s}$.

The spatial evolution of the parameters is shown in Fig. 7.2.1, in Fig. 7.2.2, in Fig. 7.2.3 and in Fig. 7.2.4 in more detail. For this, again the laser input values from Table 7.1 are used. As can be seen, the parameters start at a reasonably chosen initial value, and then move towards a static value, they have an asymptotic behavior. They converge towards the steady-state with a different speed, where the pulse duration reaches convergence fastest, and the chirp slowest. The end value is then the steady-state solution, described by (7.2.7) (7.2.9). The values for A , b and T can be extracted and yield $|A|^2 = 34.6 \text{ mW}$, $b = -1.649 \cdot 10^9 \text{ s}^{-2}$ and $T = 19.373 \mu\text{s}$. For the FWHM pulse length we therefore have $T_{FWHM} = 45.62 \mu\text{s}$. This is longer than the sweep duration, but this is no contradiction to the model, assuming that the sweep duration is fixed, and that the Gaussian begins anew with each sweep. The properties of the solution are discussed in the next section.

7.3 Steady state solution

7.3.1 Analytical solution

In the previous section, the steady-state solution has been found to be the asymptotic limit of the parameters A , b and T , and the limit has been found by solving the equations of motion with a numerical ordinary differential equation (ODE) solver. But, as in Chapter 7.1, the equations can also be solved analytically, with solutions for A , T and b in dependence of the laser parameters γ , D_2 , D_3 , $\Delta\omega$, T_R , α , g_0 , g_ω , r , a_l and a_s . We start by solving (7.2.8) with respect to b , which yields two solutions, because it

is a quadratic equation. We then get for b

$$b_{1/2} = \frac{-D_2 T^2 T_R^2 \pm \sqrt{-a_s \Delta\omega^2 g_\omega T^8 T_R^2 + a_s^2 T^4 T_R^4 + D_2^2 T^4 T_R^4}}{2a_s T^4 T_R^2}. \quad (7.3.1)$$

The solution for A can be directly derived from (7.2.9), and yields

$$A = \pm \sqrt{\frac{\sqrt{2}}{r} \left(2D_2 b + g_0 - a_l - \frac{a_s}{T^2} \right)}. \quad (7.3.2)$$

We can now insert both solutions into (7.2.7) and we get a polynomial of order 12 in T , which depends on the laser input parameters. The laser parameters for the experimental setup of Fig. 3.2.1 and Fig. 4.1.1 are listed in Table 7.1. We can then solve the polynomial and find all positive and real solutions for T .

Laser parameter	value
$\Delta\omega$	$1.134 \cdot 10^{14} \text{ s}^{-1}$
g_ω	$3.0026 \cdot 10^{-30} \text{ s}^2 \text{ m}^{-1}$
a_s	$1.2673 \cdot 10^{-26} \text{ s}^2 \text{ m}^{-1}$
α	5
T_R	$1.732 \cdot 10^{-5} \text{ s}$
a_l	$3 \cdot 10^{-4} \text{ m}^{-1}$
D_2	$-2.7603 \cdot 10^{-28} \text{ s}^2 \text{ m}^{-1}$
g_0	$6.104 \cdot 10^{-4} \text{ m}^{-1}$
γ	$0.00136 \text{ W}^{-1} \text{ m}^{-1}$
r	$0.3667 \text{ W}^{-1} \text{ m}^{-1}$

Table 7.1: The laser parameters for the experimental setup as in Fig. 3.2.1 and Fig. 4.1.1.

We now can retrieve the values for T , b and for A , yielding the same values as in the previous subsection: $|A|^2 = 34.6 \text{ mW}$, $b = -1.649 \cdot 10^9 \text{ s}^{-2}$ and $T = 19.373 \text{ } \mu\text{s}$. This is a crosscheck of the previous results.

7.3.2 Properties of the steady-state solution

By solving the equations of motion, we have found the steady-state solution for the chirped Gaussian ansatz (7.1.2). Since the steady-state solution is based on a Gaussian model, the double peaked nature of the FDML power output, shown in Fig. 3.4.3, cannot be reproduced with this model.

The chirp can be plotted by rewriting the ansatz (7.1.2):

$$u(z, t) = A e^{i\Phi(z)} e^{-t^2 \left(\frac{1}{2T^2} - ib \right)} = A e^{-\frac{t^2}{2T^2}} [\cos(bt^2 + \Phi) + i \cdot \sin(bt^2 + \Phi)]. \quad (7.3.3)$$

Taking the real part yields

$$u(t) = A e^{-\frac{t^2}{2T^2}} \cos(bt^2 + \Phi). \quad (7.3.4)$$

The chirped nature of the field (red curve) is drawn in 7.3.1 together with the power output (blue curve). Since the output is cw, the output is periodical and repeats with each new sweep.

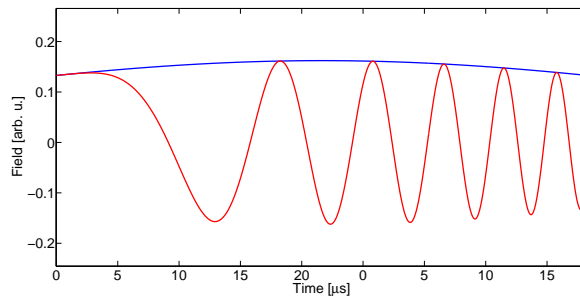


Figure 7.3.1: Here, the chirped nature of the field (red curve) has been additionally drawn together with the power output (blue curve).

Now it is interesting to see which parameters of Table 7.1 can be changed and what effect this has on the power output. Also, the uncertainty of the parameters is investigated, in order to check if slightly changed parameters within error bounds describe the observed FDML output better.

7.3.3 The frequency dependent gain parameter g_ω

Increasing the frequency dependent gain parameter results in an increase of the chirp and of the pulse length. Increasing g_ω by an order of magnitude leads to a chirp that is a factor two smaller, and a pulse duration that is a factor three smaller.

7.3.4 The gain parameter g_0

Increasing this parameter by an order of magnitude leads only to a change in the power amplitude, an increase of $\approx 10\%$. The certainty of this parameter is high and leads only to a slight change of the output.

7.3.5 The sweep range $\Delta\omega$

This parameter has a very high impact on the chirp and on the pulse duration. Increasing $\Delta\omega$ by a factor of two already increases the chirp by a factor of ≈ 3 and reduces the pulse duration by a factor of ≈ 2 . These parameters would describe the observed FDML output better than the standard parameter. Since the chirped Gaussian model is a simplified model that does not take the full gain dynamics into account, and also leaves the third order dispersion out, it is possible that an increased $\Delta\omega'$ describes the FDML dynamics better than the standard value. In Fig. 7.3.2, the output is shown for $\Delta\omega' = 2 \cdot \Delta\omega$, with $\Delta\omega$ being the standard value from Table 7.1.

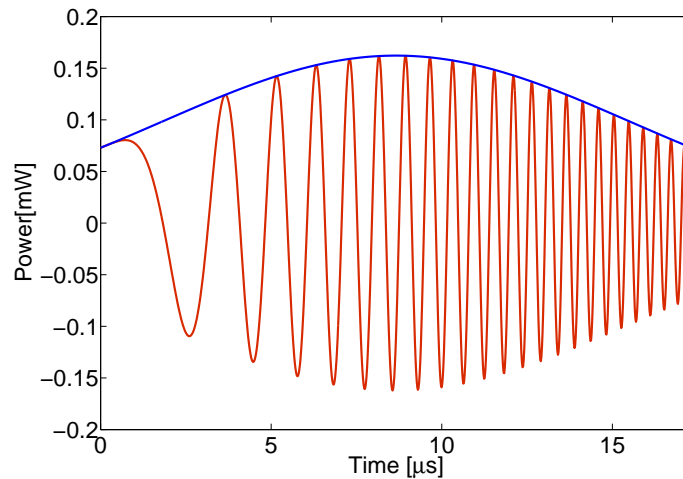


Figure 7.3.2: The FDML power output (blue curve) and the chirped field (red curve) for $\Delta\omega = 2 \cdot \Delta\omega_0$. This output fits the observed output better, in that the chirp is higher and the variation of the pulse power by a factor of ≈ 2 is also present, as seen in 3.4.3.

7.3.6 The sweep filter loss parameter a_s

Changing this parameter has a moderate impact on the chirp in the order of 10%, the power amplitude or the duration of the output.

7.3.7 The Henry factor α

A change of this parameter leads to a small change of the chirp. Decreasing α for example by a factor of 5 leads to an increase of 3% for the chirp, which is also negligible.

7.3.8 The sweep length T_R

Decreasing the sweep length T_R has a similar effect on the chirp and the duration as increasing the sweep range $\Delta\omega$. This is another indicator for the limitations of the chirped Gaussian model. A sweep length which is only half the initial sweep length leads to a power output that is very similar to the one shown in 7.3.2.

7.3.9 The overall cavity loss a_l

Increasing the loss leads to a decrease of the power amplitude and vice versa. An increase of an order of magnitude in the loss leads to a decrease of the output power of 3%, which is way below expectations. However, the tendency is correctly described by the model.

7.3.10 The second order dispersion coefficient D_2

The second order dispersion coefficient has a very high impact on the chirp parameter. Changing D_2 by an order of magnitude leads also to a change of b of an order of magnitude into the same direction.

7.3.11 The nonlinearity γ

Changing the nonlinearity in this model has only a very small impact on the chirp parameter, and does not change the other parameters

7.3.12 The saturation parameter r

The saturation parameter has an impact on the Amplitude of the steady-state solution. Changing this parameter by a factor of two leads to a change in the amplitude A by 41 %. It has no impact on the chirp or the time duration.

7.3.13 The instantaneous linewidth

Since the instantaneous linewidth is one of the most important parameters for FDML operation, and a large part of this thesis treats the evolution of the instantaneous linewidth, it is here interesting to see if this model can correctly predict the instantaneous linewidth. For the standard laser parameters of Table 7.1, we get as a result from the chirped Gaussian via Fourier transformation the spectral width corresponding to the instantaneous linewidth. The result is 0.11 GHz, about an order of magnitude lower than typically obtained values from previous chapters, which are in the range of several GHz. However, this model is simplified compared to the numerical simulation. Since the full gain dynamics is not implemented in this model, only a linearized ansatz, and the linewidth is in a large part governed by the gain, the result of 0.11 GHz is acceptable. Further theoretical work is however necessary in order to better understand the underlying mathematical principles in FDML operation, which govern the instantaneous linewidth.

7.4 Summary of the model and future outlook

The chirped Gaussian model in this chapter serves as a first simple model for describing the FDML output. As shown, several characteristics of the power output in 3.4.3 could be foretold by this model. For example the power change over time that is characteristic for the FDML output can be reproduced to a certain extent. However, the observed fluctuation of almost a factor of 3 can only be reproduced if $\Delta\omega$ is increased by at least a factor 2 in the model, or if the sweep length is decreased by at least a factor 2. Also, the chirped nature of the output is implemented in this model, however, here also the chirp is more like the observed chirp when $\Delta\omega$ or T_R are changed. The chirped nature of the output is inherent in the model, also the power fluctuations. Also, changing the cavity loss leads to a correct prediction of the power amplitude change, albeit the effect being smaller than would be the case in reality. Summarizing all these points, it is clear that the chirped Gaussian ansatz only serves as a first starting point for further investigations of analytically describing the FDML dynamics. The double-peaked nature of the output, as well as the correct prediction of the power scale, the correct scale of changes of the laser parameters,

cannot be satisfactory foretold by the model. Since the gain dynamics are simplified, here a linearized gain saturation model is used, and third order dispersion has been neglected, and the ansatz is also only the exact solution for the case of an instantaneous gain saturation. In this case however, it has been shown that the chirped Gaussian can serve as a model for an FDML laser with almost instantaneous gain saturation. Such a laser could emit short pulses without the need for compression by dispersion compensation.

The chirped Gaussian model for gain saturation can be used as a first starting point for further analytical investigations of FDML dynamics, for example employing a Hermite-Gaussian ansatz. In this model, the solution of the FDML equation (7.2.1) is a Hermite-Gaussian, which is similar to a harmonic potential problem from quantum mechanics. Such a model may be a starting point for more complex investigations of the FDML dynamics, and may lead to a full analytical description of FDML lasers.

Chapter 8

Summary and future outlook

In this work, several key effects of FDML operation are explained, and new insight is gained into the functioning mechanisms of FDML lasers. The first analysis treats the instantaneous lineshape of FDML lasers. Here, a model is developed in order to correctly predict the instantaneous lineshape, and comparison with the experiment yields good agreement. By subsequently turning on- and off certain parameters from the FDML evolution equation, the impact on the instantaneous lineshape is investigated. Here, a new discovery is made, finding that the linewidth is not dominated by ASE. This means, that in contrast to other known laser sources, completely turning off ASE in the simulation does not lead to an observable effect in the instantaneous lineshape. Therefore, the linewidth in an FDML laser is not generated by ASE or external noise sources, but is based entirely on the intrinsic physical properties of an FDML laser.

The investigation of the spatio-temporal dynamics gives insight into the balance of the physical effects that lead to stationary operation of FDML lasers. The spectral shaping effects are analyzed, and not only the impact of each physical quantity on the linewidth itself is analyzed, but also on the overall shape and frequency shift. Here, it is found that the combination of the gain recovery dynamics and the linewidth-enhancement in the SOA lead to a redshift of the instantaneous power spectrum. It is also found that the dispersion causes a time-dependent spectral shift. These effects are counterbalanced by the asymmetric absorption of the sweep filter. For a red-shifted spectrum, the sweep filter transmission function causes an effective shift to higher frequencies by reducing the low-frequency spectral wing. It is also found that self-phase modulation in the long delay fiber causes spectral broadening. The broadening on the other hand is counterbalanced by the tunable bandpass filter, narrowing the spectrum again by the repetitive filtering in each roundtrip. In summary, a detailed analysis of the optical field propagation in an FDML laser is presented for the first time. Also good agreement with the experimental data provided by the Robert Huber's group from LMU München is found, further validating the work. These new insights are an important step towards understanding the fundamental mechanisms leading to a steady state field in the FDML laser, and these results could lead towards a further optimization of FDML lasers in the near future.

In the next step, it is for the first time shown that FDML lasers are suited for the emission of short pulses, with shortest pulses being in the 60 ps range. Based on the numerical simulations also used for the previous investigations, a new code is developed in order to simulate the pulse compression which takes place in the experiment. The results are that FDML lasers can be optimized in terms of pulse compression in twofold ways. The first way is to build sweep filters with smaller bandwidths. In the experiment, production of filter bandwidths below a certain point is not possible with current methods, but theory shows that there is great potential for future optimization in this respect. It is also found that better dispersion compensation can also lead to better compressability. These two effects combined offer the chance to get into time regions given by the time-bandwidth product, namely a few hundred picoseconds. Comparing the numerical data with the experimental data also shows good agreement. Based on these results, further optimization of the FDML laser in this field is very likely in the near future.

Employing an analytical model for the solution of the FDML evolution equation, yields that a chirped Gaussian ansatz can be used as a solution for a special case of the FDML laser: an FDML with an instantaneous gain behavior and without third order dispersion or self-phase modulation. In this case, the model shows that short pulses in the nanosecond range can be produced without the need for post-dispersion compensation. Taking into account the above mentioned effects, and also including a linearized gain saturation model, it is shown that the chirped Gaussian ansatz can only describe the most fundamental properties of the FDML output, but fails to completely describe the nature of the power output. However, this model can serve as a first starting point for a full analytical model of FDML operation by generalizing the chirped Gaussian ansatz to a Hermite-Gaussian ansatz, which provides increased flexibility.

Appendix A: Fourier transform

Given is a complex function U , that can in general depend on the position $\mathbf{r} = (x, y, z)^T$ and the time variable t . The Fourier transform is then given by

$$\mathcal{F}_t\{U(t)\} = \tilde{U}(\omega) = \int_{-\infty}^{\infty} U(t)e^{i\omega t} dt. \quad (8.0.1)$$

And correspondingly for the inverse Fourier transform, we have

$$\mathcal{F}_\omega^{-1}\{\tilde{U}(\omega)\} = U(t) = \frac{1}{2\pi} \int_{-\infty}^{\infty} U(\omega)e^{-i\omega t} d\omega. \quad (8.0.2)$$

A.1 Differentiation

A time derivate of order n in time-space can be translated into Fourier space by the following relation:

$$\begin{aligned} \frac{\partial^n}{\partial t^n} U(t) &= \frac{\partial^n}{\partial t^n} \frac{1}{2\pi} \int_{-\infty}^{\infty} U(\omega)e^{-i\omega t} d\omega = \\ \frac{1}{2\pi} \int_{-\infty}^{\infty} (-i\omega)^n U(\omega)e^{-i\omega t} d\omega &= \mathcal{F}_\omega^{-1}\{(-i\omega)^n U(\omega)\}. \end{aligned} \quad (8.0.3)$$

Analogous, a frequency derivative of order n in Fourier space can be translated into the time domain by

$$\begin{aligned} \frac{\partial^n}{\partial \omega^n} U(t) &= \frac{\partial^n}{\partial \omega^n} \int_{-\infty}^{\infty} U(t)e^{i\omega t} dt = \\ \int_{-\infty}^{\infty} (it)^n U(t)e^{i\omega t} dt &= \mathcal{F}_t\{(it)^n U(t)\}. \end{aligned} \quad (8.0.4)$$

Appendix B: Variational principle

The first step is to find a Lagrangian for the system. Here, we have a Lagrangian \mathcal{L} which describes the conservative, i.e. energy-conserving terms, and a non-conservative expression Q , that describes the non-energy conserving processes. We find that the Lagrangian \mathcal{L} can be written as [Jir06]

$$\mathcal{L} = -\frac{i}{2} \left(u \frac{\partial u^*}{\partial z} - u^* \frac{\partial u}{\partial z} \right) + D_2 \left| \frac{\partial u}{\partial t} \right|^2 + \frac{(\gamma + \alpha r)}{2} |u|^4 + (D_2 + \alpha g_\omega) \omega_0(t) |u|^2 - g_0 \alpha |u|^2; \quad (8.0.5)$$

and the non-conservative term Q is given by

$$Q = i \left(-g_0 + r |u|^2 + g_\omega \omega_0^2(t) + a_l - a_s \frac{\partial^2}{\partial t^2} \right) u. \quad (8.0.6)$$

The reduced Lagrangian is given by [Cer98]

$$\langle \mathcal{L} \rangle = \int_{-\infty}^{\infty} \mathcal{L} dt. \quad (8.0.7)$$

We can now write the Euler-Lagrange equations for the parameters $f = A, \Phi, b, T$ as

$$R_f = \frac{\partial \langle \mathcal{L} \rangle}{\partial f} - \frac{d}{dz} \frac{\partial \langle \mathcal{L} \rangle}{\partial \left(\frac{\partial f}{\partial z} \right)}. \quad (8.0.8)$$

Here R_f denotes the non-conservative forces given by

$$R_f = 2\mathcal{R} \left\{ Q \frac{\partial u^*}{\partial f} dt \right\}. \quad (8.0.9)$$

We now can insert the parameters A, Φ, b, T into the non-conservative term R_f and we get for $f = A$:

$$R_A = 2\mathcal{R} \int_{-\infty}^{\infty} \left[i \left(-g_0 + r |u|^2 + g_\omega \frac{\Delta \omega^2}{T_R^2} t^2 + a_l - a_s \frac{\partial^2}{\partial t^2} \right) u \right] \frac{\partial u^*}{\partial A} dt. \quad (8.0.10)$$

The chirped Gaussian ansatz is of the form

$$u(z, t) = A e^{i\Phi} e^{-t^2 \left(\frac{1}{2T^2} - ib \right)}; \quad (8.0.11)$$

so that we get for the second order partial derivative in R_A

$$\begin{aligned} \frac{\partial^2 u}{\partial t^2} &= \frac{\partial}{\partial t} \left(A e^{i\Phi} \left(-2t \left(\frac{1}{2T^2} - ib \right) \right) e^{-t^2 \left(\frac{1}{2T^2} - ib \right)} \right) = \\ &- 2A e^{i\Phi} \left(\frac{1}{2T^2} - ib \right) e^{-t^2 \left(\frac{1}{2T^2} - ib \right)} + A e^{i\Phi} \left[-2t \left(\frac{1}{2T^2} - ib \right) \right]^2 e^{-t^2 \left(\frac{1}{2T^2} - ib \right)}. \end{aligned} \quad (8.0.12)$$

We therefore have

$$\frac{\partial^2}{\partial t^2} \left(\frac{\partial u^*}{\partial A} \right) = -2e^{-i\Phi} \left(\frac{1}{2T^2} + ib \right) e^{-t^2 \left(\frac{1}{2T^2} + ib \right)} + e^{-i\Phi} \left[-2t \left(\frac{1}{2T^2} + ib \right) \right]^2 e^{-t^2 \left(\frac{1}{2T^2} + ib \right)}. \quad (8.0.13)$$

The other derivatives are given by

$$\frac{\partial u}{\partial z} = e^{i\Phi} e^{-t^2 \left(\frac{1}{2T^2} - ib \right)} \left(\frac{\partial A}{\partial z} + iA \frac{\partial \Phi}{\partial z} + \frac{At^2}{T^3} \frac{\partial T}{\partial z} + iAt^2 \frac{\partial b}{\partial z} \right); \quad (8.0.14)$$

$$\frac{\partial u^*}{\partial z} = e^{-i\Phi} e^{-t^2 \left(\frac{1}{2T^2} + ib \right)} \left(\frac{\partial A}{\partial z} - iA \frac{\partial \Phi}{\partial z} + \frac{At^2}{T^3} \frac{\partial T}{\partial z} - iAt^2 \frac{\partial b}{\partial z} \right); \quad (8.0.15)$$

$$-\frac{i}{2} \left(u \frac{\partial u^*}{\partial z} - u^* \frac{\partial u}{\partial z} \right) = \frac{i}{2} A e^{-\frac{t^2}{T^2}} \left(2iA \frac{\partial \Phi}{\partial z} + 2iAt^2 \frac{\partial b}{\partial z} \right); \quad (8.0.16)$$

$$\left| \frac{\partial u}{\partial t} \right|^2 = \left(\frac{t^2}{T^4} + 4b^2 t^2 \right) |u|^2. \quad (8.0.17)$$

We then can write the Lagrangian \mathcal{L} as

$$\mathcal{L} = -A^2 e^{-\frac{t^2}{T^2}} \left(\frac{\partial \Phi}{\partial z} + t^2 \frac{\partial b}{\partial z} \right) + D_2 \left(\frac{t^2}{T^4} + 4b^2 t^2 \right) e^{-\frac{t^2}{T^2}} + \frac{(\gamma + \alpha r)}{2} A^4 e^{-\frac{2t^2}{T^2}} + (D_2 + \alpha g_\omega) \frac{\Delta \omega^2}{T_R^2} t^2 A^2 e^{-\frac{t^2}{T^2}} - g_0 \alpha A^2 e^{-\frac{t^2}{T^2}}. \quad (8.0.18)$$

The reduced Lagrangian is then given by

$$\begin{aligned} \langle \mathcal{L} \rangle &= -A^2 \frac{\partial \Phi}{\partial z} \int_{-\infty}^{\infty} e^{-\frac{t^2}{T^2}} dt - A^2 \frac{\partial b}{\partial z} \int_{-\infty}^{\infty} t^2 e^{-\frac{t^2}{T^2}} dt + \frac{D_2 A^2}{T^4} \int_{-\infty}^{\infty} t^2 e^{-\frac{t^2}{T^2}} dt + \\ &4D_2 b^2 A^2 \int_{-\infty}^{\infty} t^2 e^{-\frac{t^2}{T^2}} dt + \frac{(\gamma + \alpha r) A^4}{2} \int_{-\infty}^{\infty} e^{-\frac{2t^2}{T^2}} dt + (D_2 + \alpha g_\omega) \frac{\Delta \omega^2}{T_R^2} A^2 \int_{-\infty}^{\infty} t^2 e^{-\frac{t^2}{T^2}} dt - g_0 \alpha A^2 \int_{-\infty}^{\infty} e^{-\frac{t^2}{T^2}} dt = \\ &A^2 \sqrt{\pi} \left(-\frac{\partial \Phi}{\partial z} T - \frac{T^3}{2} \frac{\partial b}{\partial z} + \frac{D_2}{2T} + 2D_2 b^2 T^3 + \frac{(\gamma + \alpha r) A^2 T}{2\sqrt{2}} + (D_2 + \alpha g_\omega) \frac{\Delta \omega^2 T^3}{2T_R^2} - g_0 \alpha T \right). \end{aligned} \quad (8.0.19)$$

We can now calculate R_A by inserting every term and calculating the infinite integral subsequently:

$$\begin{aligned}
R_A = & 2\mathcal{R} \, ig_0 A \int_{-\infty}^{\infty} e^{\frac{-t^2}{T^2}} dt - irA^3 \int_{-\infty}^{\infty} e^{\frac{-t^2}{T^2}} dt - ig_\omega \frac{\Delta\omega^2}{T_R^2} A \int_{-\infty}^{\infty} t^2 e^{\frac{-t^2}{T^2}} dt - ia_l A \int_{-\infty}^{\infty} e^{\frac{-t^2}{T^2}} dt \\
& - 2ia_s A \left(\frac{1}{2T^2} - ib \right) \int_{-\infty}^{\infty} e^{\frac{-t^2}{T^2}} dt + 4ia_s A \left(\frac{1}{4T^4} - \frac{ib}{T^2} - b^2 \right) \int_{-\infty}^{\infty} t^2 e^{\frac{-t^2}{T^2}} dt = \\
& - 2a_s Ab \sqrt{\pi} T + 2a_s Ab \sqrt{\pi} T = 0.
\end{aligned} \tag{8.0.20}$$

We can now apply the same principle for R_Φ :

$$\frac{\partial^2}{\partial t^2} 2iA^2 \left(\frac{1}{2T^2} - ib \right) e^{\frac{-t^2}{T^2}} - 4iA^2 t^2 \left(\frac{1}{4T^4} - \frac{ib}{T^2} - b^2 \right) e^{\frac{-t^2}{T^2}}; \tag{8.0.21}$$

so that we get for R_Φ

$$\begin{aligned}
R_\Phi = & 2\mathcal{R} \, g_0 A^2 \int_{-\infty}^{\infty} e^{\frac{-t^2}{T^2}} dt - irA^4 \int_{-\infty}^{\infty} e^{\frac{-2t^2}{T^2}} dt - g_\omega \frac{\Delta\omega^2}{T_R^2} A^2 \int_{-\infty}^{\infty} t^2 e^{\frac{-t^2}{T^2}} dt - a_l A^2 \int_{-\infty}^{\infty} e^{\frac{-t^2}{T^2}} dt \\
& - 2a_s A^2 \left(\frac{1}{2T^2} - ib \right) \int_{-\infty}^{\infty} e^{\frac{-t^2}{T^2}} dt + 4a_s A^2 \left(\frac{1}{4T^4} - \frac{ib}{T^2} - b^2 \right) \int_{-\infty}^{\infty} t^2 e^{\frac{-t^2}{T^2}} dt = \\
& 2g_0 A^2 \sqrt{\pi} T - 2rA^4 \sqrt{\frac{\pi}{2}} T - g_\omega \frac{\Delta\omega^2}{T_R^2} A^2 \sqrt{\pi} T^3 - 2a_l A^2 \sqrt{\pi} T - \frac{a_s A^2}{T} \sqrt{\pi} - 4a_s A^2 b^2 \sqrt{\pi} T^3.
\end{aligned} \tag{8.0.22}$$

The same principle is applied to b , and we get analogously

$$\begin{aligned}
R_b = & 2\mathcal{R} \, g_0 A^2 \int_{-\infty}^{\infty} t^2 e^{\frac{-t^2}{T^2}} dt - rA^4 \int_{-\infty}^{\infty} t^2 e^{\frac{-2t^2}{T^2}} dt - g_\omega \frac{\Delta\omega^2}{T_R^2} A^2 \int_{-\infty}^{\infty} t^4 e^{\frac{-t^2}{T^2}} dt - a_l A^2 \int_{-\infty}^{\infty} t^2 e^{\frac{-t^2}{T^2}} dt \\
& - 2a_s A^2 \left(\frac{1}{2T^2} - ib \right) \int_{-\infty}^{\infty} t^2 e^{\frac{-t^2}{T^2}} dt + 4a_s A^2 \left(\frac{1}{4T^4} - \frac{ib}{T^2} - b^2 \right) \int_{-\infty}^{\infty} t^4 e^{\frac{-t^2}{T^2}} dt = \\
& g_0 A^2 \sqrt{\pi} T^4 - rA^4 \sqrt{\frac{\pi}{2}} T^3 - g_\omega \frac{3\Delta\omega^2}{2T_R^2} A^2 \sqrt{\pi} T^5 - a_l A^2 \sqrt{\pi} T^3 - a_s A^2 \sqrt{\pi} T + a_s A^2 \frac{3}{2} \sqrt{\pi} T - 6a_s A^2 b^2 \sqrt{\pi} T^5.
\end{aligned} \tag{8.0.23}$$

For T we then get analogously

$$R_T = \dots = 4a_s A^2 b \sqrt{\pi}. \tag{8.0.24}$$

The conservative components can then be calculated by applying the Euler-Lagrange equation (8.0.8) for every parameter A, T, Φ, b on the reduced Lagrangian. We then find for R_A the following condition fulfilled:

$$R_A = \frac{\partial \langle \mathcal{L} \rangle}{\partial A} - \underbrace{\frac{d}{dz} \frac{\partial \langle \mathcal{L} \rangle}{\partial \left(\frac{\partial A}{\partial z} \right)}}_{=0} =$$

$$2A\sqrt{\pi} \left(-\frac{\partial \Phi}{\partial z} T - \frac{T^3}{2} \frac{\partial b}{\partial z} + \frac{D_2}{2T} + 2D_2 b^2 T^3 + \frac{(\gamma + \alpha r) A^2 T}{2\sqrt{2}} + (D_2 + \alpha g_\omega) \frac{\Delta \omega^2 T^3}{2T_R^2} - g_0 \alpha T \right). \quad (8.0.25)$$

Analogously we get for R_Φ that

$$R_\Phi = \underbrace{\frac{\partial \langle \mathcal{L} \rangle}{\partial \Phi}}_{=0} - \frac{d}{dz} \frac{\partial \langle \mathcal{L} \rangle}{\partial \left(\frac{\partial \Phi}{\partial z} \right)} = \frac{d}{dz} (A^2 T \sqrt{\pi}) =$$

$$2A\sqrt{\pi} T \frac{\partial A}{\partial z} + A^2 \sqrt{\pi} \frac{\partial T}{\partial z} \quad (8.0.26)$$

is fulfilled. For R_b we have

$$R_b = \frac{\partial \langle \mathcal{L} \rangle}{\partial b} - \frac{d}{dz} \frac{\partial \langle \mathcal{L} \rangle}{\partial \left(\frac{\partial b}{\partial z} \right)} = 4D_2 b T^3 A^2 \sqrt{\pi} - \frac{d}{dz} \left(-A^2 \frac{T^3}{2} \sqrt{\pi} \right) =$$

$$4D_2 b T^3 A^2 \sqrt{\pi} + A\sqrt{\pi} T^3 \frac{\partial A}{\partial z} + A^2 \sqrt{\pi} \frac{3T^2}{2} \frac{\partial T}{\partial z}. \quad (8.0.27)$$

The last condition that has to be fulfilled is

$$R_T = \frac{\partial \langle \mathcal{L} \rangle}{\partial T} - \underbrace{\frac{d}{dz} \frac{\partial \langle \mathcal{L} \rangle}{\partial \left(\frac{\partial T}{\partial z} \right)}}_{=0} =$$

$$A^2 \sqrt{\pi} \left(-\frac{\partial \Phi}{\partial z} - \frac{3T^2}{2} \frac{\partial b}{\partial z} - \frac{D_2}{2T^2} + 6D_2 b^2 T^2 + \frac{(\gamma + \alpha r) A^2}{2\sqrt{2}} + (D_2 + \alpha g_\omega) \frac{3\Delta \omega^2 T^2}{2T_R^2} - g_0 \alpha \right). \quad (8.0.28)$$

The four resulting equations then are:

$$2A\sqrt{\pi} \left(-\frac{\partial \Phi}{\partial z} - \frac{T^3}{2} \frac{\partial b}{\partial z} + \frac{D_2}{2T} + 2D_2 b^2 T^3 + \frac{(\gamma + \alpha r) A^2 T}{\sqrt{2}} + (D_2 + \alpha g_\omega) \frac{\Delta \omega^2 T^3}{2T_R^2} - g_0 \alpha T \right) = 0; \quad (8.0.29)$$

$$2A\sqrt{\pi} T \frac{\partial A}{\partial z} + A^2 \sqrt{\pi} \frac{\partial T}{\partial z} = 2g_0 A^2 \sqrt{\pi} T - 2r A^4 \sqrt{\frac{\pi}{2}} T - g_\omega \frac{\Delta \omega^2}{T_R^2} A^2 \sqrt{\pi} T^3 - 2a_l A^2 \sqrt{\pi} T - \frac{a_s A^2}{T} \sqrt{\pi} - 4a_s A^2 b^2 \sqrt{\pi} T^3; \quad (8.0.30)$$

$$4D_2bT^3A^2\sqrt{\pi} + A\sqrt{\pi}T^3\frac{\partial A}{\partial z} + A^2\sqrt{\pi}\frac{3T^2}{2}\frac{\partial T}{\partial z} =$$

$$g_0A^2\sqrt{\pi}T^3 - rA^4\sqrt{\frac{\pi}{2}}T^3 - g_\omega\frac{3\Delta\omega^2}{2T_R^2}A^2\sqrt{\pi}T^5 - a_lA^2\sqrt{\pi}T^3 + a_sA^2\frac{1}{2}\sqrt{\pi}T - 6a_sA^2b^2\sqrt{\pi}T^5; \quad (8.0.31)$$

$$A^2\sqrt{\pi}\left(-\frac{\partial\Phi}{\partial z} - \frac{3T^2}{2}\frac{\partial b}{\partial z} - \frac{D_2}{2T^2} + 6D_2b^2T^2 + \frac{(\gamma + \alpha r)A^2}{2\sqrt{2}} + (D_2 + \alpha g_\omega)\frac{3\Delta\omega^2T^2}{2T_R^2} - g_0\alpha\right) = -4a_sA^2b\sqrt{\pi}. \quad (8.0.32)$$

The equations of motion are now retrieved from these 4 equations. We get by multiplying (8.0.29) with A/T and subtracting from this two times (8.0.32) the equation of motion for b . The equation of motion for T is calculated by multiplying (8.0.30) with T^2 and subtracting two times (8.0.31). The equation of motion for A is calculated by multiplying (8.0.30) with T^2 and subtracting 2/3 times (8.0.31). The equation of motion for Φ is neglected here, because we are interested in the stationary state, where the phase is constant. A constant phase factor however does not contribute to the properties of the spectral power $|u(z, t)|^2$. The three resulting equations of motion for A , T and the chirp b are then given by:

$$\frac{\partial b}{\partial z} = -\frac{4a_sb}{T^2} + 4D_2b^2 - \frac{D_2}{T^4} - \frac{(\gamma + \alpha r)A^2\sqrt{2}}{4T^2} + \frac{(D_2 + \alpha g_\omega)\Delta\omega^2}{T_R^2}; \quad (8.0.33)$$

$$\frac{\partial T}{\partial z} = -4D_2bT - g_\omega\frac{\Delta\omega^2}{T_R^2}T^3 + \frac{a_s}{T} - 4a_sb^2T^3; \quad (8.0.34)$$

$$\frac{\partial A}{\partial z} = 2D_2bA + g_0A - \frac{rA^3}{\sqrt{2}} - a_lA - \frac{a_sA}{T^2}. \quad (8.0.35)$$

Appendix C: Method of moments

The method of moments [Jir11] uses generalized moments and relations between them in order to derive the evolution equations. For $u(z, t)$ from (7.1.2) we can introduce the energy Q_0 and the momentum P_0 as

$$Q_0 = \int_{-\infty}^{\infty} |u|^2 dt; \quad (8.0.36)$$

$$P_0 = \frac{1}{2} \int_{-\infty}^{\infty} \left(u \frac{\partial}{\partial t} u^* - u^* \frac{\partial}{\partial t} u \right). \quad (8.0.37)$$

Higher order generalized moments are given by

$$Q_1 = \int_{-\infty}^{\infty} t |u|^2 dt; \quad (8.0.38)$$

$$Q_l = \int_{-\infty}^{\infty} (t - t_0)^l |u|^2 dt; \quad (8.0.39)$$

$$P_l = \int_{-\infty}^{\infty} (t - t_0)^l \left(u^* \frac{\partial}{\partial t} u - u \frac{\partial}{\partial t} u^* \right). \quad (8.0.40)$$

with the condition that $l > 1$ for Q_l and $l > 0$ for P_l . Here, t_0 denotes the center of gravity. Based on the FDML evolution equation (7.2.1), we can define the dissipative, i.e non-energy conserving term as

$$R = \left(g_0 - r |u|^2 - g_\omega \frac{\Delta \omega^2}{T_R^2} t^2 - a_l + a_s \partial_t^2 \right). \quad (8.0.41)$$

It then follows that ([Jir11])

$$i \frac{\partial}{\partial z} |u|^2 + D_2 \frac{\partial}{\partial t} \left(u \frac{\partial}{\partial t} u^* - u^* \frac{\partial}{\partial t} u \right) = u^* R - u R^*. \quad (8.0.42)$$

Furthermore we get from $\mathcal{R} [(7.2.1) \cdot \frac{\partial}{\partial t} u^* - u^* \frac{\partial}{\partial t} (7.2.1)] = 0$:

$$\begin{aligned}
& \mathcal{R}\left\{D_2 \frac{\Delta\omega^2}{T_R^2} \left(t^2 u \frac{\partial}{\partial t} u^* - t^2 u^* \frac{\partial}{\partial t} u - 2t|u|^2 \right) - \alpha \left(g_0 - r|u|^2 - g_\omega \frac{\Delta\omega^2}{T_R^2} t^2 \right) u \frac{\partial}{\partial t} u^* + \right. \\
& \quad \left. \alpha u^* \left(g_0 \frac{\partial}{\partial t} u - r \frac{\partial}{\partial t} (u^* u) - g_\omega \frac{\Delta\omega^2}{T_R^2} (2tu + t^2 \frac{\partial}{\partial t} u) \right) \right\} = \\
& - 2t|u|^2 D_2 \frac{\Delta\omega^2}{T_R^2} - 2\alpha r|u|^2 \left(u^* \frac{\partial}{\partial t} u + u \frac{\partial}{\partial t} u^* \right) - 2t|u|^2 \alpha g_\omega \frac{\Delta\omega^2}{T_R^2} = 0. \tag{8.0.43}
\end{aligned}$$

$$\begin{aligned}
& \Rightarrow i \left(u \frac{\partial}{\partial t} u^* - u^* \frac{\partial}{\partial t} u \right) - 4D_2 \frac{\partial}{\partial t} \left| \frac{\partial}{\partial t} u \right|^2 + D_2 \frac{\partial^3}{\partial t^3} |u|^2 - \gamma \frac{\partial}{\partial t} |u|^4 - 2D_2 \frac{\Delta\omega^2}{T_R^2} t|u|^2 \\
& \quad - \alpha r|u|^2 \left(u^* \frac{\partial}{\partial t} u + u \frac{\partial}{\partial t} u^* \right) - 2t|u|^2 \alpha g_\omega \frac{\Delta\omega^2}{T_R^2} = \\
& \quad 2 \left(R^* \frac{\partial}{\partial t} u + R \frac{\partial}{\partial t} u^* \right) - \frac{\partial}{\partial t} (uR^* + u^*R). \tag{8.0.44}
\end{aligned}$$

We can now rewrite (8.0.42) using the generalized moments as

$$\frac{\partial}{\partial z} Q_0 = i \int_{-\infty}^{\infty} (uR^* - u^*R) dt; \tag{8.0.45}$$

$$\frac{\partial}{\partial z} Q_2 = 2iD_2 P_1 + i \int_{-\infty}^{\infty} t^2 (uR^* - u^*R) dt. \tag{8.0.46}$$

Rewriting (8.0.44) with the generalized moments yields

$$\begin{aligned}
\frac{\partial}{\partial z} P_1 &= i \int_{-\infty}^{\infty} \left(-4D_2 \left| \frac{\partial}{\partial t} u \right|^2 - \gamma |u|^4 \right) dt + 2iD_2 \frac{\Delta\omega^2}{T_R^2} \int_{-\infty}^{\infty} t^2 |u|^2 dt + \\
& 2i\alpha r \int_{-\infty}^{\infty} t|u|^2 \left(u^* \frac{\partial}{\partial t} u + u \frac{\partial}{\partial t} u^* \right) dt + 2i\alpha g_\omega \frac{\Delta\omega^2}{T_R^2} \left(\int_{-\infty}^{\infty} t^2 |u|^2 dt \right) + \\
& 2i \int_{-\infty}^{\infty} t \left(R^* \frac{\partial}{\partial t} u + R \frac{\partial}{\partial t} u^* \right) dt + i \int_{-\infty}^{\infty} (uR^* + u^*R) dt. \tag{8.0.47}
\end{aligned}$$

We then get from (8.0.45) the condition

$$\frac{\partial}{\partial z} Q_0 = 2AT\sqrt{\pi} \frac{\partial A}{\partial z} + A^2 \sqrt{\pi} \frac{T}{\partial z}. \tag{8.0.48}$$

The integral term becomes

$$i \int_{-\infty}^{\infty} (uR^* - u^*R) dt = \dots =$$

$$2g_0A^2\sqrt{\pi}T - 2rA^4\sqrt{\frac{\pi}{2}} - g_\omega\frac{\Delta\omega^2}{T_R^2}A^2\sqrt{\pi}T^3 - a_lA^2\sqrt{\pi}T - \frac{a_sA^2}{T}\sqrt{\pi} - 4a_sA^2b^2\sqrt{\pi}T^3. \quad (8.0.49)$$

$$\Rightarrow 2AT\frac{\partial A}{\partial z} + A^2\frac{\partial T}{\partial z} = 2g_0A^2T - 2rA^4\frac{T}{2} - g_\omega\frac{\Delta\omega^2}{T_R^2}A^2T^3 - 2a_lA^2T - \frac{a_sA^2}{T} - 4a_sA^2b^2T. \quad (8.0.50)$$

From (8.0.46) it follows that

$$\frac{\partial}{\partial z}Q_2 = \frac{\partial A}{\partial z}\left(A^2T^3\frac{\sqrt{2}}{2}\right) = AT^3\sqrt{\pi}\frac{\partial A}{\partial z} + \frac{3}{2}A^2T^2\frac{\partial T}{\partial z}. \quad (8.0.51)$$

Furthermore we have

$$\begin{aligned} 2iD_2P_1 &= 2iD_2\int_{-\infty}^{\infty}t\left(u^*\frac{\partial}{\partial t}u - u\frac{\partial}{\partial t}u^*\right)dt = \\ 2iD_2A^2\int_{-\infty}^{\infty}t\left[-2t\left(\frac{1}{2T^2} - ib\right)e^{\frac{-t^2}{T^2}} + 2t\left(\frac{1}{2T^2} + ib\right)e^{\frac{-t^2}{T^2}}\right]dt &= \\ -4D_2bA^2T^3\sqrt{\pi}. \end{aligned} \quad (8.0.52)$$

The integral term yields

$$i\int_{-\infty}^{\infty}t^2(uR^* - u^*R)dt = \dots =$$

$$g_0A^2\sqrt{\pi}T^3 - rA^4\sqrt{\frac{\pi}{2}}T^3 - g_\omega\frac{3\Delta\omega^2}{2T_R^2}A^2\sqrt{\pi}T^5 - a_lA^2\sqrt{\pi}T^3 - a_sA^2\sqrt{\pi}T + a_sA^2\frac{3}{2}\sqrt{\pi}T - 6a_sA^2b^2\sqrt{\pi}T^5. \quad (8.0.53)$$

Then we can write the second condition as

$$AT^3\frac{\partial A}{\partial z} + \frac{3}{2}A^2T^2\frac{\partial T}{\partial z} =$$

$$g_0A^2T^3 - rA^4\sqrt{\frac{1}{2}}T^3 - g_\omega\frac{3\Delta\omega^2}{2T_R^2}A^2T^5 - a_lA^2T^3 - a_sA^2T + a_sA^2\frac{3}{2}T - 6a_sA^2b^2T^5. \quad (8.0.54)$$

From (8.0.47) it follows that

$$\frac{\partial}{\partial z}P_1 = \frac{\partial}{\partial z}\int_{-\infty}^{\infty}t\left(u^*\frac{\partial}{\partial t}u - u\frac{\partial}{\partial t}u^*\right)dt =$$

$$\begin{aligned} \frac{\partial}{\partial t} \int_{-\infty}^{\infty} t \left[-2t \left(\frac{1}{2T^2} - ib \right) A^2 e^{\frac{-t^2}{T^2}} + 2t \left(\frac{1}{2T^2} + ib \right) A^2 e^{\frac{-t^2}{T^2}} \right] dt = \\ 2i\sqrt{\pi} \left(2AT^3 b \frac{\partial A}{\partial z} + 3bA^2 T^2 \frac{\partial T}{\partial z} + A^2 T^3 \frac{\partial b}{\partial z} \right); \end{aligned} \quad (8.0.55)$$

$$\begin{aligned} i \int_{-\infty}^{\infty} \left(-4D_2 \left| \frac{\partial}{\partial t} u \right|^2 - \gamma |u|^4 \right) dt = i \int_{-\infty}^{\infty} \left[-4D_2 \left(\frac{t^2}{T^4} + 4b^2 t^2 \right) A^2 e^{\frac{-t^2}{T^2}} - \gamma A^4 e^{\frac{-2t^2}{T^2}} \right] dt = \\ i \left(-2A^2 \frac{D_2}{T} \sqrt{\pi} - 8A^2 b^2 D_2 \sqrt{\pi} T^3 - \gamma A^4 \sqrt{\frac{\pi}{2}} T \right). \end{aligned} \quad (8.0.56)$$

Analogously we have in (8.0.47) that

$$\begin{aligned} 2i \int_{-\infty}^{\infty} t \left(R^* \frac{\partial}{\partial t} u + R \frac{\partial}{\partial t} u^* \right) dt = \dots = \\ -8ia_s b A^2 \sqrt{\pi} T + 4ib \left(g_0 A^2 \sqrt{\pi} T^3 - r A^4 \sqrt{\frac{\pi}{2}} T^3 - g_\omega \frac{3\Delta\omega^2}{2T_R^2} A^2 \sqrt{\pi} T^5 \right. \\ \left. - a_l A^2 \sqrt{\pi} T^3 - a_s A^2 \sqrt{\pi} T + a_s A^2 \frac{3}{2} \sqrt{\pi} T - 6a_s A^2 b^2 \sqrt{\pi} T^5 \right). \end{aligned} \quad (8.0.57)$$

From symmetry it follows that the term

$$i \int_{-\infty}^{\infty} (uR^* + u^*R) dt$$

from (8.0.47) vanishes. The other terms are:

$$2iD_2 \frac{\Delta\omega^2}{T_R^2} \int_{-\infty}^{\infty} t^2 |u|^2 dt = iD_2 \frac{\Delta\omega^2}{T_R^2} A^2 T^3 \sqrt{\pi}; \quad (8.0.58)$$

$$2i\alpha r \int_{-\infty}^{\infty} |u|^2 t \left(u^* \frac{\partial}{\partial t} u + u \frac{\partial}{\partial t} u^* \right) dt = \dots = -\frac{1}{2} i\alpha A^4 r T \sqrt{2\pi}; \quad (8.0.59)$$

$$i\alpha g_\omega \frac{\Delta\omega^2}{T_R^2} \left(2 \int_{-\infty}^{\infty} t^2 |u|^2 dt \right) = i\alpha g_\omega \frac{\Delta\omega^2}{T_R^2} A^2 T^3 \sqrt{\pi}. \quad (8.0.60)$$

All the terms inserted into (8.0.47) yield the equation

$$2i \left(2AT^3 b \frac{\partial A}{\partial z} + 3bA^2 T^2 \frac{\partial T}{\partial z} + A^2 T^3 \frac{\partial b}{\partial z} \right) = i \left(-2A^2 \frac{D_2}{T} - 8A^2 b^2 D_2 T^3 - \gamma A^4 \sqrt{\frac{1}{2}} T \right) +$$

$$D_2 \frac{\Delta\omega^2}{T_R^2} A^2 T^3 - \frac{1}{2} i \alpha A^4 r T \sqrt{2} + i \alpha g_\omega \frac{\Delta\omega^2}{T_R^2} A^2 T^3. \quad (8.0.61)$$

From this it follows together with (8.0.54) that

$$\frac{\partial b}{\partial z} = -\frac{4a_s b}{T^2} + 4D_2 b^2 - \frac{D_2}{T^4} - \frac{(\gamma + \alpha r) A^2 \sqrt{2}}{4T^2} + \frac{(D_2 + \alpha g_\omega) \Delta\omega^2}{T_R^2}. \quad (8.0.62)$$

From (8.0.50) and (8.0.54) it follows the relations for T and A :

$$\frac{\partial T}{\partial z} = -4D_2 b T - g_\omega \frac{\Delta\omega^2}{T_R^2} T^3 + \frac{a_s}{T} - 4a_s b^2 T^3; \quad (8.0.63)$$

$$\frac{\partial A}{\partial z} = 2D_2 b A + g_0 A - \frac{r A^3}{\sqrt{2}} - a_l A - \frac{a_s A}{T^2}. \quad (8.0.64)$$

Comparison of (8.0.62)-(8.0.64) with (8.0.33),(8.0.34) and (8.0.35) shows that the resulting equations of motion are the same. Therefore the method of moments is analogous to the variational principle and results in the same equations of motion.

Appendix D: Laser parameter terms

The coefficients $a, b, c, d, e, f, g, h, k, l$ are given by:

$$a = 2\alpha a_s^3 D_2 \Delta \omega^2 T_R^2;$$

$$b = 2a_s^2 D_2^3 \Delta \omega^2 T_R^2;$$

$$c = 2\alpha a_s D_2^3 \Delta \omega^3 \Delta \omega^2 T_R^2;$$

$$d = 2D_2^4 \Delta \omega^2 T_R^2;$$

$$e = 2a_s^3 \Delta \omega^2 g_\omega T_R^2;$$

$$f = 2\alpha a_s^2 D_2 \Delta \omega^2 g_\omega T_R^2;$$

$$g = 2a_s D_2^2 \Delta \omega^2 g_\omega T_R^2;$$

$$\begin{aligned} k = & 2T_R^2 (a_s^6 D_2^2 \Delta \omega^4 + \alpha^2 a_s^6 D_2^2 \Delta \omega^4 + \\ & 3a_s^4 D_2^4 \Delta \omega^4 + 3\alpha^2 a_s^2 D_2^6 \Delta \omega^4 + D_2^8 \Delta \omega^4 T_R^4 + \alpha^2 D_2^8 \Delta \omega^4 + \\ & a_s^6 \Delta \omega^4 g_\omega^2 + \alpha^2 a_s^6 \Delta \omega^4 g_\omega^2 + 3a_s^4 D_2^2 \Delta \omega^4 g_\omega^2 + 3\alpha^2 a_s^4 D_2^2 \Delta \omega^4 g_\omega^2 + \\ & 3a_s^2 D_2^4 \Delta \omega^4 g_\omega^2 + \\ & 3\alpha^2 a_s^2 D_2^4 \Delta \omega^4 g_\omega^2 + \\ & D_2^6 \Delta \omega^4 g_\omega^2 + \alpha^2 D_2^6 \Delta \omega^4 g_{\omega^2})^{1/2}. \end{aligned}$$

$$\begin{aligned} l = & a_s^2 D_2^2 \Delta \omega^4 + 2\alpha a_s D_2^3 \Delta \omega^4 + \alpha^2 D_2^4 \Delta \omega^4 + \\ & 2\alpha a_s^2 D_2 \Delta \omega^4 g_\omega - 2a_s D_2^2 \Delta \omega^4 g_\omega + 2\alpha^2 a_s D_2^2 \Delta \omega^4 g_\omega - \\ & 2\alpha D_2^3 \Delta \omega^4 g_\omega + \alpha^2 a_s^2 \Delta \omega^4 g_\omega^2 - 2\alpha a_s D_2 \Delta \omega^4 g_\omega^2 + D_2^2 \Delta \omega^4 g_\omega^2. \end{aligned}$$

The chirp b is given by

$$b = \frac{T^2(a_s D_2 \Delta\omega^2 + \alpha D_2^2 \Delta\omega^2 + \alpha a_s \Delta\omega^2 g_\omega - D_2 \Delta\omega^2 g_\omega)}{4(a_s^2 + D_2^2)T_R^2}$$

Nomenclature

Acronyms

ASE	Amplified spontaneous emission
BFP-TF	Bulk Fabry-Perot tunable filter
CIR	Optical circulator
cw	Continuous wave
DCF	Dispersion compensation fiber
EDFA	Erbium doped fiber amplifier
EOM	Electro optical modulator
FC	Fused fiber coupler
FDML	Fourier domain mode-locked
FFP-TF	Fast Fabry-Perot tunable filter
FFTW	Fastest Fourier transform in the west
FRM	Faraday rotating mirror
FWHM	Full width at half maximum
ISO	Optical isolator
NSE	Nonlinear Schrödinger equation
OCT	Optical coherence tomography
PBS	Polarizing beam splitter
PC	Polarization controller
PM	Polarization maintaining
SOA	Solid state optical amplifier
SMF	Single mode fiber
SPM	Self phase modulation

Special symbols

$\frac{\partial}{\partial t}$	partial derivative with respect to t
$\frac{\partial}{\partial z}$	partial derivative with respect to z
∇	nabla operator
$\mathcal{R}\{u\}$	real part of u
$\mathcal{I}\{u\}$	imaginary part of u
u^*	complex conjugate of u

Calligraphic symbols

\mathcal{F}	Fourier transform
\mathcal{F}^{-1}	inverse Fourier transform
\mathcal{L}	Lagrangian
$\langle \mathcal{L} \rangle$	reduced Lagrangian

Greek symbols

α	Henry factor/linewidth-enhancement
γ	self-phase modulation coefficient
δ	detuning of the sweep filter with respect to the light field
Δ	Lorentzian angular frequency width
Δf	frequency tuning range
$\Delta\omega$	angular frequency tuning range
$\Delta\omega_g$	FWHM linewidth of gain transition
$\Delta\omega_l$	FWHM linewidth of optical transition
$\Delta\nu$	frequency spacing of cavity modes
ϵ_0	permittivity constant
κ	complex phase parameter in the chirped Gaussian ansatz
λ	wavelength
μ_0	permeability constant
ρ	charge density
τ_c	carrier lifetime
$\Phi(z)$	spatial phase factor, analogous to κ
$\Phi(\omega)$	spectral phase
$\Phi(\omega)_{avg}$	averaged spectral phase

χ	susceptibility
χ_{mn}	susceptibility tensor
ω	circular frequency
Ω	circular frequency in Taylor expansion
ω_c	center angular frequency
ω_s	angular sweep frequency
$\omega_0(t)$	sweep filter drive function

Latin symbols

$A(t)$	space independent complex field envelope in stationary frame
$\tilde{A}(\omega)$	space independent complex field envelope in stationary frame in Fourier domain
$A(z, t)$	space dependent complex field envelope in stationary frame
$\tilde{A}(z, \omega)$	space dependent complex field envelope in stationary frame in Fourier domain
a_l	fiber loss
a_s	sweep filter loss
b	frequency chirp
\vec{B}	magnetic flux
c_0	velocity of light in vacuum
c	velocity of light in matter
\vec{D}	dielectric flux
D_2	second order dispersion coefficient
D_3	third order dispersion coefficient
D_m	dispersion coefficient of order m
$D(\Omega)$	dispersion function
\vec{E}	electric field
$\text{erf}(z)$	error function
$\text{erfi}(z)$	imaginary error function
\hat{e}_z	unity vector in z-direction
G	amplitude gain
G_0	frequency dependent peak gain
\vec{H}	magnetic field
\vec{j}	current density
\vec{k}_c	carrier wavevector
$\vec{k}(\omega)$	angular wavevector
L	fiber length

\hat{L}	linear operator in NSE
\vec{M}	magnetization
\hat{N}	nonlinear operator in NSE
n	refractive index
$n_{2,L}$	intensity dependent refractive index
\vec{P}	polarization
P_0	peak power
$P_{av}(t)$	moving average of optical power
P_f	spectral power density
P_l	generalized moment of momentum
P_{sat}	saturation power
$P(t)$	optical power
r	nonlinearity factor in linearized gain ansatz
R_f	non-conservative forces
t_{limit}	time-bandwidth limit
T_R	total roundtrip time of the light field in the laser
Q	non-conservative term in variational ansatz
Q_l	generalized moment of energy
$u[0]$	real part of complex FFTW field
$u[1]$	imaginary part of complex FFTW field
u_{ch}	frequency chirped Gaussian field envelope
u_{comp}	compressed field envelope
$\tilde{U}(k_x)$	generalized complex field envelope in wavevector space
$u(t)$	space independent complex field envelope in swept filter reference frame, time domain
$\tilde{u}(\omega)$	space independent complex field envelope in swept filter reference frame, Fourier domain
$\tilde{U}(\omega)$	generalized space independent complex field envelope in Fourier domain
$U(x)$	generalized complex field envelope in position domain
$u(z, t)$	space dependent complex field envelope in swept filter reference frame, time domain
$\tilde{u}(z, \omega)$	space dependent complex field envelope in swept filter reference frame, Fourier domain
v_{ph}	group velocity

List of Figures

3.1.1 Image of a human finger "in vivo". The image resolution is 4096x1024 pixels which is acquired in 0.097 s. This corresponds to 42000 axial scans per second and 10 frames per second. Image courtesy of Robert Huber (Ludwig-Maximilians Universität München).	25
3.1.2 Examples of 3D images acquired by an FDML OCT setup as in [Wie10] with different setups. The left image is an OCT image of the human finger near the nail acquired at a 1 MHz scanning rate. The image in the middle is at a scanning range of 2.6 MHz. The right image is taken using a setup that operates at 5.2 MHz scanning rate. Images courtesy of Robert Huber (Ludwig-Maximilians Universität München)	26
3.1.3 The top image shows a rendering of the 3D data set acquired by the FDML setup in [Wie10]. The data set consists of 1900x1900 axial scans and an ultra-wide imaging field of 70°. The middle pictures show a reconstruction of the macula in front view. The second last row shows a cross-sectional image through the macula and the optics disc. The bottom row shows enlarged images of the macula and the optical nerve. Images courtesy of Robert Huber (Ludwig-Maximilians Universität München).	27
3.2.1 Experimental setup of FDML laser. The central elements are the tunable Fabry-Perot narrow bandpass or sweep filter (FFP-TF), the solid state optical amplifier (SOA) as a gain medium, and the 3.4 km single mode fiber (SMF) delay line. This laser has a center wavelength of 1320 nm, a sweep frequency of 57 kHz, and a tuning range of 105 nm.	28
3.2.2 The filter is driven with an angular frequency of $\omega_0(t) = -\frac{\Delta\omega}{2}\cos(\omega_s t)$, with ω_s being the sweep frequency of 57 kHz. The center frequency of the sweep is 1320 nm.	29
3.4.1 The split-step Fourier method splits a nonlinear partial differential equation into linear and nonlinear parts, which are treated consecutively in the time and in the frequency domain. The step size is h, while L and N denote the linear and nonlinear part of the differential equation, in our case 3.4.1.	32
3.4.2 (a) Experimentally measured SOA power gain (linear scale) as a function of the optical frequency for different values of the incident optical power. (b) Experimentally measured overall cavity power loss (linear scale) as a function of the optical frequency. The sweep filter has been tuned to maximum transmission at each measured frequency.	33

3.4.3 Simulated power output for an FDML laser centered at 1320 nm with a sweep range of 105 nm, a roundtrip time of 17.32 μ s, and a filter drive function according to Fig. 3.2.2.	34
4.1.1 The experimental setup shown in (a) is the same as in Fig. 3.2.1, and in (b) the measurement of the instantaneous lineshape is performed. The function generator drives the sweep filter and is linked to a pulse generator, which in turn is coupled to the electro-optical modulator (EOM). The EOM takes the outcoupled light and feeds it then into the optical spectrum analyzer.	38
4.3.1 Experimental (red) and simulated (blue) instantaneous power spectra after the SOA at (a) 1.3 μ s and (b) 3.3 μ s for no detuning.	40
4.3.2 Theoretical (blue) and experimental (red) power spectra at 7.3 μ s for (a) no detuning, for (b) a detuning of -2 Hz and for (c) a detuning of +2 Hz.	41
4.3.3 (a) Simulated instantaneous power spectrum for $\alpha = 5$ (red) and $\alpha = 0$ (blue), the sweep filter transmission function is drawn in black. (b) The instantaneous power spectrum for $\alpha = 5$ (red) and $\alpha = 0$ (blue) but without ASE.	42
5.0.1 Instantaneous power spectrum at $t=5.3 \mu$ s after the SOA for the simulation with gating considered (blue dotted curve), for the simulation without gating (green dotted curve), and as obtained from experiment (dash-dotted curve). The sweep filter transmission (solid curve) is shown for comparison.	47
5.1.1 Simulated temporal evolution of the instantaneous power spectrum after the SOA over a full roundtrip without gating included.	47
5.1.2 (a) Gaussian input pulse and the corresponding averaged power obtained from (??) as a function of time. (b) Power spectrum of the Gaussian input pulse and output power spectrum after the gain medium.	49
5.1.3 Temporal dependence of the frequency shift caused by the fiber dispersion.	50
5.1.4 Power spectrum of the Gaussian input pulse and output power spectrum after self-phase modulation.	51
5.1.5 Power spectrum of the Gaussian input pulse and output power spectrum after the sweep filter. The sweep filter transmission (dotted curve) is shown for comparison.	52
5.1.6 Simulation results for the temporal evolution of (a) mean frequency and (b) linewidth.	54
5.1.7 Simulated and measured temporal evolution of the linewidth. Shown are simulation results with gating considered (dashed curve) and without gating (dotted curve), as well as experimental data (crosses).	55
5.1.8 Experimental (dashed) and theoretical (dotted) instantaneous power spectra after (a) the SOA, (b) the SMF and (c) the sweep filter at $t=5.3 \mu$ s.	56

6.3.1 Fourier limited pulse compression in an FDML laser for the example of a linear ramp. The extracted FWHM pulse length is 49 fs, for the laser parameters of the laser setup explained in chapter 2.2.	63
6.4.1 (a) The FDML laser setup operated at 1560 nm center wavelength and a sweep frequency of 390 kHz. The post-amplification devices are used to amplify the output signal. The dispersion compensation fiber (DCF) is used for temporal compression and the detection system detects the short pulses. The SOA denotes the semiconductor optical amplifier, ISO denotes the optical isolator, PC is the polarization controller, FRM is the Faraday rotation mirror, CIR denotes the optical circulator and FFP-TF denotes the fast Fabry-Perot tunable filter, built by Robert Hubers group at LMU München. (b) Typical wavelength over time characteristics of the FDML output, including the part used for temporal compression.	64
6.5.1 (a) The cut-out of the power over time, with a duration of 20 ns. (b) The spectral power density of the cut-out in the frequency domain. (c) The spectral phase distribution. The phase $\Phi(\omega)$ and the averaged phase $\Phi(\omega)_{avg}$, which is then subtracted, are in this plot indistinguishable, because the difference is only very small. (d) The compressed pulse with a length of 84 ps. The finite resolution of the sampling oscilloscope is emulated by the smoothing of the pulse. This smoothing lengthens the pulse by 45 ps. This effect is then subtracted, which results in the 84 ps pulse length.	69
6.5.2 (a) Pulse with a length of 68 ps for 1x DCF and $\Delta\lambda \approx 6$ nm. (b) The dependency of the pulse length from detuning. The asymmetry is caused by the sampling oscilloscope. . . .	72
6.5.3 (a) The simulation data from Table 6.2 together with the experimental results [Eig11B]. As can be seen, the pulse length decreases with smaller filter bandwidths, reaching its minimum at 10 pm. The experimental data also shows that the pulse length decreases, which is measured for two different filter bandwidths. (b) The simulation data from Table 6.1 together with the experimental results. As can be seen, the general behaviour that the pulse length increases with higher detuning is also present in theory. In theory, the shortest pulse length is achieved at -0.4 Hz detuning with 83.84 ps. This is only slightly higher than the experimental result of 68 ps.	72
7.2.1 The spatial evolution of the amplitude is shown here. It can be seen that after about 10^4 m, which corresponds to about three roundtrips, the power does not change any more. It converges towards a value of 34.6 mW.	79
7.2.2 Here, the spatial evolution of the chirp is shown. It can be seen that the chirp first decreases with increasing z, then reaches a minimum after about $6 \cdot 10^3$ m, then rises again and reaches convergence towards a value of $1.649 \cdot 10^9$ s ⁻² after a distance of about $1.4 \cdot 10^4$ m, which corresponds to about four roundtrips.	79

7.2.3 This is a zoomed in portion of the chirp evolution, in order to better illustrate the point where convergence is reached.	80
7.2.4 The spatial evolution of the pulse duration. It can be seen that after a few meters, the pulse duration has already converged towards a value of $19.373 \mu s$	80
7.3.1 Here, the chirped nature of the field (red curve) has been additionally drawn together with the power output (blue curve).	82
7.3.2 The FDML power output (blue curve) and the chirped field (red curve) for $\Delta\omega = 2 \cdot \Delta\omega_0$. This output fits the observed output better, in that the chirp is higher and the variation of the pulse power by a factor of ≈ 2 is also present, as seen in 3.4.3.	83

List of Tables

6.1	The results of the pulse lengths from the simulation in dependence of the detuning. As can be seen, the pulse length has the tendency to become larger for larger detunings, with the shortest pulse at -0.4 Hz. It is noteworthy that the shortest pulse is not located at 0 Hz detuning, but the zero detuning point in the experiment does not necessarily have to coincide with the zero detuning point in the simulation, as explained in chapter 6.5.2.7.	70
6.2	The pulse length in ps in dependency of the detuning and the sweep filter bandwidth. The dashes mean that these points have not been simulated. As can be seen, the detuning dependency decreases with smaller filter bandwidths. It is also noteworthy that below 10 pm filter bandwidth, the pulse length begins increasing again, and between 5 pm and 2 pm there is a huge increase, resulting in non-existent compression at 1 pm bandwidth. In this case, there is no compression possible and therefore the pulse length equals the time length of the cut-out window. The pulse length decreases until this point with smaller filter bandwidths, reaching the smallest value at 10 pm filter bandwidth and -0.2 Hz detuning. Because the detuning is symmetric with respect to the pulse lengths, only the negative detuning has been simulated.	70
6.3	The pulse length in ps for perfect dispersion compensation (0% remaining dispersion in the cavity) in dependency of the detuning and the sweep filter bandwidth. It is noteworthy that now the shortest pulse is at 0 Hz detuning with a very short pulse length of 11.07 ps even at the standard filter bandwidth of 310 pm. For smaller filter bandwidths of 5 pm and 1 pm, very short pulses of several hundred femtoseconds can be achieved, which is in the order of the time bandwidth product of 100 fs.	71
7.1	The laser parameters for the experimental setup as in Fig. 3.2.1 and Fig. 4.1.1.	81

Bibliography

- [Abr70] M. Abramowitz, I. A. Stegun, "Handbook of Mathematical Functions with Formulas, Graphs, and Mathematical Tables", Dover Publications, New York, Ninth printing (1970).
- [Adl11] D. C. Adler, W. Wieser, F. Trepanier, *et al.*, "Extended coherence length Fourier domain mode locked lasers at 1310 nm", *Opt. Express*, **19** (21), 20930-20939 (2011).
- [Agr06] G. P. Agrawal, "Nonlinear Fiber Optics", 4th edn., Academic Press, New York (2006).
- [Ant96] Philippe Antoine, Anne L'Huillier, and Maciej Lewenstein, "Attosecond Pulse Trains Using HighOrder Harmonics", *Phys. Rev. Lett.* **77**, 12341237 (1996).
- [Ara96] S. Arahira, Y. Matsui, Y. Ogawa, "Mode-locking at very high repetition rates more than terahertz in passively mode-locked distributed-Bragg-reflector laser diodes", *IEEE J. Quantum Electron.* **327**, 1211 - 1224 (1996).
- [Arm99] J. W. Armstrong, F. B. Estabrook, and M. Tinto, "Time-Delay Interferometry for Space-based Gravitational Wave Searches" *Ap. J.* **527**, 814 (1999).
- [Arn89] V. I. Arnold, "Mathematical Methods of Classical Mechanics", 2nd ed., Springer Verlag, 5961 (1989).
- [Ath81] P. D. Atherton, N. K. Reay, J. Ring *et al.*, "Tunable Fabry-Perot filters", *Opt. Eng.*, **20**, 806-814 (1981).
- [Beh86] G. Beheim and K. Fritsch, "Range finding using frequency-modulated laser diode", *Appl. Opt.* **25** (9), 1439 (1986).
- [Ben98] P. Bender, K. Danzmann, and the LISA Study Team, "Laser Interferometer Space Antenna for the Detection of Gravitational Waves", Pre-Phase, A Report, MPQ233, Max-Planck-Institut für Quantenoptik (1998).
- [Bie09] B. R. Biedermann, "Fourierdomänen modengekoppelte Laser: Aufklärung der Funktionsweise und Erschließung neuer Anwendungsbereiche", PhD Thesis, LMU München (2010).
- [Bil06] A. Bilenca, S. H. Yun, G. J. Tearney, and B. E. Bouma, "Numerical study of wavelength-swept semiconductor ring lasers: the role of refractive-index nonlinearities in semiconductor optical amplifiers and implications for biomedical imaging applications," *Opt. Lett.* **31**, 760-762 (2006).

- [Boh06] C. Bohling, D. Scheel, K. Hohmann *et al.*, "Fiber-optic laser sensor for mine detection and verification," *Appl. Opt.* **45**, 3817-3825 (2006).
- [Bor06] R. Bornemann, U. Lemmer, and E. Thiel, "Continuous-wave solid-state dye laser", *Opt. Lett.* **31**(11), 1669 (2006).
- [Boy03] R. W. Boyd, "Nonlinear Optics", Academic Press, New York (2003).
- [Bur73] C. A. Burrus and J. Stone, "Nd³⁺ doped SiO₂ lasers in an end-pumped fiber geometry", *Appl. Phys. Lett.* **23**(7), 388 (1973).
- [Bur07] B. Burgoyne, N. Godbout, and S. Lacroix, "Nonlinear pulse propagation in optical fibers using second order moments", *Opt. Express* **15**, 10075-10090 (2007).
- [Cas00] D. Cassioli, S. Scotti, and A. Mecozzi, "A time-domain computer simulator of the nonlinear response of semiconductor optical amplifiers," *IEEE J. Quantum Electron.* **36**, 1072-1080 (2000).
- [Cer98] S. Chavez-Cerda, Solange B. Cavalcanti and J. M. Hickmann, "A Variational Approach of Non-linear Dissipative Pulse Propagation", *European Physical Journal D* **1**, 313 (1998).
- [Chi96] Y. T. Chieng, "Derivation of the mode build-up time of tunable fiber lasers", *IEEE Phot. Tech. Lett.* **8**(2) (1996).
- [Clu62] F.J. McClung and R.W. Hellwarth, "Giant optical pulsations from ruby", *J. App. Phys.* **33** (3), 828-829 (1962).
- [Did01] S. A. Diddams, Th. Udem, J. C. Bergquist, *et al.* "An optical clock based on a single trapped ¹⁹⁹Hg⁺ ion", *Science* **293**, 825 (2001).
- [Der08] D. Derickson, M. Bernacil, A. DeKelaita, B. Maher, and S. O'Connor, "SGDBR single-chip wavelength tunable lasers for swept source OCT," *Proc. SPIE* 6847, 68472P (2008).
- [Don58] I. Donald, J. MacVicar, T. G. Brown, "Investigation of abdominal masses by pulsed ultrasound", *Lancet* **1** (7032), 118895 (1958).
- [DrJ05] C. Jirauschek, "Few-Cycle Laser Dynamics and Carrier-Envelope Phase Detection", Cuvillier Verlag, Göttingen (2005).
- [Eig09] C. M. Eigenwillig, B. R. Biedermann, W. Wieser, and R. Huber, "Wavelength swept amplified spontaneous emission source," *Opt. Express* **17**(21), 18794-18807 (2009).
- [Eig09] C. M Eigenwillig, T. Klein, W. Wieser, B. R Biedermann, and R. Huber, "Wavelength swept amplified spontaneous emission source for high speed retinal optical coherence tomography at 1060 nm," *J. Biophotonics* **4**(7-8), 552-558 (2011).
- [Eig11] C. M Eigenwillig, T. Klein, W. Wieser, B. R Biedermann, and R. Huber, "Wavelength swept amplified spontaneous emission source for high speed retinal optical coherence tomography at 1060 nm," *J. Biophotonics* **4**(7-8), 552-558 (2011).

- [Eig11B] C. Eigenwillig, S. Todor, W. Wieser, B. Biedermann, T. Klein, C. Jirauschek, and R. Huber, "Picosecond pulses from an FDML laser," Conference on Lasers and Electro-Optics, (Optical Society of America, 2012).
- [Ell01] R. Ell, U. Morgner, F. X. Kärtner, J. G. Fujimoto, E. P. Ippen, V. Scheuer, G. Angelow, T. Tschudi, M. J. Lederer, A. Boiko, and B. Luther-Davies, "Generation of 5-fs pulses and octave-spanning spectra directly from a Ti:sapphire laser", *Opt. Lett.* **26** (6), 373 (2001).
- [Fer93] A.F. Fercher, C.K. Hitzenberger, W. Drexler et al., "In Vivo Optical Coherence Tomography," *Am. J. Ophthalmol.*, **116** (1), 113-114 (1993).
- [Fri05] M. Frigo, S. G. Johnson, "The design and implementation of FFTW3", *Proceedings of the IEEE* **93** (2), 216231 (2005).
- [Gar02] A. Garnache, S. Hoogland, A. C. Tropper, I. Sagnes, G. Saint-Girons, J. S. Roberts, "Sub-500-fs soliton-like pulse in a passively mode-locked broadband surface-emitting laser with 100 mW average power", *Appl. Phys. Lett.*, **80**(21), 3892 - 3894 (2002).
- [Gib96] G. N. Gibson, R. Klank, F. Gibson, and B. E. Bouma, "Electro-optically cavity-dumped ultrashort-pulse Ti:sapphire oscillator", *Opt. Lett.* **21**(14), 1055 (1996).
- [Gra91] G. Grau, W. Freude, "Optische Nachrichtentechnik", Springer Verlag, Berlin (1991).
- [Ham34] W.R. Hamilton, "On a General Method in Dynamics", *Philosophical Transaction of the Royal Society Part II*, 247-308 (1834).
- [Har64] L. E. Hargrove, R. L. Fork, and M. A. Pollack, "Locking of HeNe laser modes induced by synchronous intracavity modulation", *Appl. Phys. Lett.* **5**, 4 (1964).
- [Has73] A. Hasegawa, F. Tappert, "Transmission of stationary nonlinear optical pulses in dispersive dielectric fibers. I. Anomalous dispersion". *Appl. Phys. Lett.* **23** (3), 142144 (1973).
- [Hay07] C. A. Haynam, P. J. Wegner, J. M. Auerbach *et al.*, "National Ignition Facility laser performance status", *Appl. Opt.* **46**, 3276-3303 (2007).
- [Hen82] C.H. Henry, "Theory of the Linewidth of Semiconductor Lasers," *IEEE J.Quant. Electron.* QE-**18**, 259 (1982).
- [Hua91] C.C. Huang, "Sonographic cerebral sulcal development in premature newborns", *Brain and Development*, **13**, 27-31 (1991).
- [Hub05] R. Huber, K. Taira, and J. G. Fujimoto, "Fourier Domain Mode Locking: Overcoming limitations of frequency swept light sources and pulsed lasers", Conference on Lasers and Electro-Optics Europe/ European Quantum Electronics Conference (CLEO/Europe - EQEC 2005), Munich 2005, CP3-5-THU (2005).

- [Hub05B] R. Huber, M. Wojtkowski, K. Taira, *et al.*, "Amplified, frequency swept lasers for frequency domain reflectometry and OCT imaging: design and scaling principles," *Opt. Express* **13**(9), 35133528 (2005).
- [Hub05C] R. Huber, M. Wojtkowski, J. G. Fujimoto, J. Y. Jiang, and A. E. Cable, "Three-dimensional and C-mode OCT imaging with a compact, frequency swept laser source at 1300 nm," *Opt. Express* **13**, 10523-10538 (2005).
- [Hub06] R. Huber, M. Wojtkowski, J. G. Fujimoto, "Fourier Domain Mode Locking (FDML): A new laser operating regime and applications for optical coherence tomography", *Opt. Express*, **14**(8), 3225-3237, 2006
- [Hub06B] R. Huber, D.C. Adler, and J.G. Fujimoto, "Buffered Fourier domain mode locking: unidirectional swept laser sources for optical coherence tomography imaging at 370,000 lines/s," *Opt. Letters* **31**(20), 2975-2977 (2006).
- [Hub10] R. Huber, D. C. Adler, J. G. Fujimoto, "Buffered Fourier domain mode locking: Unidirectional swept laser sources for optical coherence tomography imaging at 370,000 lines/s", *Opt. Lett.*, **31** (20), 2975-2977 (2010).
- [Jay11] V. Jayaraman, J. Jiang, H. Li, P. Heim, G. Cole, B. Potsaid, J. G. Fujimoto, and A. Cable, "OCT Imaging up to 760 kHz Axial Scan Rate Using Single-Mode 1310nm MEMS-Tunable VCSELs with >100 nm Tuning rate," in Quantum Electronics and Laser Science Conference, (Optical Society of America), paper PDPB2 (2011).
- [Jav61] A. Javan, W. R. Bennett, Jr., and D. R. Herriott, "Population inversion and continuous optical maser oscillation in a gas discharge containing a HeNe mixture" *Phys. Rev. Lett.* **6** (3), 106 (1961).
- [Jeo08] M. Y. Jeon, J. Zhang, and Z. Chen, "Characterization of Fourier domain modelocked wavelength swept laser for optical coherence tomography imaging," *Opt. Express* **16**, 3727-3737 (2008).
- [Jir06] C. Jirauschek and F. X. Kärtner, "Gaussian pulse dynamics in gain media with Kerr nonlinearity", *J. Opt. Soc. Am. B*, **23** (9), 1776-1784 (2006).
- [Jir08] C. Jirauschek, B. Biedermann, and R. Huber, "A theoretical description of Fourier domain mode locked lasers," *Opt. Express* **17**, 24013-24019 (2009).
- [Jir08B] C. Jirauschek, C. Eigenwillig, B. Biedermann, and R. Huber, "Fourier Domain Mode Locking Theory", in Conference on Lasers and Electro-Optics/Quantum Electronics and Laser Science Conference, 14031404 (2008).
- [Jir11] C. Jirauschek and F. Ö. Ilday, "Semianalytic theory of self-similar optical propagation and mode locking using a shape-adaptive model pulse", *Phys. Rev. A* **83**, 063809 (2011).
- [Jon05] R. J. Jones, T. Ido, T. Loftus, *et al.*, "Stabilized Femtosecond Lasers for Precision Frequency Metrology and Ultrafast Science" *Laser Physics*, **15**, 7, 10101013 (2005).

- [Kae05] F. X. Kärtner, "Ultrafast Optics", Lecture, MIT (2005).
- [Kat11] L. K. Oxenløwe, "Optical communications: Single-laser super-channel", *Nature Photonics* **5**, 329331 (2011).
- [Ket03] M. W. Zwierlein, C. A. Stan, C. H. Schunck, *et al.*, "Observation of BoseEinstein Condensation of Molecules". *Phys. Rev. Lett.* **91**, 250401 (2003).
- [Kik86] H. Kikuta *et al.*, Distance measurement by the wavelength shift of laser diode light, *Appl. Opt.* **25** (17), 2976 (1986).
- [Kim11] D.-H. Kim, C.-G. Song, I. K. Ilev, *et al.* "Axial-scanning low-coherence interferometer method for noncontact thickness measurement of biological samples," *Appl. Opt.* **50**, 970-974 (2011).
- [Kle11] T. Klein, W. Wieser, C. M. Eigenwillig, *et al.*, "Megahertz OCT for ultrawide-field retinal imaging with a 1050nm Fourier domain mode-locked laser", *Opt. Express*, **19** (4), 3044-3062 (2011).
- [Klo08] P. Klopp, F. Saas, M. Zorn, M. Weyers, and U. Griebner, "290-fs pulses from a semiconductor disk laser," *Opt. Express* **16**, 5770-5775 (2008).
- [Koe64] C. J. Koester and E. Snitzer, "Amplification in a fiber laser", *Appl. Opt.* **3**(10), 1182 (1964).
- [Kra07] L. A. Kranendonk, X. An, A. W. Caswell *et al.*, "High speed engine gas thermometry by Fourier-domain mode-locked laser absorption spectroscopy," *Opt. Express* **15**, 15115-15128 (2007).
- [Kra07B] L. A. Kranendonk, R. Huber, J. G. Fujimoto *et al.*, "Wavelength-agile H₂O absorption spectrometer for thermometry of general combustion gases", *Proc. Comb. Inst.* **31**, 783-790 (2007).
- [Kra08] S. Kray, F. Spöler, M. Först, *et al.*, "Dual femtosecond laser multiheterodyne optical coherence tomography", *Opt. Lett.*, **33**, 18, 2092-2094 (2008).
- [Kui70] D. J. Kuizenga and A. E. Siegman, "FM and AM mode locking of the homogeneous laser Part I: theory", *IEEE J. Quantum Electron.* **6**, 694 (1970).
- [Lam64] W. E. Lamb Jr., "Theory of an optical laser", *Phys. Rev.* **134** (6A), A1429 (1964).
- [Lau07] L. A. Kranendonk, X. An, A. W. Caswell, *et al.*, "High speed engine gas thermometry by Fourier-domain mode-locked laser absorption spectroscopy", *Opt. Express* **15**, 15115 (2007).
- [Lim05] H. Lim, Y. Jiang, Y. Wang, *et al.*, "Ultrahigh-resolution optical coherence tomography with a fiber laser source at 1 μm ", *Opt. Lett.*, **30**, 10 (2005).
- [Liu08] G. Y. Liu, A. Mariampillai, B. A. Standish, N. R. Munce, X. Gu, and I. A. Vitkin, "High power wavelength linearly swept mode locked fiber laser for OCT imaging," *Opt. Express* **16**(18), 14095-14105 (2008).
- [Mai60] T. H. Maiman "Stimulated Optical Radiation in Ruby", *Nature* **187**, 493 - 494 (06 August 1960).
- [Mal08] S. A. Malinovskaya, "Prevention of decoherence by two femtosecond chirped pulse trains", *Opt. Lett.* **33**, 2245-2247 (2008).

- [Mao09] Y. Mao, C. Flueraru, S. Sherif, and S. Chang, "High performance wavelength-swept laser with mode-locking technique for optical coherence tomography," *Opt. Comm.* **282**(1), 88-92 (2009).
- [Max64] J. C. Maxwell, "A dynamical theory of the electromagnetic field", *Roy. Soc. Proc.*, **13**, 531-536 (1864).
- [Max97] C. E. Max, S. S. Olivier, H. W. Friedman, *et al.*, "Image Improvement from a Sodium-Layer Laser Guide Star Adaptive Optics System" *Science* **12**, 277, 1649-1652 (1997).
- [Mea85] R. J. Mears, L. Reekie, S. B. Poole, and D. N. Payne, "Neodymium-doped silica single-mode fibre lasers", *Electron. Lett.* **21**(17), 738 (1985).
- [Mes03] A. Messiah, "Quantum Mechanics", Dover Pubn Inc (2003).
- [Moc65] H. W. Mocker and R. J. Collins, "Mode competition and self-locking effects in a Q-switched ruby laser", *Appl. Phys. Lett.*, **7**, 270 (1965).
- [Moo06] S. Moon and D. Y. Kim, "Ultra-high-speed optical coherence tomography with a stretched pulse supercontinuum source," *Opt. Express* **14**(24), 11575-11584 (2006).
- [Mou86] P. F. Moulton, "Spectroscopic and laser characteristics of Ti:Al₂O₃", *J. Opt. Soc. B*, **3**, 125 (1986).
- [Mur10] E. Murphy, "The semiconductor laser: Enabling optical communication", *Nature Photonics* **4**, 287 (2010).
- [Nee96] M. D. Feit, B. C. Stuart, A. M. Rubenchik *et al.* "Ultrashort Laser Pulse Ablation of Hard Tissue", *OSA Trends in Optics and Photonics*, Optical Society of America **17** (1998).
- [Nog08] G. T. Nogueira, B. Xu, Y. Coello, M. Dantus, and F. C. Cruz, "Broadband 2.12 GHz Ti:sapphire laser compressed to 5.9 femtoseconds using MIIPS", *Opt. Express* **16**(14), 10033 (2008).
- [Ove11] G. Overton, "760 kHz OCT scanning possible with MEMS-tunable VCSEL," *Laser Focus World* **47**(7), 15 (2011).
- [Pam04] F. Pampaloni, J. Enderlein, "Gaussian, Hermite-Gaussian, and Laguerre-Gaussian beams: A primer", *arXiv:physics/0410021v1* (2004).
- [Par94] R. R. Parenti and R. J. Sasiela, "Laser-guide-star systems for astronomical applications," *J. Opt. Soc. Am. A* **11**, 288-309 (1994).
- [Per00] F. Perrenoud, A. Glacet-Bernard, R. Zolf, *et al.* "B-scan ultrasonography and optical coherence tomography (O.C.T.) in epiretinal macular membranes: pre- and post-operative evaluation", *J. Fr. Ophtalmol.* **23** (2), 137-140 (2000).
- [Poc68] R. Goldstein, "Pockels Cell Primer", *Laser Focus* (1968).
- [Pod04] A. G. Podoleanu, G. M. Dobre, R. G. Cucu, *et al.*, "Combined multiplanar optical coherence tomography and confocal scanning ophthalmoscopy" *J. Biomed. Opt.* **9** (1), 86-93 (2004).

- [Sha74] C. V. Shank and E. P. Ippen, "Subpicosecond kilowatt pulses from a modelocked cw dye laser", *Appl. Phys. Lett.* **24**, 373 (1974).
- [Sha75] C. V. Shank, "Physics of dye lasers", *Rev. Mod. Phys.* **47**, 649 (1975).
- [Sch58] A. L. Schawlow and C. H. Townes, "Infrared and Optical Masers" *Phys. Rev.* **112**, 1940-1949 (1958).
- [Sch99] J.M. Schmitt, "Optical coherence tomography (OCT): a review", *IEEE Journal of Selected Topics in Quantum Electronics* **5** (4), 1205 (1999).
- [Sri08] V. J. Srinivasan, D. C. Adler, Y. L. Chen, I. Gorczynska, R. Huber, J. S. Duker, J. S. Schumann, and J. G. Fujimoto "Ultrahigh-speed optical coherence tomography for three-dimensional and en face imaging of the retina and optic nerve head," *Invest. Ophthalmol. Vis. Sci.* **49**, 5103-5110 (2008).
- [Sti95] Ch. Spielman, T. Brabec, and F. Krausz, "Sub-10-fs mirror-dispersion-controlled Ti:sapphire laser", *Opt. Lett.* **20**(6), 602 (1995).
- [Sto74] J. Stone and C. A. Burrus, "Neodymium-doped fiber lasers: room temperature CW operation with an injection laser pump", *Appl. Opt.* **13**(6), 1256 (1974).
- [Sut99] D. H. Sutter, G. Steinmeyer, L. Gallmann, N. Matuschek, F. Morier-Genoud, U. Keller, V. Scheuer, G. Angelow and T. Tschudi, "Semiconductor saturable-absorber mirror-assisted Kerr lens modelocked Ti:sapphire laser producing pulses in the two-cycle regime", *Opt. Lett.* **24**(9), 631 (1999).
- [Swa93] E. A. Swanson, J. A. Izatt, M. R. Hee, "In vivo retinal imaging by optical coherence tomography", *Opt. Lett.* **18** (21), 1864-1866 (1993).
- [Tay00] N. Taylor, "LASER: The inventor, the Nobel laureate, and the thirty-year patent war.", New York: Simon Schuster (2000).
- [Tel75] J. M. Telle and C. L. Tang, "Very rapid tuning of cw dye laser", *Appl. Phys. Lett.* **26**, 572 (1975).
- [Toe97] T. Töpfer, K. P. Petrov, Y. Mine, *et al.*, "Room-temperature mid-infrared laser sensor for trace gas detection," *Appl. Opt.* **36**, 8042-8049 (1997).
- [Tod11] S. Todor, B. Biedermann, W. Wieser, R. Huber, and C. Jirauschek, "Instantaneous lineshape analysis of Fourier domain mode-locked lasers", *Opt. Express* **19**, 8802-8807 (2011).
- [Tod11B] S. Todor, B. Biedermann, R. Huber, and C. Jirauschek, "Balance of Physical Effects Causing Stationary Operation of Fourier Domain Mode-Locked Lasers", *JOSA B* (2012), (print in progress).
- [Tsa11] M. T. Tsai, H. L. Liu, F. Y. Chang, T. C. Chang, and C. H. Yang, "Three-Dimensional and En-Face Optical Coherence Tomography based on a Fourier Domain Mode Locking Laser for Dermatology Study, First International Symposium on Bioengineering, 88-95 (2011).
- [Tys10] R. Tyson, "Principles of Adaptive Optics", CRC Press, 2010.

- [Vai95] E. C. Vail, M.S. Wu, G.S. Li, L. Eng, and C.J. Chang-Hasnain, "GaAs micromachined widely tunable Fabry-Perot filters," *Electron. Letters* **31**(3), 228-229 (1995).
- [Val85] J. A. Valdmanis, R. L. Fork, and J. P. Gordon, "Generation of optical pulses as short as 27 femtoseconds directly from a laser balancing self-phase modulation, group-velocity dispersion, saturable absorption, and saturable gain", *Opt. Lett.* **10**(3), 131-133 (1985).
- [Wie10] W. Wieser, B. R. Biedermann, T. Klein *et al.*, "Multi-Megahertz OCT: High quality 3D imaging at 20 million A-scans and 4.5 GVoxels per second", *Opt. Express* **18**, 14685-14704 (2010).
- [Wit05] S. Witte, R. T. Zinkstok, W. Ubachs, "Deep-Ultraviolet Quantum Interference Metrology with Ultrashort Laser Pulses", *Science* **307**, 400-403 (2005).
- [Yan09] T. Yano, H. Saitou, N. Kanbara, R. Noda, S. I. Tezuka, N. Fujimura, M. Ooyama, T. Watanabe, T. Hirata, and N. Nishiyama, Wavelength modulation over 500 kHz of micromechanically tunable InP-based VCSELs with Si-MEMS technology, *IEEE J. Quantum Electron.* **15**(3), 528-534 (2009).
- [Yar89] A. Yariv, "Quantum Electronic", John Wiley Sons, New York (1989).
- [Yun03] S. H. Yun, C. Boudoux, G. J. Tearney, and B. E. Bouma, "High-speed wavelength-swept semiconductor laser with a polygon-scanner-based wavelength filter," *Opt. Letters* **28**(20), 1981-1983 (2003).
- [Zak68] V.E. Zakharov, "Stability of periodic waves of finite amplitude on the surface of a deep fluid". *J. Appl. Mech. Tech. Phys.* **9** (2), 190194 (1968).
- [Zak74] V.E. Zakharov, S.V. Manakov, "On the complete integrability of a nonlinear Schrödinger equation", *J. Theo. Math. Phys.* **19** (3), 551559, (1974).
- [Zin98] W. Zinth, H.J. Körner, "Physik III", R. Oldenbourg Verlag München Wien (1998).

Publications

Journal papers

S. Todor, Benjamin Biedermann, Wolfgang Wieser, Robert Huber, and Christian Jirauschek, *Instantaneous lineshape analysis of Fourier domain mode-locked lasers*, Opt. Express **19**, 8802-8807 (2011).

S. Todor, Christian Jirauschek and Robert Huber, *Balance of physical effects causing stationary operation of Fourier domain mode-locked lasers*, JOSA B (2012). (print in progress)

Conference papers

S. Todor, C. Jirauschek, B. Biedermann, and R. Huber, *Linewidth Optimization of Fourier Domain Mode-Locked Lasers*, Conference on Lasers and Electro-Optics, (Optical Society of America, 2010).

S. Todor, C. Jirauschek, B. Biedermann, and R. Huber, *Analysis of the Optical Dynamics in Fourier Domain Mode-Locked Lasers*, Optical Sensors, (Optical Society of America, 2010).

C. Eigenwillig, S. Todor, W. Wieser, B. Biedermann, T. Klein, C. Jirauschek, and R. Huber, *Picosecond pulses from an FDML laser*, Conference on Lasers and Electro-Optics, (Optical Society of America, 2012). (accepted)

Acknowledgment

First of all I would like to thank Dr. Christian Jirauschek for providing the interesting topic which I was allowed to work on during the last three years. Without his tremendous knowledge and support in the field of optics and laser physics, the completion of this thesis would not have been possible. There was seldom a problem for which he could not provide a hint or at least a guess which often led into the right direction. His helpful insights often proved to enable the solution of very complicated seeming problems. Also his motivation and his experience in science proved crucial for the success of this thesis.

I would also like to thank Prof. Paolo Lugli for giving me the chance to work at the Institute for Nanoelectronics. Although my topic was not very much related to the other topics of research at the institute, I am glad that I have been a part of the team for the last three years. His welcome at the institute offered me the chance to work on a highly interesting topic within the Emmy-Noether research group.

I would also like to thank Dr. Robert Huber from the LMU group, who is responsible for the experimental setup of the FDML laser. His immense insight in the field of experimental laser physics in general and FDML lasers in special, lead to very interesting converstations and often inspired interesting new research topics. From his group I would like to thank Christoph Eigenwillig for the very effective and productive cooperation. The work with him was an excellent example of how well theoretical and experimental physics can fit together. I would additionally like to thank Dr. Benjamin Biedermann for his earlier work which provided me with a lot of excellent data.

Next I would like to thank Edgar Albert for a lot of help he offered me with programming related questions. His valuable insight enabled me the solution of some tricky programming issues. But more than that I would like to thank him for the excellent friendship that emerged during the last two years, that will surely by far outlive the time here together at the institute.

I would also like to thank Dr. Alpar Matyas for the friendly atmosphere during the time in the Emmy-Noether research group. His calm and concentrated working method not only led to no distractions, but also motivated me to pursue my PhD as efficiently as he did. Next, I would like to thank Dan and Bogdan Popescu for the friendly atmosphere in the office. Four Romanians together in an office sounds like trouble, but indeed this proved to be a very excellent combination. I never encountered a better and friendlier atmosphere in an office in my entire life.

I would then also like to thank Lucia Weik and Rita von Grafenstein for helping me with the complicated paperwork. Bureaucracy is by far more complicated than physics, but with their help it proved to be no problem.

I would also like to thank Rosi Heilmann and Lucia Weik for the help with Alpar's doctoral hat. It proved to be an extremely ambitious undertaking. Especially the movement of Alpar's head was a variable that should have been taken into account. Nevertheless, it was fun.

To all those in the institute that are not mentioned here, I would like to express my gratitude for the friendly atmosphere during the last three years at the institute.

Finally, I want to give a special thanks to all my friends who supported me during this time, especially Imad Dahhan from Kassel University, the best friend one could hope to meet in an entire lifetime. And an extra special thanks goes to my parents, whose support was as always limitless and gave me the strength to finish the PhD work.

Curriculum Vitae

Sebastian Todor

Persönliche Daten

Geburtsdatum:	09.09.1981	
Geburtsort:	Temeschburg Rumänien	
Adresse:	<i>privat:</i> Springerstr.19 81477 München +49 176 80135052	<i>beruflich:</i> Lehrstuhl für Nanoelektronik Technische Universität München Arcistr. 21 Tel. +49 89 28925331, todor@tum.de
Familienstand:	ledig	
Staatsangehörigkeit:	Deutsch	
Eltern:	Renate Schamarek, geb. Ioanovits Marius Todor	

Schulischer Werdegang

1988-1989:	Grundschule Hatzfeld, Rumänien
1990-1992:	Pestalozzi Grundschule Ingolstadt
1992-2001:	Katharinen-Gymnasium Ingolstadt
06/2001:	Abitur

Studium

10/2002-10/2008:	Diplom Physik an der Technischen Universität München
10/2008	Abschluss der Diplomarbeit zum Thema "Solare Neutrinos mit LENA und spektroskopische Untersuchung von Flüssigszintillatoren"
10/2008	Erlangung des Diploms mit Note "Sehr gut"

Promotion

seit 12/2008:	Wissenschaftlicher Angestellter am Lehrstuhl für Nanoelektronik, Technische Universität München
---------------	--

Praktika und hilfswissenschaftliche Tätigkeiten

02/2005 – 05/2005:	Werkstudent am Lehrstuhl E 18 der TUM
06/2007 – 08/2007:	Werkstudent am Lehrstuhl E 15 der TUM
08/2007:	Projektarbeit zum Thema Protonenzerfall in einem großen Flüssigszintillationsdetektor